IMPROVING THE CONTRAST OF TWO-PHOTON MICROSCOPY AND THE APPLICATION OF FLUORESCENCE METHODS TO THE DETECTION OF TUBERCULOSIS

A Dissertation

Presented to the Faculty of the Graduate School

Of Cornell University

In Partial Fulfillment of the Requirements for the Degree of

Doctor of Philosophy

by

Jesse Donald McMullen

May 2010

IMPROVING THE CONTRAST OF TWO-PHOTON MICROSCOPY AND THE APPLICATION OF FLUORESCENCE METHODS TO THE DETECTION OF TUBERCULOSIS

Jesse Donald McMullen, Ph.D.
Cornell University 2010

Multiphoton fluorescence microscopy (MPM) has proved itself a useful tool in the exploration of a vast variety of biological material. Recently, it has been demonstrated as capable of producing histological grade images from biopsied tissue, without the need for the intensive preparations characteristic of standard histology. Unfortunately, the intrinsic fluorescence of the tissue is quite dim, necessitating high laser intensity which produces both photo-bleaching and photo-damage. In order to increase the fluorescence detection in excess of the standard epi-collection, we have created a collar of light guides which surround the sample increasing the solid angle of collection. Furthermore, in an effort to maximize the available solid angle of collection, we have designed a new type of objective lens specifically for MPM. This objective possesses an extremely wide field of view, a sufficient numerical aperture, and, when numerically tested against the best current objective, collected more than an order of magnitude more fluorescence. In addition to improving the instrumentation, we have also attempted to increase the brightness of the biological tissue by using the endogenous fluorescence of a number of anti-tumor drugs. The two-photon absorption of these drugs was characterized. One of the measured drugs, Irinotecan, was used to image ovarian cancer

allowing the acquisition of better quality images at much lower excitation energies than native fluorescence allowed. Additionally, this drug demonstrated a preference for tumors relative to native tissue, aiding the discrimination of the tumor tissue.

Through the fluorescent imaging of another disease, tuberculosis, we will hopefully gain a better understanding of the illness which will lead to new types anti-tubercular drugs. To that end we have constructed a fluorescent bronchoscope that will be used to image tuberculosis bacteria which will have been selected to express a GFP variant on genes been demonstrated to be transcriptionally up-regulated in response to various environmental stresses such as low pH, hypoxia, and drug sensitivity. We have also examined the use of fluorescence lifetime imaging to identify the bacteria, and to image it against the bright background fluorescence of the pulmonary tract.

BIOGRAPHICAL SKETCH

Jesse was born one sepia colored Monday, ever so long ago, in that great metropolis, Toronto, which serves as both the center and scapegoat of its vast nation. Much of his youth however, was spent either exploring the woods and streams of Kolapore, or else amid the vast landscapes of the printed page – provinces which continue to reveal their pleasures to him to this day. Eventually, as he found himself mathematically and mechanically inclined, he made his way to Kingston, where he earned a bachelor's degree in Engineering Physics from Queen's University. Subsequent years of study at Cornell University were filled with adventures: high, low, and in between. After completing his thesis - and as unsure about the immediate future as he is about the distant - he decided to try his hand at traveling and enters that fog-filled realm with patient optimism. Regardless of the direction the road will take, he looks forward to finding out the answer to that age old riddle, what happens next...

To my father

who said "We want you to succeed! Do not waste your genes!"

And to my mother

who convinced me to wear them,

And to my sister

who constantly complements me on how they look.

ACKNOWLEDGEMENTS

It is rather daunting to begin acknowledgements knowing I am indebted to so many people who have made my time in Ithaca so rewarding and interesting. I should like to thank my advisor Warren Zipfel, for his patience and encouragement during my graduate degree, and also as a guide into a great variety of fields and disciplines. The wealth and breadth of his knowledge has proved something to strive towards obtaining, if slightly intimidating. Becky Williams should also be thanked for all the help she has proffered over the years. Over and over again she has demonstrated the ability to ask off the cuff questions of penetrating insightfulness that have helped move things along. Thanks to my committee: Watt Webb (for his introduction to the field), Alex Gaeta, and Barbara Baird. I would also like to thank the NIH and the Bill and Melinda Gates foundation for the funding which has enabled all the research in this document.

I have had the pleasure of working with an enthusiastic and bright group of researchers many of whom have become good friends. To Avtar, Lisa, Paul, Evan, Val, Johanna, Pam, Sylvia, Sned, Nate, Mark, Elaine, Huimin, Ina, Minghan, Alex (and Judy), Jie, Huizhong (and Jane), Liz, Tobias, Chris, Dan (and Liz), Sally, Dimitre, Shalin... and all those who put up with my various questions or complaints - thank you.

It's also been my pleasure to make many friends over the course of my time in Ithaca whose attention and diversion have helped to smooth out the rough times and celebrate the good. A few words here hardly seem an adequate recompense for the privilege of their acquaintance. I`ll focus on the Ithacan friendships, though there are many at home deserving of the thanks I send. I`ve had the pleasant good fortune to land myself as crew on

Fantasy, and many hours were spent racing on Cayuga lake in all weathers. I am grateful to Eberhard Alsen and the rest of the gang: Rick, David, Chris, and Rebecca, for a warm introduction to the sport of sailing. Ian, Stephen, and the Monday night philosophes provided stimulating conversation and an introduction to a world I value much more now than I did before. Nic Lane, though his time in Ithaca was short has remained a good friend. Saikat and Sharvari are to be thanked for many more dinners than I could ever hope to pay back, and making me feel like an honorary Indian. Kurt and Julie have not only been fun to hang out with, but have all ways been the first to lend a hand or groan at a pun. Jeff and Julia, my one time roommates, have had a great impact on my life that extends far beyond teaching me how to cook and introducing me to Townes van Zandt. Jose, Gabi, and young Camila have been with me in Ithaca through the whole course of my studies and have become so enmeshed in my life that even my family feels like they`re related. What Larks!

Finally, I would like to thank my family - the clans Faye, Herstone, Matthews, and Weissberg - who have been a true backbone during the course of my studies. Without them, I can't imagine where I'd be, but definitely not here. Special mention is due to my Grandmothers, Lee and Dolly, both of whom could always be relied on whenever I was in need of an ego boost. To my parents and my sister I give my love which seems hardly a fit return for all they have given me.

TABLE OF CONTENTS

LIST OF FIGURES

LIST OF TABLES

LIST OF ABBREVIATIONS

Acoustic Optical Modulator (AOM)

Anti-cancer Drugs (ACDs)

Electric Optical Modulator (EOM)

Field of View (FOV)

Microstructured Fiber (MSF)

Multiphoton Microscopy (MPM)

Mycobacterium tuberculosis (mtb)

Numerical Aperture (NA)

Photomultiplier Tube (PMT)

Second Harmonic Generation (SHG)

Single Mode Fiber (SMF)

Total Internal Reflection (TIR)

Chapter 1 – An Introduction

It has been twenty years since the development of multiphoton microscopy in the laboratory of Watt Webb (Denk et al., 1990), allowing high resolution fluorescence microscopy to penetrate the depths of scattering media like no other technique before it. The intervening years have seen a rapid expansion of the technology (Zipfel et al., 2003b) which has proven its usefulness in such diverse areas from neurobiology to polymer lithography. Its utility, which stems from the localisation of the fluorescence generation to within a defined focal volume, has made it a suitable partner to a variety of biophysical methods including fluorescence correlation spectroscopy, fluorescence recovery after photobleaching, and fluorescence photoactivation. Additionally, its employment of a pulsed excitation source gives it an intrinsic gating property that makes it compatible with the time correlation requirements of fluorescence lifetime microscopy. Commercial systems, available from microscope manufacturers such as Carl Zeiss and Olympus, are now becoming standard instruments in imaging facilities at research institutions throughout the world. Both the instrumentation and the application of this technique continue to be advanced here at Cornell. This thesis presents my contributions to the enhancement of the overall imaging capabilities of two-photon microscopes and their application to biological systems – with a bit of standard fluorescence imaging thrown in at the end for good measure. As the succeeding chapters assume that the reader is familiar with MPM, perhaps a bit of background is in order.

Multiphoton microscopy (MPM) relies on two or more photons fulfilling a role that is normally performed by only one. In two-photon

absorption, two near-IR photons are simultaneously absorbed by an electron in a fluorescent molecule, which enters into an excited state. Sometime later (typically nanoseconds) it decays back down to the ground state by releasing the absorbed energy as a fluoresced photon of slightly greater than half the excitation wavelength (due to vibrational losses). Therefore, the amount of fluorescence generated varies with the square of the input power and may be defined explicitly in thick tissue (Xu and Webb, 1996) as:

$$\langle F(t)\rangle = \frac{1}{2}\phi\eta_2\sigma_2 C\frac{g_P}{f\tau}\frac{8n\langle P(t)\rangle^2}{\pi\lambda} \quad (1)$$

here ϕ is the collection efficiency of the system, η_2 is the quantum efficiency of the fluorescent molecule, σ_2 its two photon cross-section and C its concentration, g_p a measure of the pulse temporal coherence, *f* the laser repetition rate, τ the pulse width, n the refractive index, λ the wavelength, and P the power. In general, the probability of these nonlinear processes occuring is very low. As a result, the photons are compressed in both time and space to rapidly increase the likelihood of their coincidence without drastically changing the average beam energy. This confines the excited fluorescence to a tiny focal volume that may be scanned in order to record an image. It is this profound result – that all fluorescent light can be considered signal – when combined with the property that the excitation light is twice the typical wavelength (and therefore scatters about half as much), is what creates the two-photon advantage over other forms of fluorescence microscopy.

A typical MPM system is depicted in Figure 1.1. It begins with the Ti:Sapphire oscillator pumped by green light from a continuous-wave laser (such as a Nd:YVO_4 solid state laser such as the Millennia from Spectra

Physics) producing ultra-short pulses across a broad range of wavelengths from 690 to 1000 nm. These pulses are typically on the order of 80-100 fs in duration with associated bandwidths of 10-15nm. Recently developed fiber based systems are capable of producing high power ultra-short pulses within the Ti:Sapphire range, as well as at points outside of it (eg. the 1064 nm Fianium Femtolaser). While these have the potential to make MPM microscopy more affordable and accessible (through simplification and reduction in system size), they currently suffer from longer pulse widths, lower peak powers, and poor wavelength tunability when compared to the more expensive free space crystal resonators. The latter typically operate around 80 MHz which correlates to a peak-to-peak pulse spacing of 12.5 ns, or enough time for the typical fluorophore to be excited and then fluoresce back to its ground state. Recently, super-high repetition rates have been achieved by injecting the output from an 80 MHz laser into Fabry-Perot etalon (Ji et al., 2008), increasing the pulse frequency by greater than 100x while lowering the average pulse energy to a picojoule. This was shown to greatly mitigate photo-bleaching and photo-damage while improving acquisition speeds. The technique is still new enough, however, that it has not been widely implemented. Another modification to the laser path that is more widely deployed is a dispersion compensation system. By using prisms, gratings, or chirped mirrors to provide anomalous dispersion to temporally chirp the excitation pulse, it is possible to compensate for the group velocity dispersion of the glass in the optical path.

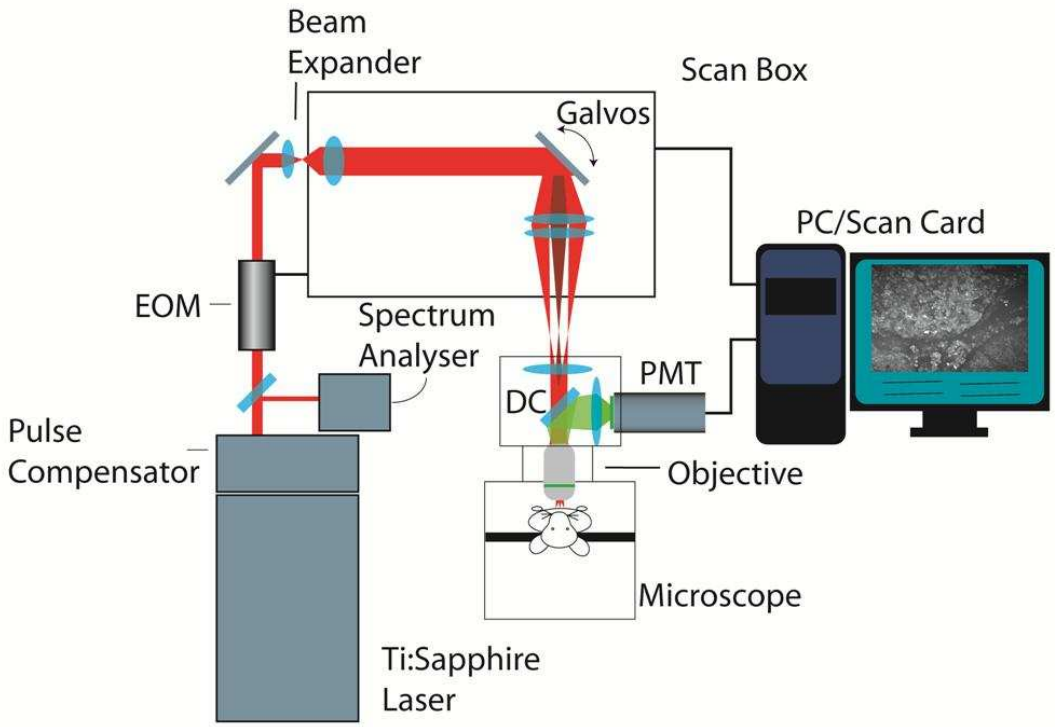

Figure 1.1 – A schematic of a standard multiphoton microscope. A Ti:Sapphire laser is used to produce ultra-short pulses. These may be pre-chirped to compensate for glass dispersion in the system. The beam is shuttered using an electro-optic modulator (EOM) and enters the scanbox. There it is expanded and deflected in the x-y directions by galvanometers. This serves to tilt the beam on the back aperture of an objective, resulting in a scanned focal volume. A dichroic filter is used to separate the emission from the excitation pathway, where a photomultiplier tube (PMT) is used to convert the photon flux to an electrical signal that can be integrated in the scancard. The scancard also controls the pixel clock associated with beam scanning as well as the EOM. In some laser systems, it may also be used to operate the laser.

This allows for the delivery of transform-limited pulses to the sample and a corresponding increase in the two-photon excited fluorescence.

After the excitation source, a spectrum analyser may be used to measure the wavelength profile and verify mode-locking. New laser systems have a digital output of both of these features and in that case this instrument may be omitted. Regulation of beam intensity may be done in several different ways. Neutral density (ND) filters serve to evenly attenuate the light over a variety of wavelengths, however even reflective ND filters spatially aberrate the multi-Watt beam as a result of uneven thermal expansion within the glass. Alternatively, an electric-optical modulator (EOM) such as a Pockels cell or an acoustic optical modulator (AOM) is used to electrically vary the beam intensity or to achieve fast modulation. The former device exploits the electrically variable birefringence of noncentrosymmetric crystals to rotate the polarization of the light causing extinction when passing an output polarizer. The latter instrument uses diffraction from transducer induced standing waves in glass to diffract a given portion of the beam. While the AOM has the advantage of producing absolute extinction, it is slower, has lower maximal transmission (70% rather than ~85%), and is twice as dispersive as a Pockels Cell; incidentally, some of this dispersion was found to be of higher order and therefore not compensatable by pre-chirping. The AOM's ability to deflect the beam has proven useful for spot scanning, in which the focal volume can be directed for uncaging/bleaching events at disparate points within an image (Shoham et al., 2005).

Image scanning is typically produced using galvanometers which tilt the beam on the back focal plane of the objective. This raster scans the

focal volume in horizontal lines similar to the way one reads a page in English. In this arrangement, the EOM is used to rapidly blank the beam during the time the horizontal galvanometer returns to its start position in order to avoid unnecessary photo-exposure. In some cases – at the cost of timing issues that affect the alternating lines – a bi-directional raster scan in which the image is recorded left to right, then right to left, is used to increase acquisition speed. When imaging speed is important, there are a number of more complex methods that can improve the acquisition rate. For example, complex three dimensional scans can be arranged (Göbel et al., 2007) in which the path of the focal volume is controlled to pass through the soma of identified cells. This allows maximal sampling with minimal imaging of the intercellular space. This technique replaces the z-stepper motor of a standard system with a piezoelectric objective translator. Other modifications away from a point-scanning system can further increase the acquisition rate, although these require imaging the focal plane on to a detector and use a CCD rather than a PMT. For example, by inserting a cylindrical lens into the optical path and scanning a line rather than a single point (Kim et al., 1998) one can acquire images at the rate of a few hundred Hertz. Alternatively, by creating a matrix of focal points by using an array of microlenses (Bewersdorf et al., 1998) or a diffractive optic element (Sacconi et al., 2003) one is able to scan multiple focal volumes simultaneously. Although these techniques have increased the imaging rate at a cost to the imaging depth, the recent application of multi-anode PMT arrays (Kim et al., 2007) has somewhat improved this trade off.

The majority of multiphoton systems, like the one presented in Figure 1.1, scan a single focal volume by focusing the excitation light using a high

NA objective. It has been demonstrated both experimentally and theoretically (Beaurepaire and Mertz, 2002) that an ideal MPM objective has as low a magnification as possible and as high a numerical aperture: giving a large field of view and the best possible resolution. This has led to the improvement of standard water immersion objectives from 60x/0.9 NA to 25x/1.05 NA (both Olympus). The fluorescence excited by these objectives is traditionally collected in the epi-direction (back through the objective), but in the case of thin samples may be collected in the transmitted direction as well. In either case, a dichroic mirror is used to separate the emission from the excited light and the former is converted to integratable electrical signal by a photomultiplier tube (the detector of choice due to its large active area and fast response). There has been a large improvement in these detectors over the years and a shift away from bi-alkali to multi-alkali meshless photocathodes with high quantum efficiency in the blue end of the spectrum and GaAs/GaAsP PMTs for use in the red end.

Given a standard MPM system, it is reasonable to consider just how deep it is possible to image into tissue (this being the speciality of two-photon microscopy). The imaging depth of a two-photon system varies from sample to sample as a result of the scattering and absorption characteristics of the tissue as well as the distribution and brightness of the fluorophore. The maximum imaging depth has been summarized as derived from equation 1) by (Theer et al., 2003) for a given average power ($\bar{P}$) as:

$$z_{max} = \ell_s \ln\left(\bar{P}\,\gamma\sqrt{1/f\tau}\right) \qquad 2)$$

where ℓ_s is the scattering mean free path (how far on average a fluoresced photon will travel on average before scattering), τ the pulse width and *f* the repetition rate of the excitation laser, and γ is defined by:

$$\gamma = \left[\sigma_2^* \phi(z_{max}) \Big/ \bar{P}(z_{max}) \right]^{1/2} \qquad 3)$$

here σ_2^* is the two-photon action cross-section, $\phi(z_{max})$ is the collection efficiency of the system for that focal plane, and $\bar{P}(z_{max})$ the average power at the focus. In general the high scattering cross-section of haemoglobin below 600 nm (Cheong et al, 1990) limits penetration into bloody tissues, such as the liver, to several hundred microns, whereas image depths of 600 μm are standard in the cortical layers of the brain.

In order to penetrate deeper into the tissue, changes need to be made to the instrumentation of the system. Adaptive optic systems have been shown to correct for deformations to the wavefront of the excitation beam (Rueckel et al., 2006) increasing the effective number of ballistic photons that reach the focal plane without increasing the excitation power. By shifting to longer excitation wavelengths than are achievable with just a Ti:Sapphire oscillator longer wavelength dyes may be excited This effectively lowers the scattering mean free paths for both the excitation and emission wavelengths. The output of an optical parametric oscillator at 1280nm has been used to image the neuronal architecture labelled with Alexa680-dextran at depths greater than a mm in the brain (Kobat et al., 2009). These same penetration depths have also been achieved by using a low rep-rate regenerative amplifier producing 3 μJ pulses at 925nm (Theer et al., 2003), effectively increasing the peak power so that a high number of

ballistic photons remained even after many scattering lengths. Ultimately, however, scattering reduces the excitation power in both these techniques, and out-of-focus fluorescence at the surface (from the high unscattered intensity there), overwhelms the excited signal from the focal volume (Theer and Denk, 2006). There are methods to get around this by deforming the beam spatially or temporally. By applying a phase mask onto the wavefront of the beam it is possible to so deform the focus (effectively inducing the opposite of the standard adaptive optics technique) such that little fluorescence is excited there. This creates the acquisition of an image solely composed of out-of-focus fluorescence that can be subtracted from one that was acquired normally, thus increasing the signal to noise ratio (Leray and Mertz, 2006). Temporal focusing by using a grating to separate the various spectral components of the beam spatially and temporally chirps the pulse so much that the surface intensity is greatly reduced. As the beam is focused, the wavelength components come together and normal pulse widths are achieved (Zhu et al., 2005) with minimal out-of-focus fluorescence.

While it will not get rid of out-of-focal volume fluorescence problem, a straightforward way of increasing the depth (up to a point) is to increase the amount of fluorescence detected by improving the collection efficiency of the system. This has the added benefit of allowing for the reduction of the illumination powers or the increase of the scan speed consequently mitigating tissue damage from photon exposure. As mentioned previously, collection in the forward path will enhance signal to noise for thin specimens. It is also possible (Combs et al., 2007) to employ a parabolic mirror below the sample to reflect fluoresced light back through the epi-objective. Rather complex reflecting objectives have also been designed

(Vucinic et al., 2006) in order to increase the collection of scattered light. When one considers the total solid angle collected by an objective lens, the results are strikingly low (Figure 1.2). Even a modern lens like the Olympus XLUMPLFL 20x/0.95W objective collects only about 30% of the fluorescence radiated into the hemisphere facing its front aperture. The second chapter of this thesis describes our efforts to increase this fluorescence emission solid angle by the addition of extra collection pathways. Therefore, the work in the second chapter attempts to remedy this short coming through the addition of a ring of high NA liquid light guides mounted around the sample. The significant image enhancement of this design scheme, especially on the Olympus 4x XLFLUOR macro lens, allowed for a significant increase in signal collection at the expense of the awkwardness inherent in having five large light guides emerging from the sample area (it was not without reason that this system was initially labelled "the Medusa detector"). It also had the added benefit of providing a second detection pathway with which to observe SHG anisotropy.

Motivated by the relatively lax chromatic requirements of multiphoton optics, the next logical step was a complete redesign of an objective based on this idea of maximal solid angle. The utility of a large field of view was becoming evident in our imaging experiments, so we decided to incorporate this into our lens design. We realised as well that, unlike other forms of fluorescence microscopy which need to project an image onto a conjugate focal plane, the excited fluorescence need only be directed within the area of the photocathode of some non-descanned detector. Thus, we

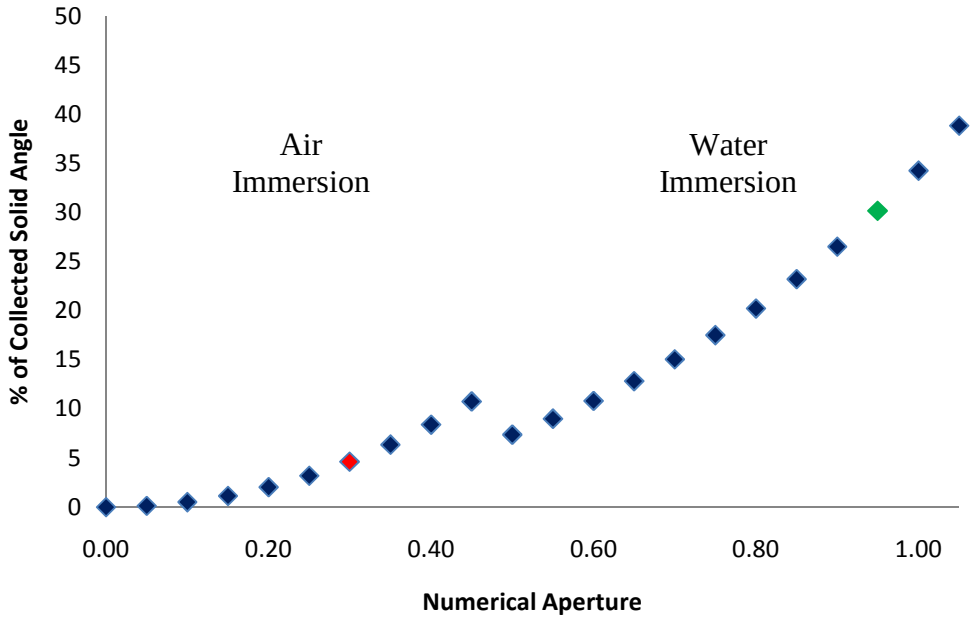

Figure 1.2 – A plot demonstrating the collected fraction of solid angle of a hemisphere radiated from the focal point of an objective as a function of its numerical aperture. The discontinuity stems from the fact that the immersion media is taken to be water for all numerical apertures greater than 0.45.

placed the detector as close to the sample as possible - incorporating it into the objective casing by including a dichroic beam splitter as one of the lens elements. The resulting lenses, discussed in Chapter 3, were tested (via non-sequential modeling) against the patent of the Olympus 4x lens and demonstrated capable of collecting over an order of magnitude more fluoresced light than the current lens, while maintaining better resolution and a comparable field of view.

This lens was designed with an application to multiphoton pathology in mind, in an attempt to improve upon the already stellar histological grade images that MPM has been demonstrated (Rogart et al., 2008, Zipfel et al., 2003a) capable of generating. There is also a growing effort to design a nonlinear fluorescence endoscope. However, these early devices (from Helmchen et al., 2001 to Le Harzac et al., 2009) have proven incapable of satisfactorily imaging even large fluorescent beads, as they suffer from the difficulty: of miniaturizing a non-descanned detection pathway; the fiber delivery of ultra-short pulses (see Appendix B); and the effective implementation of a distal end scanning system. Efforts to generate images suitable for pathology using only intrinsic fluorescence are further hindered by the extremely low two-photon cross-sections of these endogenous fluorophores (Zipfel et al., 2003a) which are several order of magnitudes below that of normal dyes. Unlike in the laboratory, clinical *in vivo* tissue imaging cannot benefit from the myriad of available commercial dyes, with their variety of specialized functions (e.g. calcium sensitivity, ligand binding etc.) as only fluorescein and indocyanine green are FDA-approved for use in humans. In order to examine other potential contrast agents that might benefit MPM endoscopy, we performed a survey of various fluorescent anti-

cancer agents and Chapter 4 reports the measured two photon action cross-sections for these various drugs. We selected one of the "brightest" candidates – the topoisomerase I inhibiter irinotecan – and applied it to a metastasizing ovarian epithelial cancer model. Multiphoton images were made of tissue and tumors excised from sick mice that had been given intraperitoneal injections of Camptosar (the trade name of irinotecan distributed by Pfizer). Not only did this compound show over an order of magnitude increase in the fluorescence signal strength when compared to control samples, the fluorescence was found to be preferentially four times brighter in the cancer tissue.

Sometimes, the complexity of an MPM system with it ultra-expensive high powered lasers and automated scanning system is not worth the benefit one gains from its intrinsic sectioning ability. When presented with the problem of the *in vivo* detection of fluorescent *Mycobacterium tuberculosis* (Mtb) against the auto-fluorescence of the pulmonary tract of primates, we decided to leave the world of nonlinear excitation to employ standard one-photon excited fluorescence. The fifth chapter details the preliminary work we have made to this end. As part of a large multi-institutional collaboration funded by the Bill and Melinda Gates Foundation, we have constructed a fluorescence bronchoscope that will be used as one of an array of diagnostic tools in the examination of the response of tubercular granulomas to novel drugs. This device was designed with an outer diameter of under 800 microns, the capability to image two different channels simultaneously, and the power to image and reactivate the photo-switchable fluorescent protein Dronpa. By this last mechanism we have shown that it is possible to eliminate a large portion of background fluorescence simply by image

subtraction. Additionally, we have begun exploratory work attempting to use the endogenous fluorescence of the bacterium as a means of detecting it. The lung tissue itself is strongly autofluorescent and serves as a hindrance to both the projects in this chapter. However, the unusually long lifetime of the main Mtb fluorophore, coenzyme F_{420}, promises to allow discrimination of the bacterium from the surrounding lung tissue, which could potentially find application in the clinical diagnosis of tuberculosis.

Finally, the concluding chapter looks back at the work presented in this thesis and attempts to make suggestions regarding further experiments that may prove useful in the future.

REFERENCES

Beaurepaire E and Mertz J, "Epifluorescence collection in two-photon microscopy", Appl. Opt. **41** 5376-5382 (2002).

Bewersdorf J, Pick R, Hell SW, "Multifocal multiphoton microscopy" Opt. Lett. **23** 655–657 (1998)

Cheong WF, Prahl SA, Welch AJ, "A Review of the Optical Properties of Biological Tissues", IEEE J. Quant. Elec. **26** 2166-2185 (1990)

Combs C, Smirnov A, Riley J, Gandjbakhche A, Knutson J, Balaban R, "Optimization of multiphoton excitation microscopy by total emission detection using a parabolic reflector" J. of Microscopy **228** 330-337 (2007)

Denk W, Strickler JH, Webb WW, "Two-photon laser scanning microscopy" Science **248** 73-76 (1990)

Denk W, Svoboda K. (1997) Photon upmanship: why multiphoton imaging is more than a gimmick. *Neuron* **18**, 351 -357

Göbel W, Kampa B, Helmchen F, "Imaging Cellular network dynamics in three dimensions using fast 3D laser scanning" Nature Methods **4** 73-79 (2007)

Helmchen F, Fee MS, Tank DW, and Denk W, "A miniature head-mounted two-photon microscope: High-resolution brain imaging in freely moving animals," Neuron **31** 903-912 (2001)

Ji N, Magee J, Betzig E, "High-speed, low-photodamage nonlinear imaging using passive pulse splitters" Nat. Methods **5** 197-203 (2008)

Kim KH, Buehler C, So PTC, "High-speed, twp-photon scanning microscope" App. Opt. **38** 6004-6010 (1998)

Kim KH, Buehler C, Bahlmann, Ragan T, Lee WCA, Nedivi E, Heffer E, Fantini S, So PTC, "Multifocal multiphoton microscopy based on multianode photomultiplier tubes" Opt. Exp. **17** 11658-11678 (2007)

Kobat D, Durst M, Nishimura N, Wong A, Schaffer C, Xu C, "Deep tissue multiphoton microscopy using longer wavelength excitation" Opt. Express **17** 13354-13357 (2009)

Le Harzac R, Riemann I, Weinigel M, Konig K, Messerschmidt B, "Rigid and high-numerical-aperture two-photon fluorescence endoscope" Applied Optics, **48** 3396-3401 (2009)

Leray A, Mertz J, "Rejection of two-photon fluorescence background in thick tissue by differential aberration imaging" Opt. Express **14** 10565-10573 (2006)

Rogart JN, Nagata J, Loeser CS, Roorda RD, Aslanian H, Robert ME, Zipfel W, Nathanson MH, "Multiphoton Imaging Can Be Used for Microscopic Examination of Intact Human Gastrointestinal Mucosa Ex Vivo" Clincial Gastroenterology and Hepatology **6** 95-101 (2008)

Rueckel M, Mack-Bucher JA, Denk W, "Adaptive wavefront correction in two-photon microscopy using coherence-gated wavefront sensing" PNAS **103** 17137-17142 (2006)

Sacconi L, Froner E, Antolini R, Taghizadeh MR, Choudhury A, Pavone FS, "Multiphoton multifocal microscopy exploiting a diffractive optical element" Opt. Lett. **28**, 1918–1920 (2003)

Shoham S, O'Connor DH, Sarkisov DV, Wang SSH, "Rapid neurotransmitter uncaging in spatially defined patterns" Nat. Methods **2** 837-843 (2005)

Theer P, Denk W, "On the fundamental imaging depth of two photon microscopy" J. Opt. Soc. Am. **23** 3139-3150 (2006)

Theer P, Hasan M, Denk W, "Two-photon imaging to a depth of 1000 μm in living brains by use of a Ti:Al2O3 regenerative amplifier" Opt. Lett. **28** 1022-1025 (2003)

Vucinic D, Bartol TM, Sejnowski TJ, "Hybrid reflecting objectives for functional multiphoton microscopy in turbid media," Optics Letters **31**, pp. 2447-2449 (2006)

Xu C, Webb WW, "Measurement of two-photon excitation cross sections of molecular fluorophores with data from 690 to 1050nm" J. Opt. Soc. Am B. **13** 481-492 (1996)

Zhu GH, van Howe J, Durst M, Zipfel W, and Xu C, "Simultaneous spatial and temporal focusing of femtosecond pulses", Opt. Express **13,** 2153-2159 (2005)

Zipfel WR, Williams RM, Christie R, Nikitin A, Hyman BT, & Webb WW, "Live tissue intrinsic emission microscopy using multiphoton excited native fluorescence and second harmonic generation," PNAS, **100,** 7075-7080 (2003a)

Zipfel WR, Williams RM, & Webb WW, "Nonlinear magic: multiphoton microscopy in the biosciences," Nat Biotech. **11,** 1369-77 (2003b)

Chapter 2 - Enhancing Collection Efficiency in Large Field of View Multiphoton Microscopy[1]

Abstract

Many multiphoton imaging applications would benefit from a larger field of view (FOV); however, large FOVs (>mm) require low magnification objectives which have low light collection efficiencies. We demonstrate a light collection system mounted on a low magnification objective that increases fluorescence collection by as much as 20-fold in scattering tissues. This peripheral detector results in an effective NA of collection > 0.8 with a 3-4 mm field of view.

Introduction

Multiphoton microscopy (MPM) has become an important fluorescence imaging modality since its invention nearly two decades ago (Denk et al., 1990; Zipfel et al., 2003b). MPM's intrinsic 3D localization of excitation allows for deeper imaging into scattering tissues while maintaining high resolution and signal-to-noise. MPM optics have greatly improved over the past decade. For many applications the ideal two-photon objective lens would be of low magnification and high NA, the former determining the size of the field of view (FOV), and the latter the resolution and light collecting ability (Oheim et al., 2001). This design requirement has led to the development of physiological objective lenses with magnifications between 20-25X and numerical apertures around 1.0. These newer objective lenses provide enhanced collection at larger FOVs compared to earlier

[1] McMullen J, Kwan A, Williams R, Zipfel W, "Enhancing Collection Efficiency in Large Field of View Multiphoton Microscopy" J. Microscopy Accepted

physiological objectives of similar NA and have greatly improved imaging in applications such cell trafficking and tracking (Miller *et al.*, 2003), calcium imaging in neural networks (Gobel & Helmchen, 2007), *in vivo* studies of nutrient transport (Williams *et al.*, 2007) and for examination of pathologic tissues (Zipfel *et al.*, 2003a). In many of these applications parameters such as increased FOV, long working distance and high collection efficiency are often more important than sub-micron optical resolution. To achieve FOVs greater than a square millimeter, it is necessary to use low magnification objectives (2.5 to 5X) which have poor collection efficiency due to their small numerical apertures (0.16-0.28). For example, a 0.28 NA objective lens collects less than 6% of the fluorescence that a 20x/0.95 objective collects.

Several schemes have been devised to increase the collection efficiency of a multiphoton microscope. For example, transmission detection can increase the amount of light collected from thin samples. This scheme has been further improved by the use of parabolic mirrors in a clever design that directs fluorescence back towards an epi-positioned detector (Combs *et al.*, 2007). However, these options are not applicable when imaging live animals or thick specimens. A novel hybrid reflecting objective lens has been proposed (Vucinic *et al.*, 2006) that also promises increased collection, but it has not yet been implemented. Recently it has been demonstrated (Engelbrecht *et al.*, 2009) that surrounding a 40x/0.8 NA lens with light guiding fibers can increase the amount of signal collected by a factor of 2. We further expand on this idea by applying it to the Olympus XLFluor 4x/0.28 where it has a profound effect on the image collection.

Materials and Methods

Circumferential Ring Detector

We have designed a series of light guide based detector devices which (depending on the lens and imaging depth) can increase the amount of light collected by as much as 20 fold yet provide a 3-4 mm wide FOV. The devices consist of a ring of high transmission liquid light guides placed around the front lens the objective lens at an optimal collection angle. We refer to this device as a Circumferential Ring Detector (CRD). A series of CRDs were machined from white reflective Delrin for different objectives commonly used for *in vivo* imaging in our laboratory. The device holds five high transmission liquid light guides close to the sample at an angle normal to the collection sphere of the objective lens (Figure 1a). Whereas other similar collection-enhancing designs employ multimode fiber optics (Engelbrecht *et al.*, 2009) we elected to use high NA liquid light guides because of their superior scattered light collecting ability. Light guides have a larger diameter than conventional silica fiber optics and collect a higher percentage of scattered emission. Although it would be possible to use a large number of optical fibers and collect from a similar surface area of the collection sphere, there would still be high packing losses from the regions between the fiber cores that do not propagate light. Secondly, liquid light guides have a larger high numerical aperture than typical fiber optics (~0.5 vs. ~0.2) which improves detection of highly scattered light generated in deep multiphoton imaging. To confirm the superior performance of light guides over optical fibers for collecting highly scattered light we examined the collection characteristics of light guides and a number of different fibers (Table 1). Light guides under test were positioned at an exit port of an

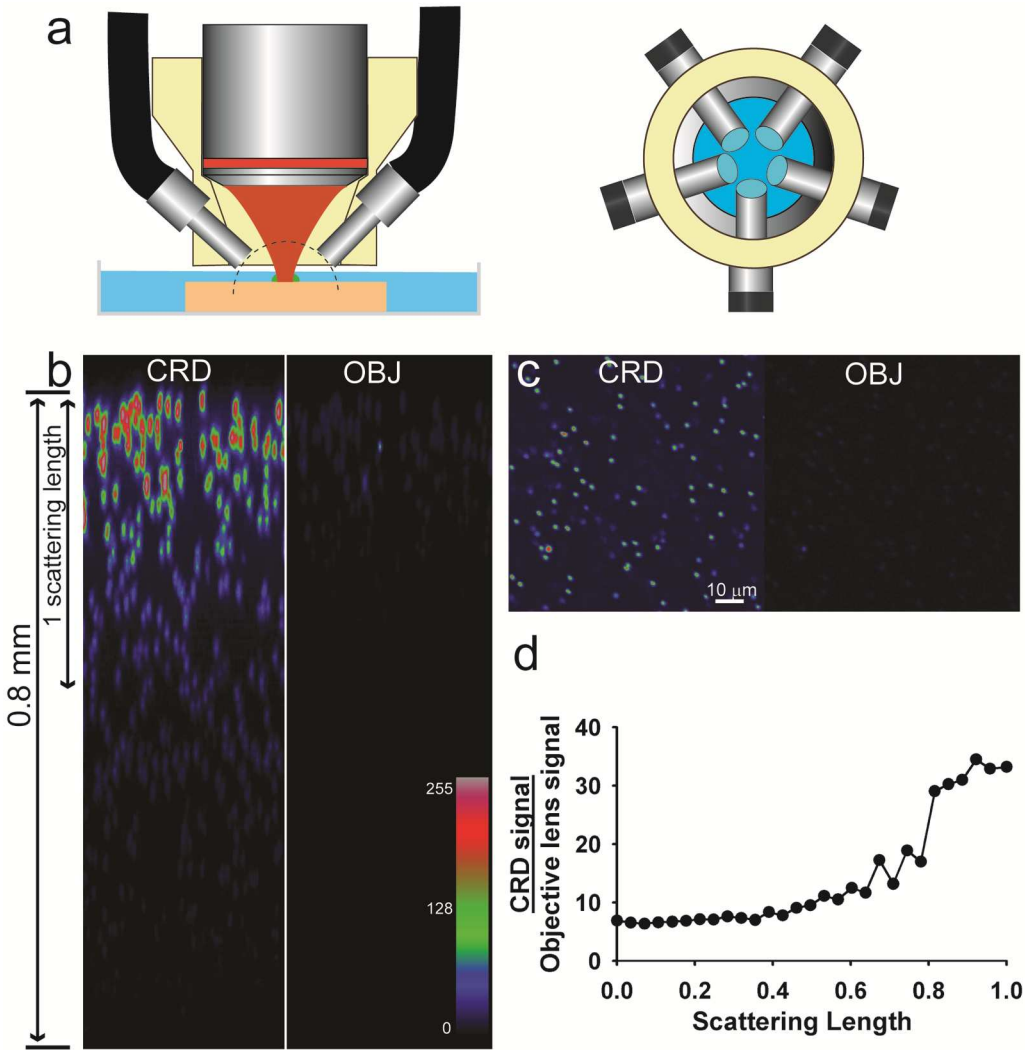

Figure 2.1 – CRD design and imaging depth comparison in scattering gels. (a) Side and bottom view of low NA objective device. (b) XZ images of 1 µm green fluorescent beads in 5% aragrose with added non-fluorescent beads as scatterers. One scattering length at λ=520 nm is indicated at the left. Excitation was at 880 nm delivered through an Olympus 4x/0.28 objective lens. 100 frames (384 x 512 pixels) were collected using a 10 µm step in z; pixel integration time was 3.0 µs. (c) Surface (XY) image by CRD and OBJ channels. (d) Change in the collection enhancement as a function of scattering length. One scattering length corresponds to ~350 microns into the gel. Values are the average ratio of the amplitudes from Gaussian fits of in-focus fluorescent beads from each slice (see text).

integrating sphere (Thorlabs IS200, Newton, NJ) which was illuminated by an attenuated, filtered (575/150 nm bandpass) halogen light source coupled into the integrating sphere input port. Using photon counting (Stanford Research SR400, Sunnyvale, CA), we measured the number of photons incident on a PMT at the opposite end of the light guide under test. The liquid light guide significantly outperformed the fiber counterparts in the collection of highly scattered light, even after the signal was scaled relative to the area of the transmitting core.

Table 2.1 – A comparison of the collection efficiency of various optical waveguides based on their ability to transmit visible (500-650nm) light radiated from an integrating sphere. Here the photons counted are presented normalized to those detected from the liquid light guide and then relative to their core area.

Fibre	Diameter (μm)	NA	Normalised Counts	Normalised Counts/mm^2
Oz Optics QMMJ-UVVIS-200/240	200	0.22	5.68E-04	0.37
Thorlabs -M1705	200	0.22	7.43E-04	0.48
Ocean Optics -P1000-2-UV-VIS	1000	0.22	1.38E-02	0.36
Thorlabs -M31L01	62.5	0.28	3.30E-05	0.22
Thorlabs -M2001	400	0.39	4.37E-03	0.71
Thorlabs -M2101	600	0.39	1.07E-02	0.78
Newport Liquid Light guide 77636	5100	0.52	1.00E+00	1.00

The output ends of the light guides are held bundled together by a machined mount and deliver the collected light through an emission filter directly onto the photocathode of the photomultiplier tube (Hamamatsu HC125-02, Bridgewater, NJ, USA). Quantitative comparisons in imaging mode were made by using two PMTs (Hamamatsu HC125-02, Bridgewater, NJ, USA) with ~identical dynode gains and QEs as determined by photon counting at low light and comparison of their single photon pulse heights (at -900 v). These two PMTs were used for all imaging experiments and pixel intensities can be compared directly.

Murine Brain Slices

Hippocampal brain slices, 300 μm-thick, were prepared from 1-month old ICR wild type mice using procedures described previously (Kwan et al., 2008). All preparations were performed in accordance with Cornell University animal use regulations (IACUC protocol 00-46-03). 50 mg of Fluo-3 AM (Invitrogen) was dissolved in 4 μL of DMSO with Pluronic F-127 (20% by weight, both from Sigma-Aldrich). This dye solution was diluted with a buffer solution, consisting of 150 mM NaCl, 2.5 mM KCl, 10 mM HEPES, to make a final dye concentration of 5 mM. The brain slice was incubated in the dye solution at room temperature for ~10 min, and then rinsed with Ringer's solution before imaging.

Spinal Cord Segments

Spinal cord segments were prepared from *Hb9*-GFP transgenic mice originally generated by Dr. Thomas Jessell (Wichterle et al., 2002). In the lumbar segments of the spinal cord, this transgenic line selectively labels motor neurons and a small group of ventromedial interneurons (Wilson et al., 2005). For the whole spinal cord preparation, P1-P3 *Hb9*-GFP mice were

euthanized by decapitation and their spinal cords were removed by laminectomy. The ventral meninges were completely removed and the spinal cord was pinned, ventral-side up, in a Sylgard-filled dish.

Murine Tumor Model

An ascites cancer model of ovarian metastasis was examined. This was developed at Cornell University in the laboratory of Dr. Alexander Nikitin by harvesting ovarian surface epithelia from FVB mice. This OSN3 cell line was generated from these cells by cre-mediated deletion of Rb and p53 tumor suppressors. To initiate peritoneal tumors,10^7 OSN3 cells were injected IP into FVB mice. Tumors developed within the peritoneal cavity in one to two months after injection. Mice that displayed signs of sickness were euthanized and the identified tumors were pinned in a Sylgard-filled dish in saline buffer.

Results and Discussion

Our design positions the 5 mm diameter faces of the light guides ~9 mm from the 4x/0.28 macro lens focus to maintain a practical working distance of ~2 mm. This reduces the angular collection of each guide relative to its acceptance angle and results in a collection NA of ~0.27 for each 0.52 NA light guide. Based on fractional solid angle, each light guide would collect about the same fraction of isotropic emission as the 0.28 NA objective (~ % per guide) and the five light guides together would be expected to collect 4.7 times more fluorescence light than the 4x/0.28 objective. To quantify the photon fluxes acquired by the two collection pathways (CRD and OBJ) we measured photon counts directly by photon counting while focused onto a pool of fluorophore. This value varied slightly each time the device was reassembled, with values ranging from 5.9

to 7.1, for an average ratio of 6.3±0.2 (n=6) times more light than the objective lens in the absence of scattering, higher than predicted by solid angle alone. We attribute this increase to the reflective surfaces of the CRD ring and collection of scattered signal is even further enhanced by the CRD device relative to the objective lens. To quantify the level of enhancement we imaged 1 μm fluorescent microspheres embedded in 5% agarose gel which also contained non-fluorescent 1 micron polystyrene beads as scatterers (Figure 1b). Under these conditions, a CRD device mounted on a 0.28 NA lens collected > 20 times more light than the objective (Figure 1d). Figure 1d was obtained by fitting bead images from the CRD channel to a 3D Gaussian function and using the centroid to locate the corresponding bead in the objective lens collection channel image to quantify the signal from the equivalent region in the objective lens image. Values plotted are the ratios of the two signals as a function of sample scattering length at 520 nm. In these experiments the laser power out of the objective was held constant during the z-stack acquisition. Although epi-collected signal was too low to accurately compare at deeper than ~0.8 scattering lengths, there is a remarkable enhancement of collection in scattering samples.

For the Olympus XLFluor 4x/0.28 objective used for our large field-of-view imaging, the diffraction-limited resolution at 880 nm would be ~1.2 and ~14 microns (lateral and axial FWHM respectively). However, the 25 mm back aperture of the objective is underfilled by the excitation beam and measured PSF values from the bead data (Figure 1c) yielded a 2.2 micron lateral FWHM and an axial extent of ~23 microns for both the CRD and objective lens signals. This level of resolution is sufficient for many

applications such as monitoring cell trafficking or calcium activity across large areas, or imaging large scale tissue morphology. Based on the collection efficiency obtained, our 4x macro system with CRD attachment has an effective "collection NA" of ~0.55 in the absence of scattering and as high as 0.8-0.9 deep in scattering samples.

Use of our CRD device increases the signal-to-noise ratio, allows for imaging at lower laser powers which is critical in many *in vivo* and live tissue imaging experiments, or for faster imaging since more photons are collected per pixel at a given frame rate. When implemented on a low NA objective the CRD can acquire signals not otherwise obtainable with low NA objective epi-collection alone. Figure 2 shows two applications where the CRD produces significant improvement. For example, it is possible to follow calcium signals over large regions hundreds of microns deep using our system (Figure 2a-d). Intrinsic tissue signals such as NADH fluorescence and collagen second harmonic generation (SHG) are useful in many studies, but are weak and difficult to impossible to image with low NA optics. With the CRD we can obtain overall 3D resolved images of tumor structure using intrinsic signals alone. Figure 2e shows a projected image stack from a ~3x3 mm square region 1.2 mm deep through the tumor and into the peritoneum on which the tumor is attached. The only signal collected by the low NA objective (at the laser power used) is the collagen network of the surface peritoneum, a much stronger signal than tissue autofluorescence. The CRD collects the tissue autofluorescence, but little collagen SHG signal due a 420LP filter on the entrance glass of the light guide (this coating is optional and the raw light guides transmit light down as low as 340nm). The

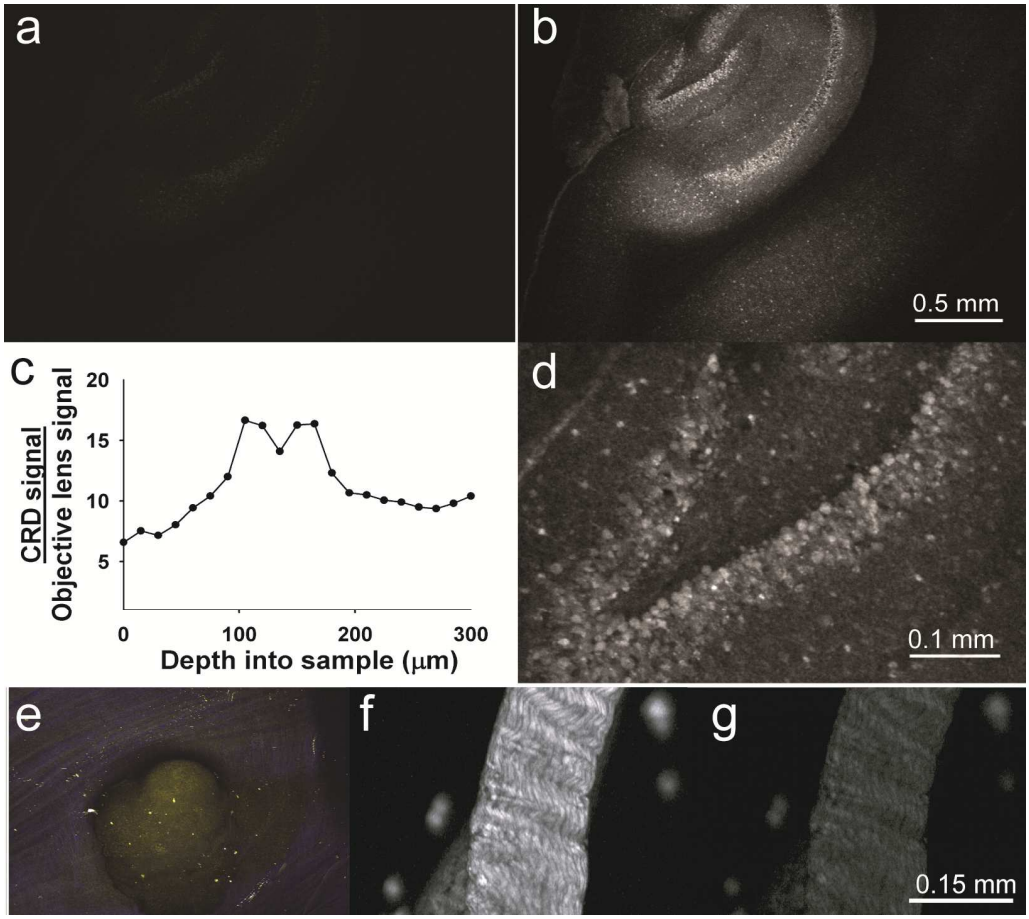

Figure 2.2 – Large field of view multiphoton imaging. (a, b) Single optical sections from 150 microns into a Fluo-3 loaded mouse brain slice from the OBJ (a) and CRD (b) channels. Excitation at 820 nm (~100 fs) was delivered through the 4x/0.28 NA objective; emission 370-600 nm. Power was set to avoid saturated pixels at the surface (~100 mW) and held constant while acquiring the z-stack. (c) CRD signal enhancement as a function of depth into a scattering sample (brain slice). Plotted values represent the average of the ratios between CRD and corresponding OBJ pixels after background subtraction. (d) Higher zoom CRD image of the dentate gyrus region of the hippocampus. (e) Large FOV multiphoton imaging of an unstained ascites tumor in mouse (exc. ~100 mW at780 nm, 370-550 nm em). The merge shows epi-channel (blue) and CRD signal (green) – in this case the SHG at 390 nm is not transmitted through the light guide because of a 420LP optical filter. Mouse tail collagen and fluorescent beads were imaged at 880nm to examine any difference in fluorescence collection. (f) Collection through the CRD (g) the same image Epi-collected showed preferential collection of SHG in the CRD channel, when normalized to the fluorescence.

combination of these two channels allows for the ready discrimination of the tumor mass.

Collagen has become increasingly important as a potential diagnostic tool for tissue pathologies, and differential SHG signals based on collection geometry may prove useful for distinguishing morphological changes associated with disease states or tissue damage. While fluorescence emission is isotropic; however, SHG is anisotropic and dependent on the geometry of collagen fibrils in the sample (Zipfel et al., 2003a; Williams et al 2005). To determine whether there were any observable differences between the ability of the two channels to detect SHG, we imaged (Figure 2f,g), at 880nm, a sample of mouse tail tendon in saline solution, alongside 15μm fluorescent beads (Polysciences). Here the fluorescence from the beads served to standardize the comparison between the two channels. The ratios of the collagen SHG to bead fluorescence to in each channel were computed. These showed a 31 ± 5% (n=5) enhancement in SHG collection in the CRD channel relative to the Epi after both channels had been calibrated for transmission differences. This difference was consistent enough to argue the potential use of this system as a means of examining tissue pathology, although just how the disease-state will change this ratio remains to be determined. We note that although the average power used in some of our CRD macro lens experiments is on the order of 100 mW (e.g. for intrinsic tissue fluorescence imaging), the spot size is much larger and the intensity at the focus is 47 times lower than it would be with a typical high NA objective at 100 mW.

For high NA objective lenses such as the 25x/1.05 Olympus lens, the relative collection increase by a CRD device is more modest. Photon

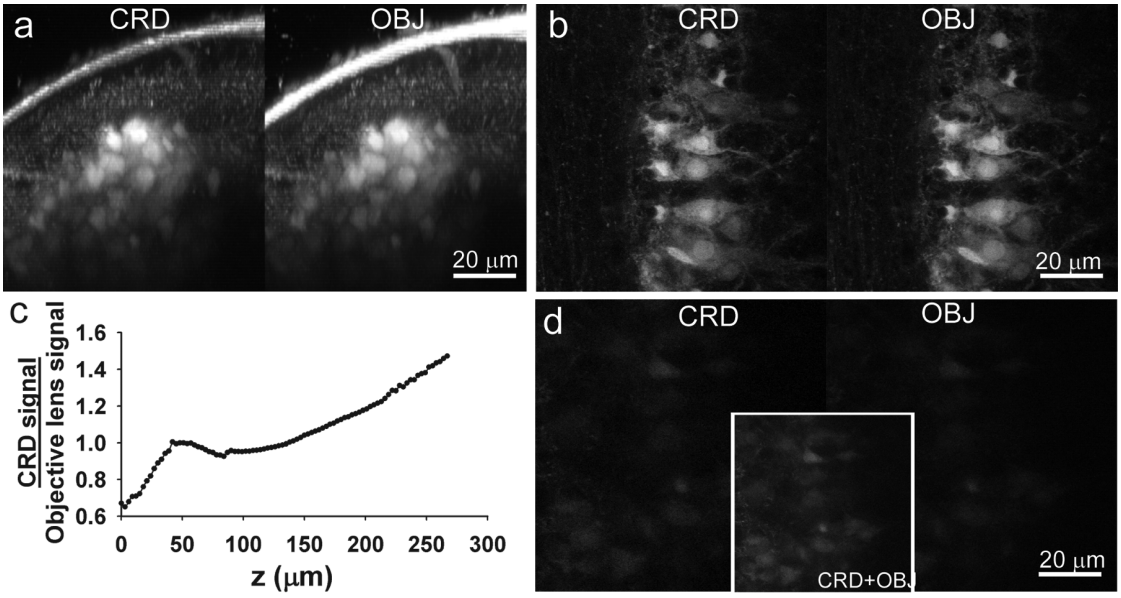

Figure 2.3 – CRD used with a high NA physiological objective. (a) Projected XZ images of GFP expressing motor neurons in mouse spinal cord acquired by the CRD and objective lens. (b) XY sections from 150 μm. (c) Ratio of CRD pixels to objective collected pixels (background subtracted). (d) CRD and objective collected images at 230 μm. Insert shows the summed image. Excitation was at 880 nm. Power was set to avoid saturated pixels at the surface (20 mW) and held constant while acquiring the z-stack. Images (768x512) were acquired with a 1.5 μs pixel time and without frame averaging.

counting measurements made using a CRD device designed around the Olympus 20x/0.95 and 25x/1.05 objectives resulted in a CRD signal that was typically 30-60% of the high NA objective signals at the surface. However this additional signal would have otherwise not been collected and represents an overall 10-20% improvement in the signal-to-noise ratio (SNR). Furthermore, when imaging deep in a scattering specimen the light collected by the CRD can exceed that collected by a high NA objective lens. Our results using high NA objectives are similar to a recent report (Engelbrecht et al., 2009) where a number of large core plastic fibers were used around a 0.8 NA lens. An example of the level of enhancement we found using a CRD device in a high NA objective is shown in Figure 3. When imaging GFP expressing neurons in the mouse spinal cord preparation, the CRD collected slightly less signal at the surface (Figure 3a), but equal or higher signal deep in the sample (Figure 3c). By summation of both the signals, use of the CRD device provides a square root two or higher increase in the SNR.

In conclusion, we have developed a simple external light collection scheme well suited for in vivo imaging that can gather as much as 20 times more signal then that acquired by the objective lens when imaging with low NA objectives deep in tissue. Data taken using the prototype devices described here demonstrate the utility of the idea and we are currently exploring more streamlined implementations, such as a design consisting of two semi-circular halves that surround the objective and funnel light into two light guides. The technique is particularly useful in experiments requiring a large FOV where it overcomes the poor light collection of low NA objectives. However, even when implemented on high NA

physiological objectives such as the newer Olympus and Zeiss 20-25x water immersion lens, significant collection increases can be obtained in scattering tissues.

Acknowledgements

This work is supported by the National Institutes of Health (NCI R01 CA116583 and NIBIB P41 RR04224 to WRZ). We wish to thank Andrea Flesken-Nikitin and Dr. Alexander Nikitin for assistance with establishing the mouse models of ovarian metastasis, and Dr. R. Harris-Warrick for the *Hb9*-GFP transgenic mice.

REFERENCES

Combs C, Smirnov A, Riley J, Gandjbakhche A, Knutson J, Balaban R, Optimization of multiphoton excitation microscopy by total emission detection using a parabolic reflector. J. of Microscopy **228** 330-337 (2007)

Denk W, Strickler JH, and Webb WW, Two-photon laser scanning microscopy," Science **248**, 73-76 (1990)

Engelbrecht CJ, Göbel W, and Helmchen F, Enhanced fluorescence signal in nonlinear microscopy through supplementary fiber-optic light collection. Optics Express. **17** 6421-6435 (2009)

Göbel W and Helmchen F, In vivo calcium imaging of neural network function. Physiology 22 358-65 (2007)

Kwan AC, Dombeck DA, & Webb WW, Polarized microtubule arrays in apical dendrites and axons. Proc. Natl. Acad. Sci. USA **105**, 11370-11375 (2008)

Miller MJ, Wei SH, Parker I, and Cahalan MD, Two-photon imaging of lymphocyte motility and antigen response in intact lymph node Science **296** 1869-73 (2002)

Oheim M, Beaurepaire E, Chaigneau, E, Mertz J, and Charpak. S, Two photon microscopy in brain tissue: parameters influencing the imaging depth. J. Neuroscience Meth. **111** 29-37 (2001)

Vucinic D, Bartol T, and Sejnowski T Hybrid reflecting objectives for functional multiphoton microscopy in turbid media. Optics Let **31** 2447-2449 (2006)

Wichterle H, Lieberam I, Porter JA, & Jessell TM, Directed differentiation of embryonic stem cells into motor neurons. Cell **110**, 385-397 (2002)

Williams RM, Zipfel WR, & Webb WW, Interpreting second harmonic generation images of collagen. I fibrils. Biophys J. **88** 1377-1386 (2005)

Williams RM, Zipfel WR, Tinsley ML, & Farnum CE, Solute transport in growth plate cartilage: in vitro and in vivo. Biophys J. **93** 1039-50 (2007)

Wilson JM, et al. Conditional Rhythmicity of Ventral Spinal Interneurons Defined by Expression of the Hb9 Homeodomain Protein. J. Neurosci. 25, 5710-5719 (2005)

Zipfel WR, Williams RM, Christie R, Nikitin A, Hyman BT, & Webb WW, Live tissue intrinsic emission microscopy using multiphoton excited native fluorescence and second harmonic generation. PNAS, **100,** 7075-7080 (2003a)

Zipfel WR, Williams RM, & Webb WW, Nonlinear magic: multiphoton microscopy in the biosciences. Nat Biotech. **11,** 1369-77 (2003b)

Chapter 3 - A Multiphoton Objective Design With Incorporated Beam Splitter for Enhanced Fluorescence Collection[1]

Abstract

We present a *de novo* design of an objective for use in multi-photon (MPM) and second harmonic generation (SHG) microscopy. This objective was designed to have a large field of view (FOV), while maintaining a moderate numerical aperture (NA) and relative straightforward construction. A dichroic beam splitter was incorporated within the objective itself allowing for an increase in the front aperture of the objective and corresponding enhancement of the solid angle of collected emission by an order of magnitude over existing designs.

Introduction

Multiphoton microscopy (Denk et al., 1990; Zipfel et al., 2003) has developed into a standard tool for the life scientist with far reaching applications ranging from basic cell biology to imaging physiology and disease progression in live animals. This robust form of laser scanning microcopy is ideal for experiments in which cellular and sub-cellular resolution fluorescence imaging is required in a highly scattering medium. As the technique has advanced there has been a corresponding development of new objective lenses specifically for use in multiphoton microscopy. These new designs have increased IR transmission and obtained high numerical apertures (NA) at relatively low magnification (e.g. Olympus

[1] McMullen JD and Zipfel WR "A Multiphoton Objective Design With Incorporated Beam Splitter for Enhanced Fluorescence Collection" Opt. Express **18,** 5390-5398 (2010)

25x/1.05 NA, Zeiss 20x/1.0 NA). Other collection schemes, which exploit the principle that all of the collected emission light in MPM – even the scattered photons – contribute to useable signal (Theer and Denk, 2006), have increased the overall solid angle sampled by implementing additional collection optics such as a parabolic reflector underneath the tissue (Combs et al., 2007), or a ring of waveguides surrounding it (McMullen et al., 2009, Engelbrecht et al, 2009). High NA reflecting objectives have also been designed and demonstrated to efficiently collect fluorescence (Vucinic et al., 2006).

Although high numerical aperture is important to achieve the highest resolution, there are cases in which the experimenter is willing to sacrifice resolution for an increase in the field of view (FOV), for example in cell tracking experiments in tissues, or for observations of calcium oscillations in a large neuronal networks. Additionally, a wider field of view would be particularly useful for "multiphoton pathology" applications. The translation of MPM from the laboratory to the operating room is currently underway with various research groups developing the first generation of MPM endoscopes (Lelek et al. 2007; Fu et al., 2005; Gobel et al., 2004) in the hopes of soon being able to perform *in vivo* optical biopsies. The direct MPM imaging of fresh unstained biopsy tissue has been demonstrated (Zipfel et al., 2003; Rogart et al., 2008; Mukherjee et al., 2009) to provide instant histological grade images without the tedious preparation necessary to produce standard sectioned slides, and one day may become an indispensable part of clinical practice. In addition, the intrinsic contrast provided both by autofluoresence from endogenous fluorophores such as NADH, flavins and other autofluors, as well as second harmonic generation

from such macromolecules as collagen, adds information beyond morphometric parameters. However, some of these signals are weaker than typical dyes by several orders of magnitude (Zipfel et al., 2003), and it is therefore critically important to maximize the collection optics for this particular application.

As existing technology has been focused on higher numerical aperture objective designs with fields of view under a millimeter, we decided to develop a new objective design motivated by the following requirements: (1) large field of view; (2) long working distance; (3) a sufficient numerical aperture for reasonable optical sectioning and single cell resolution; (4) collection of as large of a solid angle as possible; (5) an inexpensive design to fabricate; and (6) chromatic correction over at least the bandwidth of a typical femtosecond pulse (10-15 nm).

Based our own large field of view multiphoton imaging needs, we determined that the objective should have a FOV of at least 4 mm at zoom 1 on our scanning microscopes. In addition, the working distance needs to be at least 2 mm. Although that is more than twice the imaging penetration depth of an MPM system, a larger working distance becomes necessary when imaging the irregular surfaces common in tissue and live animal imaging cases. Again based on the needs of typical large FOV imaging experiments, we imposed the requirement that the axial FWHM of the two-photon focal volume be no more than 10 microns maximum, roughly the thickness of a cell layer. For an objective lens of a NA < 0.7, in an immersion medium of refractive index n, the dimensions (and so the sectioning capability) of the two-photon focal volume can be given as (Zipfel et al., 2003):

$$\omega_{x,y} = \frac{0.32\lambda}{\sqrt{2}NA} \quad , \qquad \omega_z = \frac{0.532\lambda}{\sqrt{2}}\left[\frac{1}{n-\sqrt{n^2-NA^2}}\right] \tag{1}$$

where $\omega_{x,y}$ and ω_z are the lateral and axial 1/e waist of the focal volume for a given wavelength λ. Using these equations we determined that our minimum resolution specification was met by an NA of ~0.3 in air and ~0.35 for an objective designed to be immersed in water. The upper limit on objective NA is also set by the size of the lens back aperture. We set a design threshold of no more than 25 mm for the diameter of this stop, which we can reasonably accommodate in our scanning systems using a scan lens/tube lens combination that produces a ~12x increase in the laser beam diameter to provide a nearly overfilled back aperture. Although this reduces our scan angle, this lens design achieves a large FOV at relatively small field angles.

To maximize the objective's ability to collect emissions, we increased the acceptance solid angle by enlarging the diameter of the front aperture. An infinity corrected fluorescence objective is designed to collimate light originating from its focal plane so that that it can be translated onto a distant image plane and, as a result, the diameter of its front aperture is dictated by its working distance and NA. However, by incorporating a dichroic element into the objective itself, the need to collimate this light in order to send it to a distant detector can be relaxed. This allows for an increase in the size of the front aperture of the objective as well as the application of a reflective coating to the interior of the objective casing, both of which boost the collected solid angle far in excess of what one would predict based on NA alone. Our design effectively decouples the excitation and emission paths within the objective lens.

Throughout the design process an effort was made to limit the fabrication cost of the system. The number of lens elements was kept as low

as possible – 3 for the air objective with the addition of one additional meniscus lens element to compensate for aberration when water was used as an immersion medium (Shimizu and Takenaka, 1994). No aspheric surfaces were used, though they could be implemented to further increase the field of view of the system or the NA. All glasses are stock and were selected to minimize fabrication cost. Only two glass types were used in the two designs (Schott SF2 and Schott NSK16).

The objective lens was designed to deliver excitation light centered at 780 nm with all of the optics having a default ¼ wavelength magnesium fluoride coating. The system was designed to support a bandwidth of greater than 10 nm (775, 780, and 785 nm all being equally weighted during calculations). Although the reference wavelength was 780 nm, the objective performed well throughout the range of the Ti:Sapphire laser, with only a small relative shift in the focal plane occurring for different excitation wavelengths (e.g. ~35 μm at 880 nm). Although dispersion due to the focusing elements and beam splitter might appear to be problem at first glance, this design is not substantially more dispersive material than other lenses of similar NA and FOV (Kazuhiro, 1999) based on total glass thickness. With the current trend of pre-compensation systems being incorporated into commercial Ti:Sapphire lasers (e.g. Spectra Physics DeepSee) it should be possible to deliver transform limited pulses through it.

Design

The ray tracing software Code V (Optics Research Associates, Optics Research Associates, Pasadena, CA) was used to design both an air and a water immersion version of the lens (figure 3.1) whose properties are

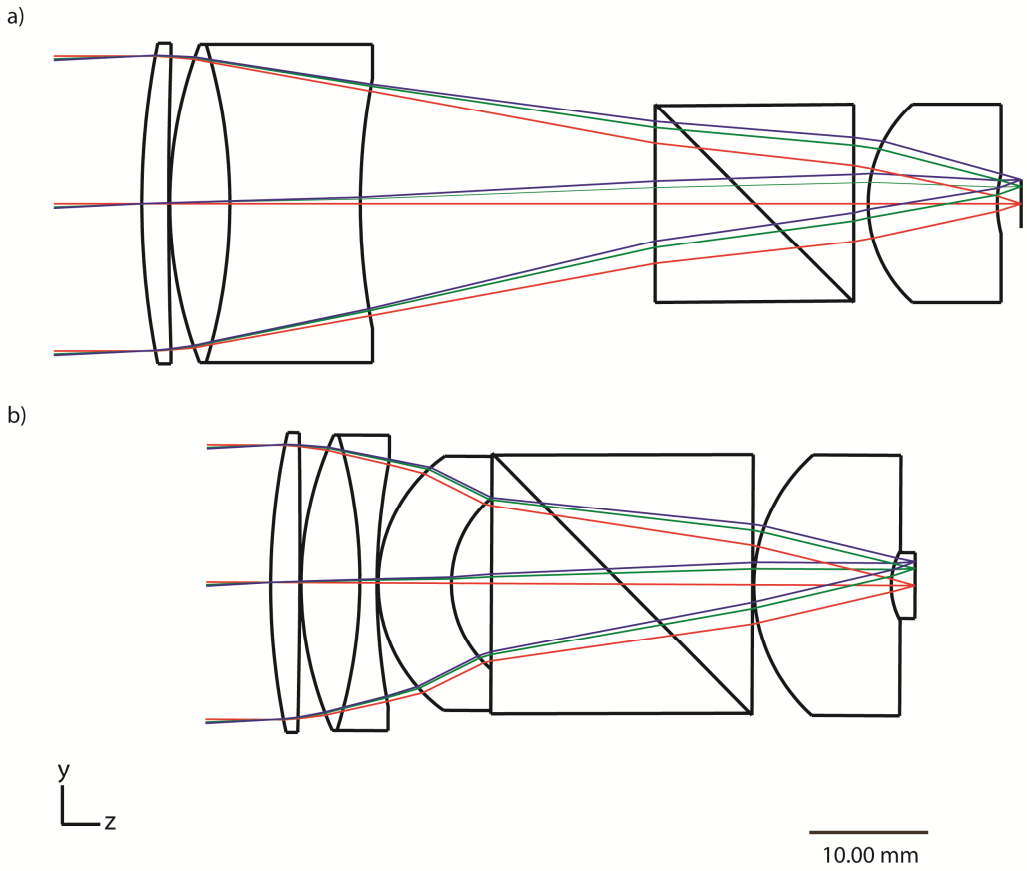

Figure 3.1 - The design of an objective incorporating a beam splitter to efficiently decouple the excitation and collection path (a) air immersion, (b) water immersion

summarized below (table 1). The air immersion lens had an NA of 0.3 and a full FOV of 4 mm from an input field angle of ±2.8º. The water objective requires a beam tilt of ±3.5º to cover its full field of view, but the higher index of refraction of water increases the numerical aperture to 0.35 and slightly decreases the diameter of the back aperture. Both lenses have a working distance of 2 mm. An emission-splitting plate dichroic placed directly after the front lens was found to severely degrade the point spread function, however a dichroic coated beam splitting cylindrical wedge incorporated into the lens design at that point produced no significant degradation after optimization (Smith 2000). The emission diverting optic is large, matching of the typical diameter of a photomultiplier tube (PMT)

Table 3.1 - A Summary of Objective Lens Parameters

Immersion Medium	Back Aperture	NA	Input Y Field Angle (º)	Y Position at Focus	Strehl Ratio
Air	24.8	0.30	0	0	0.963
			2	1.43	0.971
			2.8	2	0.869
Water	23.1	0.35	0	0	0.885
			2.5	1.43	0.868
			3.5	2	0.812

photocathode (~20 mm). However, the rays at this point could also be efficiently coupled into a high NA, high transmission light guide for example to direct to a more distant multichannel detection system.

The performance of the lens is close to the diffraction limit. The composite Strehl ratio (table 1), consisting of all three equally weighted wavelengths, meets the *Marechal* criterion for each lens for all three calculated angles, indicating effectively diffraction limited performance across the field. This is confirmed by the modulation transfer functions (MTF) (figure 3.2 a,d) for both designs where the tangential and radial components of each

field approximate the diffraction limited curve. The MTF shown in figure 3.2 was calculated based on the single photon PSF; the MTF is further improved using two-photon excitation and the two-photon PSFs at the extreme of the field of view (figure 3.2 b,e) were found to be effectively diffraction limited. Small amounts of aberration (mainly coma) in the single photon point spread function are minimized by the squaring of the PSF. Finally, the field curvature for both the lenses (figure 3.2 c,f) was calculated and found to be within the axial FWHM, with fairly good overlap between the tangential and sagittal rays indicating minimal astigmatism.

Analysis

In order to assess the overall collection efficiency of our lens design we conducted Monte Carlo simulations using the non-sequential ray tracer LightTools (v6.3 Optics Research Associates, Pasadena, CA). This allowed us to calculate the overall "collection numerical aperture" of our lenses which was different than numerical aperture of the excitation focusing pathway. We compared these designs to the Olympus 4x XLFLUOR, a commercially available macro objective with an NA of 0.28 – approximately 1.75x the typical NA of a standard 4x. This macro lens has been our primary objective lens for large FOV multiphoton imaging in our lab. The lens model we used for our comparison was based on the design shown in the Olympus patent (Kazuhiro, 1999) and had a slightly smaller NA (0.265) and working distance (28.1 mm) compared to the commercially available Olympus 4x macro objective (NA=0.28 and WD=29.5 mm). Another minor difference in the design shown in the patent was that it was corrected for a sample immersed in 6 mm of water rather than the 5 mm water layer

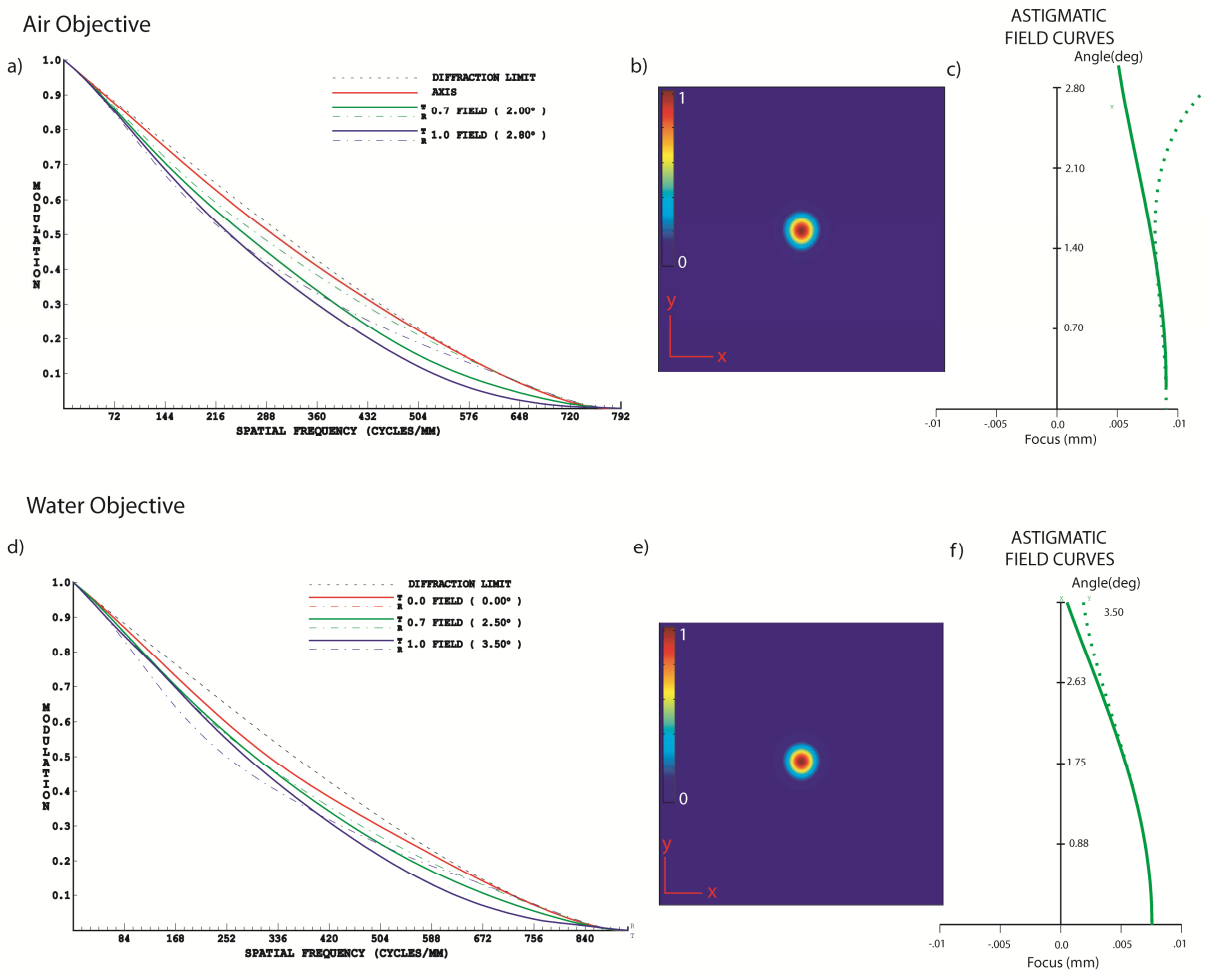

Figure 3.2 Characterization of the excitation transmission for the air and water immersion objectives (a,d) modulation transfer function (b,e) two photon PSF at the greatest field angle - scale bar = 2μm (c,f) field curvature at the edge of the field for the tangential (dashed) and sagittal (solid) surfaces.

the commercially available 4x objective is designed around. The three objective lens designs (our air and water designs, and the Olympus 4x) were imported from Code V into LightTools (figure 3.3) and an enclosure was placed around the system with an opening for the detector (receiver surface - figure 3.3a) which was placed perpendicular to the optical axis (only one detector side of the objective enclosure was set to be reflective at and below the beam splitter (figure 3.3d) and the lateral edges of the optical components were assumed to be transmitting. In the case of the Olympus objective simulation a 2" square dichroic mirror was placed 10 cm along the optical axis away from the back aperture. This was focused into a receiver of 20 mm diameter (the size of our PMT photocathode) by a lens 40 mm wide. This simulation is similar to our current large FOV multiphoton imaging systems. It should be noted that for the case of these simulations the coating on both the internal dichroic as well on the external dichroic was set to be 100% reflective. In order to assess the effective collection NA (NA_c) of the objectives in their respective immersion media (without any scattering), we first examined the collected fraction of photons from an isotropically radiating 587 nm point source located at the intersection of the optical axis and the focal plane. By equating this to the fraction of total solid angle, it is possible to derive the equation for the numerical aperture of collection:

$$NA_c = n\sin\left(\cos^{-1}(1-2\Phi)\right) \qquad (2)$$

where Φ is the fraction of the total radiated photons that were incident on the detector. The values of NA_c as displayed in Table 2 were found to be

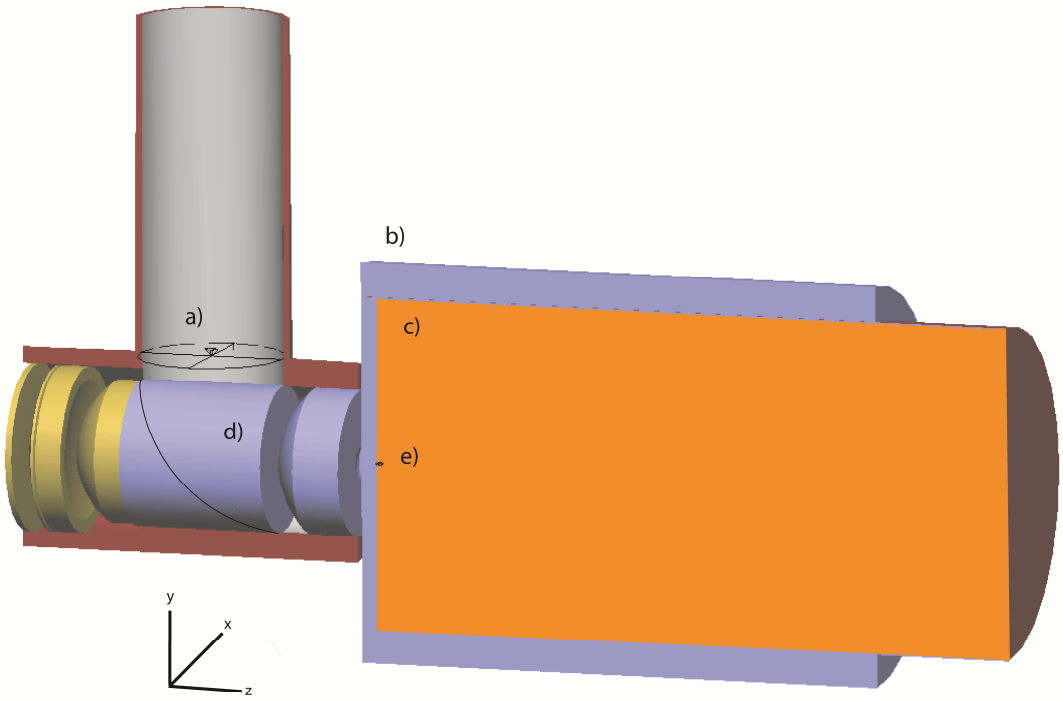

Figure 3.3 A cross-section of the water immersion objective modeled using LightTools a) receiver b) water c) tissue slab d) beam splitter e) point source (scale bar ≈1 cm)

greatly enhanced for the new objectives due to the acceptance of the large front aperture and the internal dichroic.

Table 3.2 - A Summary of The Lenses' Numerical Apertures

Objective	Calculated Numerical Aperture (NA)	Observed Numerical Aperture (NAc)
Olympus 4x	0.27	0.27
Air Objective	0.3	0.82
Water Objective	0.35	0.98

The objectives were also compared for their ability to collect light from a scattering sample. In this case, a cylindrical tissue slab 50 mm in diameter and 100 mm long (figure 3.3c) was constructed as a volume scatterer using a Mie scattering model at a wavelength of 587 nm. The scattering mean free path and anisotropy factor g for the tissue were set to 0.05 mm and 0.95 respectively, with a bulk refractive index of the material being 1.33. A small amount of absorption at 587 nm was also included in the model, corresponding to a transmittance per unit length of 0.87 – approximating that of human bladder (Cheong et al., 1990) Light was simulated emitting isotropically from a point source located inside the tissue slab (figure 3.3e). The number of photons collected was assessed at various points in the focal plane, as well as at various depths within the tissue. For the two new objectives, 10^5 photons were simulated, each with a maximum of 10^4 allowed scattering events. For the Olympus 4x objective, 10^6 photons were launched to obtain reproducible results, necessitated by the smaller number of rays that reached the detector surface.

The results from these experiments are plotted in figure 3.4a. Our objective designs collect roughly an order of magnitude more fluorescence

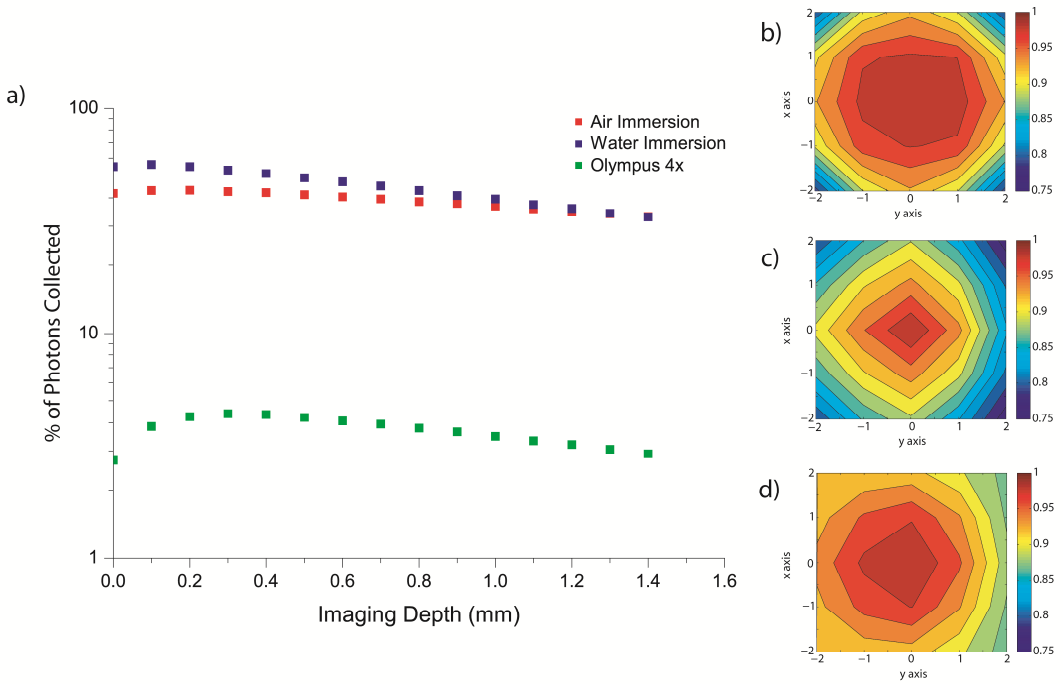

Figure 3.4 Simulated light collection in a scattering material. a) Fractional collection as a function of depth of the (on-axis) photon origin in the scattering material. b-d) Spatial variance in the collection path. Collection of scattered light calculated for differing photon origins positions over the FOV relative to the optical axis. b) Olympus 4x objective with focal plane near surface, c) water immersion objective for focal plane near surface, and d) the water immersion objective with the focal plane 500 μm into the simulated tissue.

than the standard 4x macro lens. It should be noted that the collection of all three objectives was enhanced by scattering from tissue. This occurs in simulation because the depth of the focus is shallow compared to the length of the "tissue", resulting in the bulk of the tissue acting as a mirror to photons that had initially been radiated away from the lens, but are eventually scattered backwards. This effect is dependent on the particular simulation parameters such as number scattering events allowed, sample absorption and length of the simulated tissue. The magnitude of this effect has been shown (Beaurepaire and Mertz, 2001) to increase with the field of view of the lens

We examined spatial variance in the collection path by moving the point source about the focal plane at half integer intervals between -2 and +2 mm, and tallying the number of rays reaching the receiver at each point. The number of counts – relative to the center of the field of view – was observed to fall off for all three objective designs, although the value was above 75% of the maximum in all cases. However, unlike the 4x lens (figure 3.4b) which appeared radially symmetric about the optical axis, the incorporation of the dichroic element created a slight asymmetry in the collection path for both the water (figure 3.4c) and air lenses (not shown, but similar to figure 3.4c). Increased scattering appeared to partially curb this effect for the water immersion lens which improved substantially even at moderate depths (figure 3.4d), although both the air immersion variant and the Olympus lens showed no change of this ratio with depth.

Summary

We have demonstrated a new design for multiphoton objective lenses specifically for use in cases where large fields of view and high collection efficiencies are required. The objective lens designs presented have a 4 mm large field of view, a moderately low, but useable, focusing NA, with an effective collection NA approaching 1. The designs were demonstrated to be highly efficient at collecting fluorescence, especially in the scattering samples typical of multiphoton microscopy. The incorporation of such an objective/detector system on an existing microscope should have immediate impact in experiments such as studies of neuronal network signaling, imaging cell migration in tissues explants and live animals, characterization of engineered tissue constructs and promising new areas such as "instant pathology" based on rapid multiphoton imaging of biopsy samples.

Acknowledgments

This work is supported by the National Institutes of Health (NCI R01 CA116583 and NIBIB P41 RR04224 to WRZ). We would like to thank Olympus Inc for helpful discussions and for providing design information on their 4x macro objective lens, Optical Research Associates for providing Code V and LightTools software packages, and Avtar Singh and Dr. Rebecca Williams for useful discussion and comments.

REFERENCES

Beaurepaire Eand Mertz J, "Epifluorescence collection in two-photon microscopy", Appl. Opt. **41** 5376-5382 (2002).

Cheong WF, Prahl SA, Welch AJ, "A Review of the Optical Properties of Biological Tissues", IEEE J. Quant. Elec. **26** 2166-2185 (1990)

Combs C, Smirnov A, Riley J, Gandjbakhche A, Knutson J, Balaban R, "Optimization of multiphoton excitation microscopy by total emission detection using a parabolic reflector" J. of Microscopy **228** 330-337 (2007)

Denk W, Strickler JH, Webb WW, "Two-photon laser scanning microscopy," Science **241**, pp. 73 – 76 (1990).

Engelbrecht CJ, Göbel W, and Helmchen F, "Enhanced fluorescence signal in nonlinear microscopy through supplementary fiber-optic light collection" Optics Express. **17** 6421-6435. (2009)

Fu L, Gan X, and Gu M, "Nonlinear optical microscopy based on double-clad photonic crystal fibres," Opt. Express 13, 5528-5534 (2005).

Göbel W, Kerr JND, Nimmerjahn A, and Helmchen F, "Miniaturized two-photon microscope based on a flexible coherent fibre bundle and a gradient-index lens objective," Opt. Lett. **29**, 2521-2523. (2004)

Kazuhiro H, Olympus Optical Company, Ltd. "Microscope Objective" Japanese Patent 11-231224 (1999)

Lelek M, Suran E, Louradour F, Barthelemy A, Viellerobe B, and Lacombe F,"Coherent femtosecond pulse shaping for the optimization of a non-linear micro-endoscope" Optics Express, **15** (16):10154-10162 (2007)

McMullen JD, and Zipfel WR, "A Scheme for Increasing the Collection Efficiency of Multiphoton Microscopy," Biophys. J. **96**, 639a (2009)

Mukherjee S, Wysock JS, Ng CK, Akhtar M, Perner S, Lee MM, Rubin MA, Maxfield FR, Webb WW, Scherr DS, "Human bladder cancer diagnosis using Multiphoton Microscopy" Proc. Of *SPIE* **7161,** 716117-1 to 716117-10 (2009)

Rogart JN, Nagata J, Loeser CS, Roorda RD, Aslanian H, Robert ME, Zipfel WR& Nathanson MH. "Multiphoton imaging can be used for microscopic examination of intact human gastrointestinal mucosa ex vivo." Clin Gastroenterol Hepatol **6**(1):95-101.(2008).

Shimizu Y and Takenaka H, "Microscope Objective Design" Adv. Opt. Electron. Microsc. **14** 249-334 (1994)

Smith WJ,"Modern Optical Engineering", (McGraw Hill, 2000) Chapter 13

Theer P, and Denk W, "On the fundamental imaging-depth limit in two-photon microscopy." J Opt Soc Am A Opt Image Sci Vis 23(12): 3139-49, (2006).

Vucinic D, Bartol TM, Sejnowski TJ, "Hybrid reflecting objectives for functional multiphoton microscopy in turbid media," Optics Letters **31**, pp. 2447-2449 (2006)

Zipfel WR, Williams RM, Christie R, Nikitin A, Hyman BT, & Webb WW, "Live tissue intrinsic emission microscopy using multiphoton-excited native fluorescence and second harmonic generation" PNAS, **100,** 7075-7080. (2003)

Zipfel WR, Williams RM, Webb WW, "Nonlinear magic: multiphoton microscopy in the biosciences," Nature Biotech. **21,** 1369-1377 (2003).

Chapter 4 – An Examination of the Intrinsic Fluorescence of Anti-Cancer Drugs and its Application to Two-Photon Microscopy[1]

Abstract

As part of an effort to transition two-photon microscopy from the laboratory into the clinic a collection of anti-cancer drugs (ACDs) used in chemotherapy and possessing strong intrinsic fluorescence were assembled. Their two-photon action cross-sections were measured over the wavelength range of the Ti:Sapphire laser. One of these drugs –Irinotecan - was then selected for use in imaging a metastatic ovarian cancer model. Tumors were visualised with an ACD, producing contrast enhancement by as much as four times for tumors on the uterine horn.

Introduction

Since its discovery in 1990, multiphoton microscopy (MPM) (Denk et al., 1990) has proved a useful tool for *in vivo* fluorescent imaging through its ability to image deeply into scattering tissue with sub-cellular resolution. When combined with the complimentary second harmonic generation (SHG) microscopy, MPM is capable of providing images that rival those from histological slides without fixing and mechanically slicing the tissue to be imaged (Zipfel et al., 2003). This points to clinical applications of MPM in general pathology and the possibility of real time "optical biopsies" either by the immediate multiphoton imaging of fresh biopsy samples, or by in situ imaging using laparoscopic and endoscopic multiphoton instruments. Diagnoses could be made immediately in the operating suite providing

[1] McMullen JD, Williams R, Flesken-Nikitin A, Nikitin A, Zipfel WR, "An Examination of the Intrinsic Fluorescence of Anti-Cancer Drugs and its Application to Two-Photon Microscopy" to be submitted

critical information on tumor phenotype and on the efficacy of a tumor resection by instant evaluation of the tumor border tissue. There are currently several confocal scanning endoscopes (Becker et al., 2007; Kiesslich et al., 2004) on the market that aim to perform this task through traditional single photon fluorescence. However these systems do not have the depth penetration, or the SHG capabilities of a MPM endoscope. The eventual development of a commercial multiphoton based endoscope system is inevitable, and at the time of this publication there are a number of systems in development at various labs throughout the world (Fu et al., 2005; Göbel et al., 2004; Helmchen et al., 2001; Myaing et al., 2006). There are several challenges however that makes the development of a successful multiphoton endoscope far from trivial. First of all, the laser light source used to achieve nonlinear excitation, consists of extremely short pulses of light on the order of 100fs in duration. There are several pulse broadening mechanisms, including group velocity dispersion and self phase modulation, that occur when attempting to deliver pulses this short through a standard optical fibre which would interfere with optimal fluorophore excitation (Ouzounov et al., 2002). Secondly, one of the major advantages of multiphoton over confocal microscopy – that all of the fluorescence is considered a signal – becomes harder to exploit in a miniaturized fiber-delivered instrument, where a non-descanned pathway is difficult to implement. Finally, perhaps the most challenging obstacle involves the transition from the lab to the clinic. As opposed to the myriad of fluorophores available to the microscopist in the lab, there are currently only two contrast agents authorised by the FDA. While tissue auto-fluorescence can be a powerful tool for pathology, it is – with the exception of SHG from

collagen – several orders of magnitude weaker than conventional dyes and its detection *in vivo* in humans, without exposing the tissue to excessive powers, becomes quite challenging.

To this end, we examined a number of popular cancer drugs that also exhibit endogenous fluorescence, in an attempt to characterise them for use as contrast agents in multiphoton endoscopy. Aside from its relevance to cancer imaging, drug auto-fluorescence may be used to study the drug's metabolism in the body, uptake heterogeneity within various cancers, and other pharma-physiological uses for which the high resolution and imaging depth of multiphoton imaging may prove especially useful. For the selection of the drugs under study we relied heavily on the paper by Aaron and Trajkovska (2006), and chose the anti-tumoral drugs 9-aminoacridine, doxorubicin, and ellipticine; the anti-tumor drug coactivator dipyridamole; and the topoisomerase I inhibitors camptothecin and its more water soluble analogue irinotecan. We also examined 5- aminolevulinic acid (5-ALA), the precursor to protoporphryin IX (PPIX), which is used both in photodynamic therapy, as well as for tumor imaging (primarily for barin tumours) due to accumulation of fluorescent PPIX in malignant cells.

Materials and Methods

Cross-Section Measurement

To estimate the effectiveness of the various agents as fluorescent markers, we first measured their two photon absorption spectra across the wavelength range of the Ti:Sapphire laser. As the absolute nonlinear absorption cross-section is difficult to determine due to its infinitesimally small effect on the intensity of the excitation beam, we chose instead to measure the action cross-section following the methods described previously

(Xu and Webb, 1996). The action cross-section is the multiple of the quantum efficiency and the absolute two-photon absorption, and provides a quantification of "molecular brightness" for a given excitation wavelength. In order to speed up the acquisition of what is in general a tedious measurement, we constructed a system centered around a microcontroller which was used: to communicate with a laptop; to control a mechanised rack of up to nine cuvettes (seven samples, one blank, one reference) that were scanned through the focus of an objective (New Focus 20x/0.5 asphere); to monitor excitation power via a light to frequency sensor(Taos inc); to regulate the excitation power via a Pockels Cell (ConOptics) and to count emission photons from the photomultipler tube (PMT) detector (Hamamatsu H7421-40). The automation was completed by using the same software to sweep the wavelength range of a computer controlled Ti:Sapphire (MaiTai, Spectra Physics). Compounds were obtained in powder form from Sigma Aldrich with the exception of PPIX (BIOMOL International). Working concentrations of the solutions were kept below 10 μM to prevent screening effects and were prepared from stock solutions in DMSO or ethanol if the aqueous solubility of the drug was low. The values for particular species were obtained by ratioing the slope of its nonlinear excitation curve to that of a fluorescein standard, while accounting for collection efficiency differences between the two (due to different emission line shapes). The multiphoton emission characteristics were assumed to be the same as the single photon excited spectra, which were recorded *in vitro* using a fluorometer (Photon Technology International).

Murine Cancer Model

To evaluate drug dependent tumor contrast enhancement in vivo, we selected an OSN3 cancer model we had used previously in the lab (Williams et al., 2010), which was developed in the Nikitin laboratory to replicate ovarian metastasis. The OSN3 cell line was generated from harvested ovarian surface epithelial cells that had been modified by a Cre-LoxP mediated deletion of *p53* and *pRb*. Approximately 10^7 of these cells were injected into several week old female FVB/N mice (Charles River), which develop symptoms after approximately six weeks. At this time tumors are present throughout the peritoneal cavity and accompanied with severe exudate ascities and eventual death. Unless stated otherwise, 0.1ml of Camptosar (Pizer - 20mg/ml Irinotecan) diluted with 0.2ml PBS was injected by i.p. into the abdomen of each mouse to give a dosage of ~80mg/kg. This dosage is clinically relevant, and below the high dosages (>150mg/kg) used in other studies (Kunimoto et al., 1987; Allegrini et al., 2004). All mice were euthanized and the tissues removed for imaging 4 hours after injection.

Multiphoton Spectra and Imaging

Multiphoton images were recorded on a converted Bio-Rad MRC600 laser scanning microscope, using a Ti:Sapphire (Tsunami, Spectra Physics) to provide the excitation, a DC680LP (Chroma Tech.) to separate the emission and the excitation wavelengths, and employing lab built detector schemes featuring bialkali PMTs (Hamamatsu HC125) with channels defined by blue glass filter (BGG22), a 575/150 filter and split by a DC500LP dichroic filter (all from Chroma Tech.). Wider-field images were acquired with an Olympus XLFLUOR 4x/.28 objective and higher magnifications obtained with an Olympus UPFLN 20x/.50. To record spectra in tissue samples a 1

mm core collection fibre was used in place of detectors and coupled to a Peltier cooled USB spectrometer (Ocean Optics QE 65000). Tissues containing tumors large enough to be identified under a dissection scope, were excised and immediately submerged in PBS at pH 7.4 with 4.5g/L D-glucose and placed on ice. The samples were then imaged in fresh buffer within the next several hours. A live/dead viability/cytotoxicity kit for mammalian cells (L-3224 Invitrogen) was used to test the health of tissues undergoing such a pressure by incubating them in buffer with 2 μM calcein-AM or 4 μM Ethidium Homodimer-1 for approximately 15 minutes.

Results and Discussion

The action cross-sections for the various drugs were measured (Figure 4.1) using the automated system described above. As might be expected considering that they were not designed specifically as fluorophores the cross-section values were determined to be relatively dim when compared to commercially available dyes. However, they were still in general, an order of magnitude brighter than the intrinsic fluorophores found in tissue (Zipfel et al., 2003). It should be noted that these measurements were done in solution; the quantum efficiency or indeed the absolute cross-section may be enhanced *in vivo* by binding or insertion into a lipid membrane, and in fact a number of these dyes are known intercalators (doxorubicin, camptothecin, irinotecan). For example, the cross-section of the relatively insoluble drug Ellipticine (Figure 4.1b) changed noticeably which measured in DMSO versus PBS. During the measurement process, the slope of the line defined by taking the log of the power versus the log of the fluorescence counts was calculated. Typically, this was computed to be 2.00±0.05, indicating that the bulk of the fluorescence originated from two-photon absorption. However,

in the case of PPIX, it was equal to 1 below 750 nm rising to between 1.7 and 1.9 from 800 nm upwards. This indicated that a proportion of the fluorescence was derived from linear absorption even at these longer wavelengths, which may mean the values plotted of ppIX (Figure 4.1h) are systematically off, and more importantly, may result in less than optimal image contrast and sectioning ability for multiphoton use (Kantelhardt et al., 2008). This, combined with its low overall cross-section, led to the choice not to pursue PPIX as a contrast agent, although it has been used with good effect to identify cancers in standard fluorescence bronchoscopy (Loning et al., 2004).

After examining the measured the cross-sections, irinotecan (Figure 1e) was identified as a suitable candidate for two-photon cancer drug imaging. It possesses one of the highest cross-sections of the drugs surveyed (albeit unfortunately, lower – by a factor of ten – than the related topotecan (Gryczynski et al., 1999) and solubility in water is high allowing its straightforward injection intravenously and intraperitoneally (Kunimoto et al., 1987). Although typically used for bowel cancer, it has demonstrated effectiveness in the treatment of the metastatic epithelial ovarian cancer (Sugiyama et al., 2002; Bodurka et al., 2003). This disease is extremely deadly due to its lack of detection at early stages, and so we elected to use a murine model we had used previously (Williams et al., 2010) to demonstrate the benefits possible using ACD-based detection. An excitation wavelength of 750 was selected because the action cross-sections appear to drop off quickly above this wavelength and although the drug is slightly brighter towards 700 nm, in general, shorter wavelengths are also more photo-toxic to the tissue.

Figure 4.1 – ACD fluorescence properties: a) the intrinsic fluorescent emission of the various fluorophores; b) Ellipticine in DMSO (brown) and PBS (red); c) 9-Aminoacridine in PBS(red); d) Camptotecan in PBS(red); e) Irinotecan in PBS(red); f) Doxorubicin in PBS(red); g) Dipyridamole in PBS(red); h) protoporphyrin IX in EtOH (green). All solutions in PBS had a pH of 7.4. The normalised linear absorption of the molecule at half the wavelength is plotted in blue for lineshape comparison.

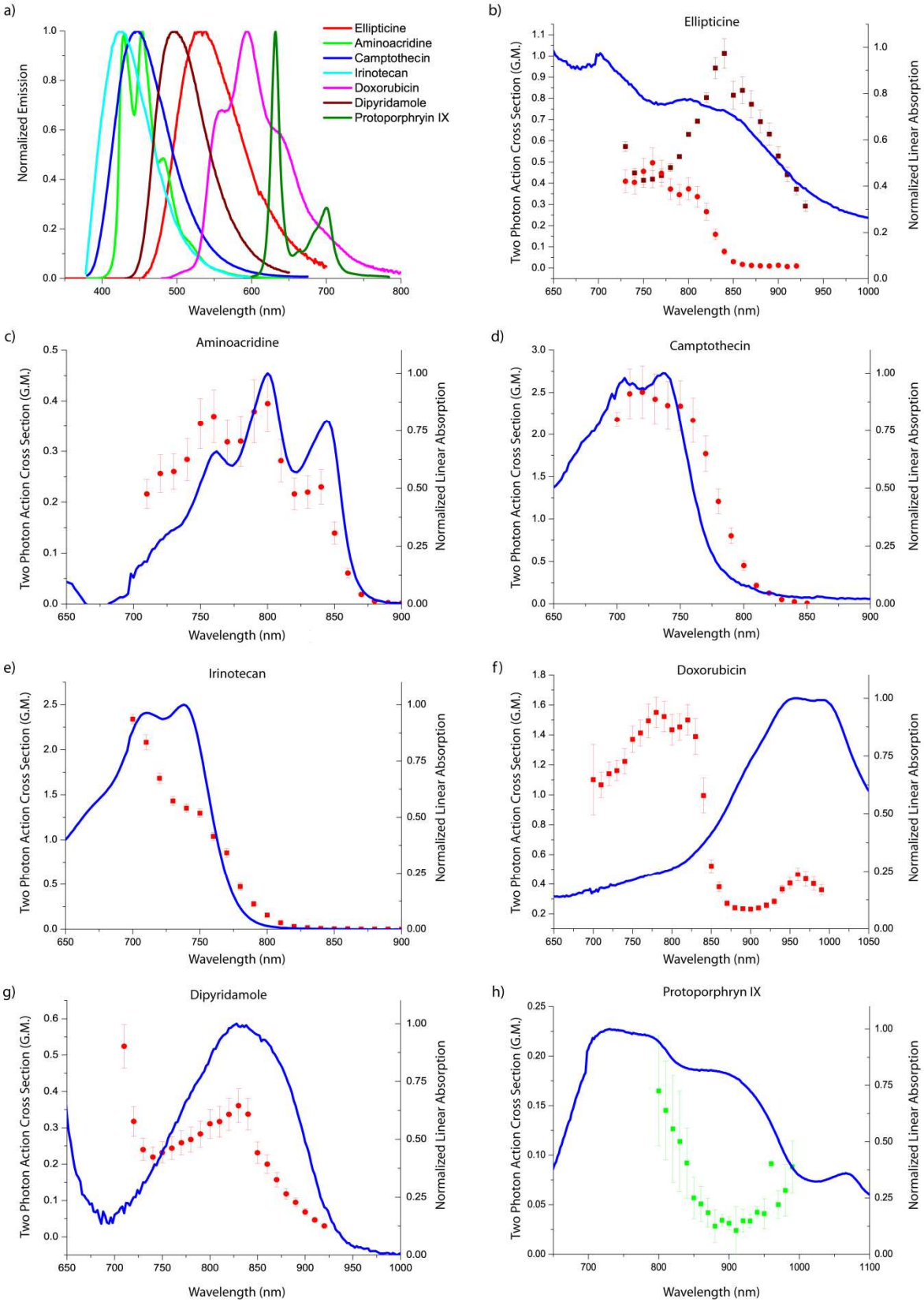
a)
Normalized Emission
Wavelength (nm)
Ellipticine
Aminoacridine
Camptothecin
Irinotecan
Doxorubicin
Dipyridamole
Protoporphryin IX
b)
Ellipticine
Two Photon Action Cross Section (G.M.)
Normalized Linear Absorption
Wavelength (nm)
c)
Aminoacridine
Two Photon Action Cross Section (G.M.)
Normalized Linear Absorption
Wavelength (nm)
d)
Camptothecin
Two Photon Action Cross Section (G.M.)
Normalized Linear Absorption
Wavelength (nm)
e)
Irinotecan
Two Photon Action Cross Section (G.M.)
Normalized Linear Absorption
Wavelength (nm)
f)
Doxorubicin
Two Photon Action Cross Section (G.M.)
Normalized Linear Absorption
Wavelength (nm)
g)
Dipyridamole
Two Photon Action Cross Section (G.M.)
Normalized Linear Absorption
Wavelength (nm)
h)
Protoporphryn IX
Two Photon Action Cross Section (G.M.)
Normalized Linear Absorption
Wavelength (nm)

Tumors and the surrounding tissue from all over the peritoneal cavity were excised for imaging using a two-photon microscope. Although direct in vivo imaging would have been more ideal, in vivo imaging introduces additional complications that will be addressed in further studies after optimal drug candidates are determined. Since the cancerous masses imaged in this study were large enough to be identified under a low magnification dissection scope, with diameters of greater than 100 microns, the wider field of view of a 4x objective was found to be useful for imaging. This objective was known to have an axial resolution on the order of 20 microns (less than expected from the NA of 0.28 due to underfilling of the back aperture), so while its sectioning capability was limited, it could be used to generate large image stacks of 1-2 mm, necessitated by the irregularity of the surface, with steps of 20μm without losing any information. Complementary higher magnification images were also recorded using a 20x objective, though in this case it became difficult to acquire images through the necessary depth of field while maintaining optimal axial resolution.

Tissues imaged in an irinotecan injected mouse (Figure 4.2b,c; 4.3b) were strikingly bright when compared to images taken in control mice (Figure 4.2a;4.3a). Drug fluorescence allowed much lower imaging powers to be used – for the 4x objective this was the difference between using 50-90 mW at the sample compared with between 280-350 mW (for the 20x objective the powers were about a fifth of this for each case). Not only were these lower powers better for phototoxicity, they did not generate the artefacts (visible in Figure 4.3a) created from the scattering of excitation light from lipid molecules in the sample and suspended in the buffer that often plagued the autofluoresence images. The tumors were found to be fairly dense

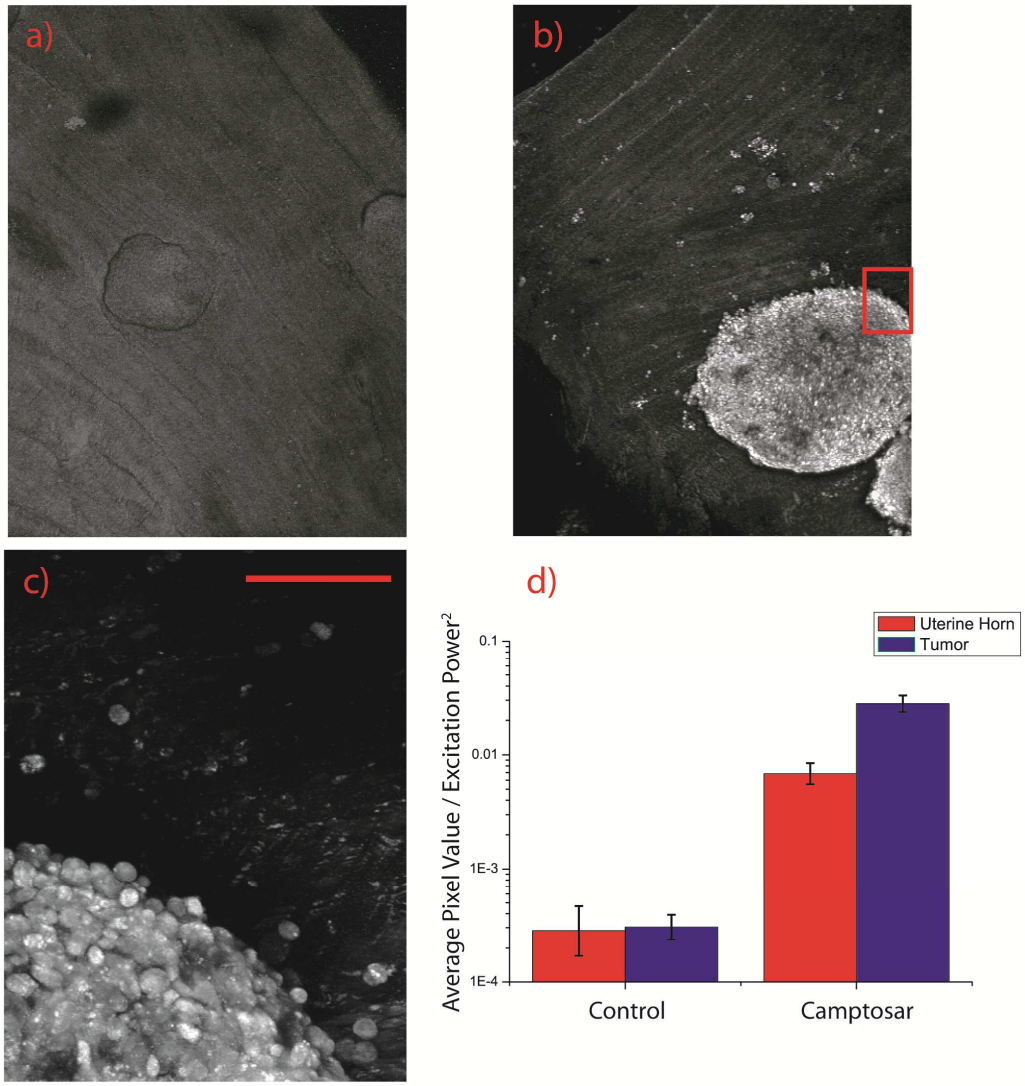

Figure 4.2 – Z projections of tumors on the uterine horn acquired from stacks of images taken with the Olympus 4x objective on a control mouse a) and Camptosar injected mouse b). An Olympus 20x objective was used c) to acquire a higher magnification image of the highlighted region of the irinotecan mouse. The control image has been brightened for better contrast and was taken at 5.5 times the excitation power of b). An analysis of tumors d) on the uterine horn found a general enhancement in fluorescence from irinotecan injection with the drug preferentially staining the tumors over the tissue by a factor of ≈4. (Scale bar represents 500 μm for images a and b 100 μm for c))

scatterers limiting maximal imaging depth into the tumor mass using the 20x objective to between ~100 μm.

In order to better quantify the magnitude and nature of the drug fluorescence for so varied a disease, tumors were identified on two separate locations: the uterine horn (Figure 4.2) and the intestinal peritoneum along the length of the bowel (Figure 4.3). The two-dimensional images for analysis were created from the three dimensional stacks by creating projections of the maximal value for each pixel. In some cases the tissue moved during the course of scanning, but as long as this displacement was slight enough to create only minimal blurring the images were used in the analysis. Though the instrumentation was kept constant throughout the trial, the laser power was varied in order to prevent pixel saturation in any of the images. Therefore "brightness" was taken to be the average pixel value of the tissue in the projection normalised by the square of the excitation power used to acquire it. Overall, eight mice were analyzed with tumors on the uterine horn (2-control, 6-Camptosar with a total of 5 and 15 tumors respectively – Figure 4.2d) and nine with tumors along the bowel (4 Control - 5 Campto, 9 tumors total – Figure 4.2e). Tissue fluorescence increased greatly in both samples with the addition of irinotecan by over an order of magnitude, however perhaps more interestingly, this increase in fluoresence favoured the tumor over the background tissue preferentially so that the change in tumor fluorescence was higher than the change in the surrounding tissue fluorescence by roughly a factor of four (3.8x in the case of the uterous and 4.2x for the intestines ($p < 0.05$)). However, because the intestinal autofluorescence was about twice as bright as that from the tumor, the resulting contrast between tumor and tissue was only a factor of two,

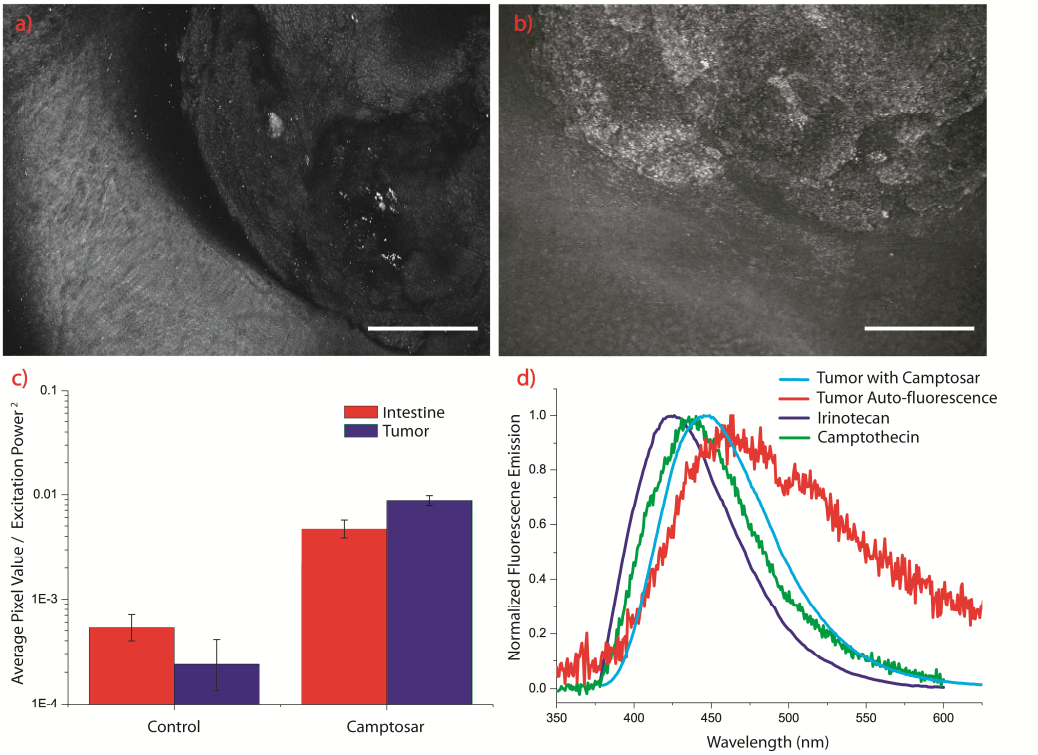

Figure 4.3 – Imaging of tumors on the mouse intestinal tract in a control a) and Camptosar injected mouse b). Analysis revealed an enhancement of fluorescence in the Camptosar injected animals and a preference in the tumors of about 4 times. However, in this case the intestinal auto-fluorescence was initially roughly twice as bright as the tumor, so the total discrimination was roughly a factor of two. Emission spectra d)were recorded from tumors with and without Camptosar injection and from irinotecan in PBS in a fluorimeter, demonstrating the presence of irinotecan in the tumor tissue. (Scale bar 500 μm for images a and b)

mice were measured (Figure 4.3d). The spectra was observed to shift slightly rather than in the case of the uterine horn where this factor of four held. Interestingly, this preferential uptake did not occur when excised tissue from a control mouse was incubated for twenty minutes in 50μM irinotecan.

In order to confirm that it was irinotecan we were measuring, the two-photon fluorescence spectra of tumors from the Camptosar and control from that measured by single photon fluorescence in a fluorometer, so that it lay closer to that of camptothecin. Although, irinotecan is known to gain its cytotoxic effect by hydrolysis into the much more potent lipophylic SN-38 (Toffoli et al., 2003), this occurs over much longer time scales, so it is unlikely that a bi-product of irinotecan was being observed. Instead, it is probable that this slight shift stemmed from the environmental effects mentioned previously. The spectrum does lie close enough to the fluorometric emission curve to suggest that irinotecan was the predominant cause of the fluorescence in the images.

Finally, the viability of the excised tissue from both the control and drug injected animals during imaging was tested by utilising a Live/Dead assay. Tissue/Tumors from irinotecan injected mice were co-stained with calcein-AM, which has been shown to label live tissue. The samples then became fluorescent in the green channel, with good overlap between the blue and green channels, (though the calcein absorption was more uniform across all the tissue - data not shown). The apoptosis indicator ethidium homodimer-1, provided scant staining of the tissue, thus confirming that the tissue was in general still healthy, as well as suggesting that the drug had not yet had a substantial impact on the tumor cell vitality.

Conclusions

This work has elucidated fundamental photophysical properties of fluorescent ADC's relevant to multiphoton cancer visualization. The capability for utilizing the fluorescent drugs as multiphoton contrast agents has demonstrated in tissue using reasonable intermediate doses. Especially of interest is the demonstrated nature of the drug to preferentially target tumors, which may add to its usefulness as a contrast agent for optical biopsy in vivo. Much remains to be explored in order for this technique to be found truly useful to the clinician, including the study of the image quality when administered intravenously and at various time points after injection or during a course or treatment. Like any model system, its relevancy to human cancers needs also to be examined. However, these images demonstrate the ability of ACDs to provide immediate and cellularly resolved multiphoton images, with promise of one day becoming a complementary diagnostic technique to the clinical oncologist.

Acknowlegements

Alex Nikitin's lab donated the OSN3 cells, and Andrea Fleshkin-Nikitin provided help advice pertaining to this cell line. Pam Gordiner performed the tedious task of cell passaging and prepared the OSN3 cells for injection. Sylvia Allen and the rest of her crew in the CARE animal facility kept the mice healthy and happy as long as possible. Dr. Wendy Williams was a useful source of information

REFERENCES

Aaron JJ and Trajkovska S, "Fluorescence Studies of Anti-Cancer Drugs - Analytical and Biomedical Applications". Current Drug Targets, **7** 1067-1081 (2006)

Allegrini G, Goulette FA, Darnowski JA, Calabresi P, "Thrombospondin-1 plus irinotecan: a novel antiangiogenic chemotherapeutic combination that inhibits the growth of advanced human colon tumor xenografts in mice" Cancer Chemother Pharmacol **53**: 261–266 (2004)

Bodurka DC, Levenback C, Wolf JK, Gano J, Wharton JT, Kavanagh JK, and Gershenson DM, "Phase II Trial of Irinotecan in Patients With Metastatic Epithelial Ovarian Cancer or Peritoneal Cancer" *J Clin Oncol 21:291-297.* (2003)

Becker, V, Vercauteren T, von Weyern CH, Prinz C, Schmid RM, and Meining A, "High Resolution Miniprobe-based Confocal Microscopy in Combination with Video-mosaicing." Gastrointestinal Endoscopy", **66** 1001–1007 (2007)

Denk W, Strickler J, Webb WW,"Two-photon laser scanning fluorescence microscopy". Science **248** 73–6 (1990)

Fu L, Gan X, and Gu M, "Nonlinear optical microscopy based on double-clad photonic crystal fibres," Opt. Express **13** 5528-5534 (2005).

Göbel W, Kerr JND, Nimmerjahn A, and Helmchen F, "Miniaturized two-photon microscope based on a flexible coherent fibre bundle and a gradient-index lens objective," Opt. Lett. **29** 2521-2523 (2004)

Gryczynski I,Gryczynski Z, Lakowicz JR, Yang D, Burke TG "Fluorescence Spectral Properties of the Anticancer Drug Topotecan by Steady-State

and Frequency Domain Fluorometry with One-Photon and MultiPhoton Excitation" Photochemistry and Photobiology, **69** 421-428 (1999)

Helmchen F, Fee MS, Tank DW, and Denk W, "A miniature head-mounted two-photon microscope: High-resolution brain imaging in freely moving animals," Neuron **31** 903-912 (2001)

Kantelhardt SR, Diddens H, Leppert J, Rohde B, Huttmann G, Giese A, "Multiphoton Excitation Fluorescence Microscopy of 5-Aminolevulinic Acid Induced Fluorescence in Experimental Gliomas" Lasers in Surgery and Medicine **40** 273-281 (2008)

Kiesslich R, Burg J, Vieth M, Gnaendiger J, Enders M, Delaney P, Polglase A, McLaren W, Janell D, Thomas S, Nafe B, Galle PR, Neurath MF. "Confocal laser endoscopy for diagnosing intraepithelial neoplasias and colorectal cancer in vivo," Gastroenterology," **127** 706-713 (2004)

Kunimoto T, Nitta K, Tanaka T, Uehara N, Baba H, Takeuchi M, Yokokura T, Sawada S, Miyasaka T, Mutai M "Antitumor activity of 7-ethyl-10-[4-(1-piperidino)-l-piperidino]-lcarbonyloxy-camptothecin, a novel water soluble derivative of camptothecin, against murine tumors." Cancer Res **47** 5944-5947 (1987)

Loning M, Diddens H, Kupker W, Diedrich K, Huttmann G, "Laparoscopic fluorescence detection of ovarian carcinoma metastases using 5-aminolevulinic acid-induced protoporphyrin IX." Cancer **100** 1650–1656 (2004)

Myaing MT, MacDonald DJ, and Li XD, "Fiber-optic scanning two-photon fluorescence endoscope," Opt. Lett. 31, 1076-1078 (2006).

Ouzounov DG, Moll KD, Foster MA, Zipfel WR, Webb WW, and Gaeta AL, "Delivery of nanojoule femtosecond pulses through large-core microstructured fibers," Opt. Lett. 27, 1513-1515 (2002)

Sugiyama T, Yakushiji M, Kamura T, Ikeda M, Umesaki N, Hasegawa K, Ishikawa M, Saji F, Hiura M, Takahashi T, Sato S, Ochiai K, Kikkawa F, Takeuchi S, Ohashi Y, Noda K, "Irinotecan and Cisplatin as First-Line Chemotherapy for Advanced Ovarian Cancer" Oncology **63** 16-22 (2002)

Toffoli G, Cecchin E, Corona G and Boiocchi M "Pharmacogenetics of Irinotecan" *Curr. Med. Chem. - Anti-Cancer Agents,* ***225,*** 225-237 (2003)

Williams RB, Flesken-Nikitin A, Ellenson LH, Connolly DC, Hamilton TC, Nikitin AY, and Zipfel WR, "Strategies for high resolution imaging of epithelial ovarian cancer by laparoscopic nonlinear microscopy" Under Review

Xu C, and Webb WW, "Measurement of two-photon excitation cross sections of molecular fluorophores with data from 690 to 1050 nm" J. Opt. Soc. Am. *B*, **13** 481 (1996)

Zipfel WR, Williams RM, Christie R, Nikitin A, Hyman BT, & Webb WW, "Live tissue intrinsic emission microscopy using multiphoton excited native fluorescence and second harmonic generation," PNAS, **100,** 7075-7080 (2003)

Zipfel WR, Williams RM, & Webb WW, "Nonlinear magic: multiphoton microscopy in the biosciences," Nat Biotech. **11,** 1369-77 (2003)

Chapter 5 – Preliminary Studies in the Application of Fluorescent Microscopy to the Detection of Tuberculosis

Abstract

A multi-institutional collaboration has been established to attempt to build a primate tuberculosis model suitable for the development of a new generation of anti-tuberculosis drugs. As part of this consortium, a fibre bundle based fluorescence bronchoscope was constructed that will be used to examine the stress-reporting fluorescence from engineered mycobacteria *in vivo*. This bronchoscope has been demonstrated to be capable of imaging and switching the fluorescent protein Dronpa, which will hopefully allow the background auto-fluorescence from the lung tissue to be subtracted from the images. Additionally, as a potential means of detecting the wild type bacteria *in vivo*, the fluorescence lifetime of the related bacteria *m. smegmatis* has been measured and demonstrated to be significantly different from that of the intrinsic fluorescence of the background lung tissue. This could allow for its use in the discrimination in sputum smears and within the pulmonary tract, and therefore as a technique to diagnose tuberculosis in humans.

Introduction

In the western world, it is hard not to think of tuberculosis as a disease of a bygone age, the feller of such immortal names as Keats, Chekov, Chopin, Lawrence, and Orwell... In fact the very length of this list hints at the impact of the disease on general life before the advent of antibiotics and one is reminded of the sanatoriums that were once spread throughout the landscape of North America. However, a disease which, as the fossil record demonstrates, has been plaguing humans for at least half a million years, is hard to eradicate, especially when combined with the general poverty typical

of life outside the developed world; today *Mycobacterium tuberculosis* (Mtb) continues to infect an astonishing one third of all humans (Barry and Cheung, 2009). Most of these cases however are in a latent form, the invasive bacteria being successfully sequestered by the body's immune system into granulomas. In only 5 to 10 percent of all infected individuals will the disease develop into a more aggressive active form, but this is enough to make Mtb the second deadliest infectious killer in the world (next to HIV/AIDS) with 1.7 million deaths per annum (Russell, 2007). That more than 90% of these deaths occur in the developing world can be directly attributed to the cost and the lengthy duration of the Mtb treatment. The World Health Organisation currently recommends that new infectious cases of pulmonary Mtb are treated with an intensive combination of four anti tuberculosis drugs for two months in duration, followed by continued treatment of at least two drugs for an additional four to six months (WHO, 2003). This mix generally contains the bactericidal drugs isoniazid, the sterilizer rifampicin, ethambutol which mitigates resistance, and pyrzinamide which operates in acidic conditions or streptomycin which inhibits rapidly multiplying populations. As costly as that may seem, things get even worse for patients with a weakened immune system due to co-infection with HIV/AIDS and it should be noted that there is a strong geographic overlap between the diseases. Furthermore, re-infected or drug resistant patients require a new, more diverse medical cocktail, with treatment lasting for at least 18 months and increasing the cost of treatment by 1400 fold (Barry and Cheung, 2009). Incidents of resistant strains of the disease are growing rapidly - with cases now appearing that are resistant to all of the first-line

antibiotics. For these reasons the development of new antituberculosis drugs is critical to controlling the worldwide Mtb pandemic.

Since tuberculosis has long been considered effectively eliminated in the wealthier nations, it has become a relatively understudied disease given its current global impact. For example, all of the aforementioned "First Line" drugs were developed before 1970. Questions as fundamental as how the virulent form emerges from the latent disease still remain, with recent extremely controversial findings (Ghosh et al., 2009) going as far as to suggest spore formation as the vehicle for this transition. Thus, research into new drug development must be conducted in parallel with attempts to elucidate the basic natural history of infection. To that end we have been part of a large scale international collaboration funded by the Bill and Melinda Gates foundation, in order to develop both suitable model systems for tuberculosis, as well as techniques for studying them. Unfortunately, unlike other diseases, mice do not develop the full blown granulomas that are the distinguishing characteristics of the human infection (Russell, 2007). In the human lung, for example, an "invading" bacterium (and a single bacterium is likely the infectious dose (Russell, 2007)) is phagocytosed by alveolar macrophages, which then recruit other mononuclear cells. Eventually, a mass – the granuloma or tubercle from which the disease derives its name – develops consisting of a core containing the infected macrophages, foamy macrophages, and other immune cells. This is surrounded by a shell of lymphocytes and a fibrous cuff composed of collagen and other extracellular matrix components. Typically this is the extent of the disease, but in the active patient, the granuloma has at its center a necrotic core of caseating tissue (so named due to its cheese like

appearance) from which spill thousands of free mycobacteria which in turn infect both other regions of the body as well as other individuals. Not all granulomas are alike. In fact, a spectrum of tubercular lesions have been found even within the same individual including variation of both the composition of mononuclear cells within the granuloma (Lin et al., 2009) as well as the local microenvironment (Via et al., 2008). These differences contribute to drug uptake and efficacy and therefore the characterization of the local profile of the disease is crucial to drug development. Fluorescence microscopists have amassed a variety of tools for assessing such parameters as oxygen tension, pH, calcium concentration etc., but the use of these stains in the granuloma is not trivial, especially in live animals. Like other mycobacterium, Mtb is an acid-fast organism, and thus readily resists standard staining methods. The auramine-rhodamine stain may be used to fluorescently label bacteria, but its rather intensive protocol includes fixation, and therefore incompatible with *in vivo* studies. We are involved in two attempts to use fluorescence to visualise the bacterium and its surrounding tissue: The first involves the development of transgenic strains of Mtb which report their local environment by up regulation of genes encoding fluorescent proteins. The second attempts to visualise and identify the bacteria by the nature of their own intrinsic fluorescence.

Visualisation of Fluorescent Reporting M. tuberculosis Strains Using A Custom Designed Fluorescent Bronchoscope

Regardless of their size, creatures adapt to the sudden stresses placed on them by their environment for the maintenance of their vitality. In the case of single celled organisms, gene transcription can rapidly evolve as the

molecular pathways used to stabilize the cell are invoked. By examining and selecting genes that are up regulated in response to specific stresses, our collaborators in the Russell lab at the Cornell's College of Veterinary Medicine are creating strains of tuberculosis that can serve as reporters to such varied stresses as drug toxicity, hypoxia, and external pH. These genetically modified bacteria will then be used to infect Macaque monkeys. By endoscopically monitoring the granuloma fluorescence over duration of the drug course, we hope to gain vital information regarding the varying response of the disease to the treatment.

There are two main challenges involved in the fluorescence bronchoscopy of tuberculosis - delivering the tip of the bronchoscope to tubercular region and then imaging the desired reporters amid the large background auto-fluorescence present in the lung. The solution to the former problem will hopefully come from technology already commercially available. The company Traxtal is able to guide a catheter through the labyrinthine bronchial tree using an electromagnetic probe co-registered via external fiducials with a pulmonary computer tomography (CT) scan. This should allow the delivery of the distal tip of the catheter to an intended position with 1mm accuracy. Regions of interest identified by collaborators using positron emission tomography (PET) markers such as fludeoxyglucose (FDG) and as well as novel probes such as a trehalose derivative developed as a part of this grant, may be then examined via bronchoscopy.

The large amount of auto-fluorescence in the lung poses a serious problem to the quantification of signal from bacterial reporters due to its relative strength and breadth across the visible spectrum (Hüttenberger et al., 2008). This signal stems from such endogenous fluorophores as elastin

(Deyl et al., 1980) which is abundant in the lung and may also derive from macrophage cells which have been shown to intensely auto-fluoresce (Njoroge et al., 2001) although the nature of that fluorescence is still unknown. As one possible means of getting around this auto-fluorescence we have considered using the fluorophore Dronpa. This genetically engineered GFP variant is photo-switchable. Like GFP, Dronpa fluoresces when exposed to 490 nm light during which time it bleaches away into an off state. It can then be reactivated with a burst of 400 nm light. By cycling between pulses of 400 and 490 nm one can create an image in which the signal fluctuates against a constant background. This method of optical lock-in detection (OLID) has been demonstrated (Marriott et al., 2009) to recover features that previously would have been swamped out by background. However, OLID requires a rather lengthy time series be taken and then in order to quantify the relative amount of switchable fluorophore at each pixel a time series must be analysed by the following correlation algorithm:

$$\rho(x,y) = \sum_t \frac{\{I(x,y,t)-\mu_I\}\{R(t)-\mu_R\}}{\sigma_I \sigma_R} \qquad 1)$$

Where I(x,y,t) is the pixel intensity at a given time, R(t) the value of a reference Dronpa sample at that time, μ_I, σ_I and μ_R,σ_R are the mean and standard deviation values of the pixel intensity and the reference respectively. It should be noted that while optimal results are achieved by using an external reference or beads in the media coated with Dronpa, regions in the image suspected of containing high fluorescent protein content may also be used. We acquired samples of *Drosophila* salivary gland containing Dronpa tagged histones, to evaluate this scheme. A time series

(figure 5.1a) was acquired during which the sample was repeatedly imaged for 10 seconds at 490nm and then activated with 400 nm in bursts of 250 ms. Images following the activation pulse (figure 5.1c) were noticeably brighter than immediately preceding it (figure 5.1b). Of relevance to the project was that the rescaled result obtained by subtraction of the pre from the post–activation images (figure 5.2d) was not noticeably difference from one obtained using the above algorithm (figure 5.1e). This suggests the possibility of neglecting the acquisition of such a long time series of data which would be difficult in the lung of a breathing animal. Instead, one could bleach the surrounding tissue for an extended period of time and then: acquire an image, activate, and acquire a second image in less than half a second. The feasibility of this scheme is enhanced both by fact that the respiration of the animal will already be gated for the CT imaging required to place the bronchoscope, as well as relaxed constraints on the quantification of the signal due to the essentially binary nature of the reported stress (ie the bacteria report either low or neutral pH, but not graduations in between).

There were a number of parameters to consider in the design of the bronchoscope. First of all, the physicians specified that the outer diameter be no more than 800 microns. This was deemed too narrow for a scanning system and so an imaging fibre bundle was selected to relay the image to an external CCD. There are three manufacturers of coherent fibre bundles we have tested: a 10,000 core leached fibre bundle from Schott, a 30,000 core fibre bundle from Sumitomo (IGN-08/30), and a 30,000 core fibre bundle from Fujikura (FIGH-30-650s). All the bundles had a maximum outer diameter of 0.8mm, including the outer jacket. Although it

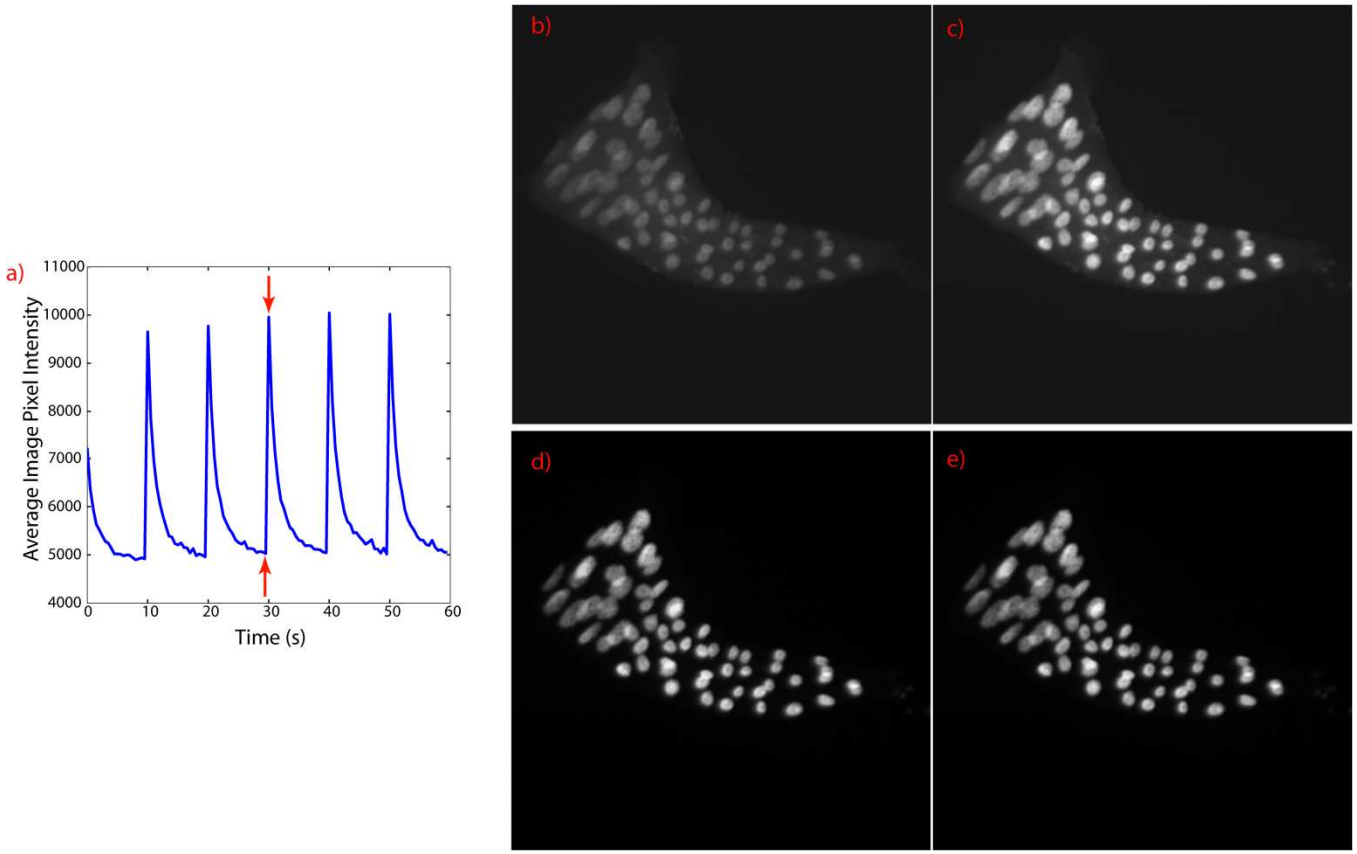

Figure 5.1 – An examination of background subtraction using Dronpa tagged histones in the *Drosophila* salivary gland: a) A time series of during which the image was read with 490nm light followed by reactivation every 10s with a short burst at 400nm; b) an example of the image brightness at the bleached point indicated in a); c) the reactivated image; d) the result of the subtraction of these bright and dim images; e) the result of the OLID correlation method.

benefits the signal-to-noise ratio to use separate fibres for illumination, we chose the simpler route of epi-collection with the excitation and emission pathways separated by a dichroic filter in the usual manner (figure 5.2-3). In this scenario auto-fluorescent of the fibre can become a problem. A characterization of these fibre bundles (Udovich et al., 2008) has demonstrated that while all of these bundles fluoresce, the Sumitomo bundle appears to do so the least and most of that lies in the blue portion of the spectrum.

When purchasing the Fujikura bundle, the vendor (Myriad Fiber Imaging Tech.) provided and mounted an aspheric doublet on the distal tip which was contained in a stainless steel sheath 3mm long and 0.8mm in diameter. This lens system produced a field of view of 70º for objects greater than 5mm away. The other fibre bundles however lacked any distal optics. Many systems of this size use gradient index lenses to provide magnification, however these appear to suffer from spherical aberration which reduces resolution (Jung and Schnitzer, 2003). A bare bundle itself provides some inherent resolution, for example, the Sumitomo bundle possesses hexagonally packed cores of a diameter equal to 2.4μm spaced 4μm apart from each other and so, from sampling theory, should be able to provide lateral resolution on the order of 8μm. There is also an intrinsic sectioning ability of the fibre as both the intensity of the excitation light and the detection probability of the fluorescence being coupled back into an individual core falls off rapidly away from the face of the fibre (Balaji et al., 2003) giving an axial resolution on the order of 10 microns. It is therefore possible that the distal end optics may be neglected entirely.

In order to help quantify the signal, the vector for an additional fluorescent protein – mCherry – was inserted downstream of a constitutive promoter, the transcription rate of which was demonstrated to be independent of the bacterial environment. This creates a source of constant fluorescence that can then be ratioed against that from the reporter. In order to image both the green emission of Dronpa and the red of mCherry we have added an Optosplit II (Cairn Research, figure 5.2-4) which allows for the image to be split into two frames on the same CCD. Since sensor size of the purchased Luca EMCCD (Andor Technology, figure 5.2-5) is 1024x1024 pixels, it is able to acquire two 512x512 images on the same camera. The Luca has the added benefit of allowing the image transfer over USB rather than the typical PCI card, thus allowing the system to be run on a laptop.

The process of exciting both the chromophores, and the reactivation of bleached Dronpa molecules necessitates the use of three excitation bands at 400, 490, and 575nm. Switching between separate laser systems is both expensive and challenging to align. Instead we have selected a "light engine" (Lumencor) a system composed of diode pumped fluorescent rods which produce over 200mW at each wavelength with a relatively narrow (20nm) bandwidth. The device is switchable at up to 1kHz and can be fully automated. Initially our system used a single liquid light guide (Newport) to deliver the light from the unit, to collimating optics, and then to an objective where it was launched into the bundle. However we found that this autofluoresced at these high illumination powers and coupling into the fibre bundle was poor owing to an étendue mismatch between the two (the light

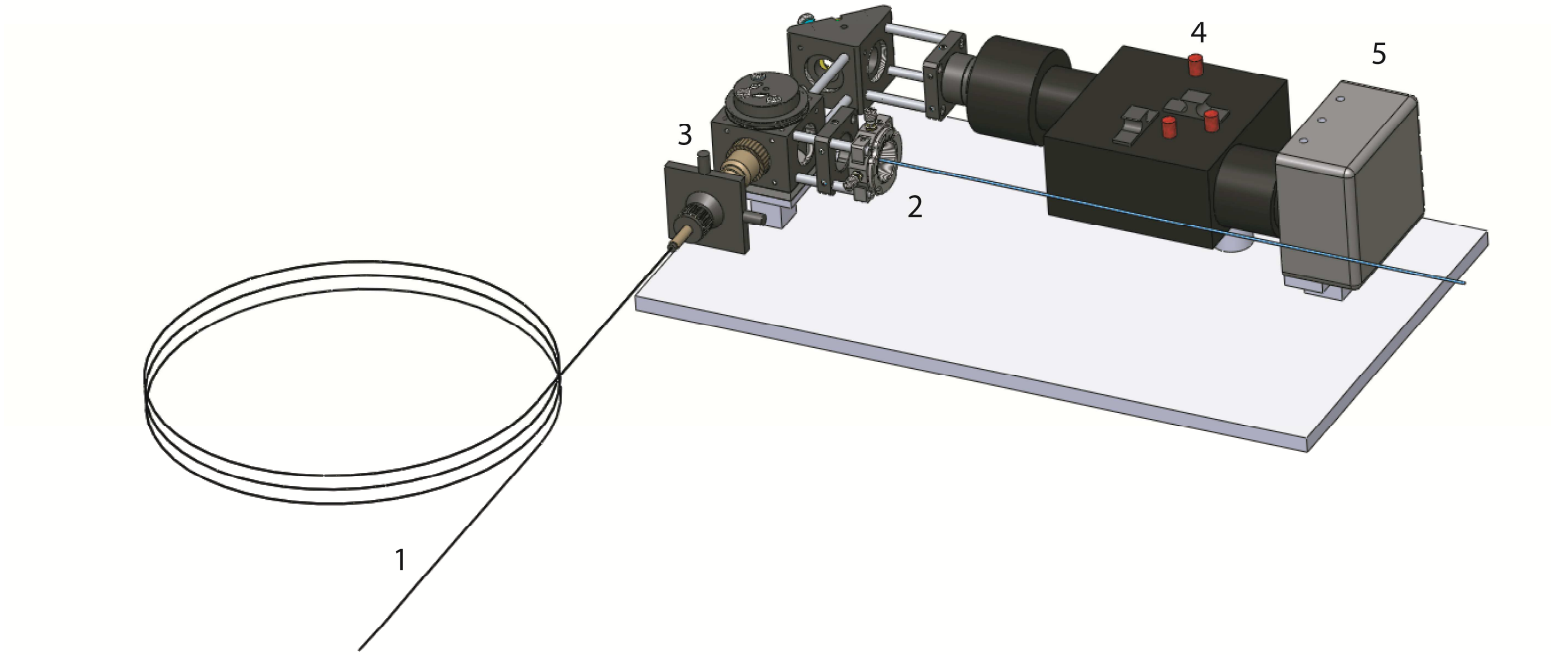

Figure 5.2 – A CAD mock up of the bronchoscope showing its primary components: 1) the Sumitomo imaging fibre bundle; 2) the illumination fibre from the Lumencor light engine; 3)the fibre mount and aspheric objective; 4) the Optosplit II image divider; and 5) the Luca EMCCD.

guide has a much higher NA of 0.65 compared to 0.35). As a result we elected to use a silica fibre optic cable to deliver the illumination light (figure 5.2-2). While awaiting the completion of the reporter strains from the Russell lab, we again returned to the Dronpa-tagged histones of the *Drosopholia* salivary gland. Using the Schott fibre bundle we were able to acquire images (figure 5.3a-c) similar to those seen above. This supports the feasibility of using the image subtraction scheme through a fibre bundle, especially the capability of our system to deliver enough UV light to photo-activate the fluorescent protein. This leached bundle, however, was deemed too flexible by the physicians to be inserted down a catheter and dismissed for the Fujikura and Sumitomo fibres. In an attempt to gain some practical experience with the bronchoscope, the system was transported to the NIH where it was used with the Traxtal system to image an adult boar. The pig was anesthetised, intubated, and placed on its back on a CT bed where a tomographic reconstruction of the bronchial pathway was taken. The physician then guided a catheter using the Traxtal navigation software to a selected region of the lung. At that point the probe was removed from the catheter and the bronchoscope fibre inserted. The Fujikura bundle was then used – in combination with light from an additionally inserted commercial scope - to image the bronchiole (figure 5.3e). Although this system was capable of generating acceptable images with significant fields of view when imaging reflected light (figure 5.3d), the numerical aperture of the lens must be quite low, for it was found to be insufficient at collecting fluoresced light. The bare Sumitomo fibre, however, proved itself capable of acquiring bright fluorescence images, but only for samples pressed directly against the distal

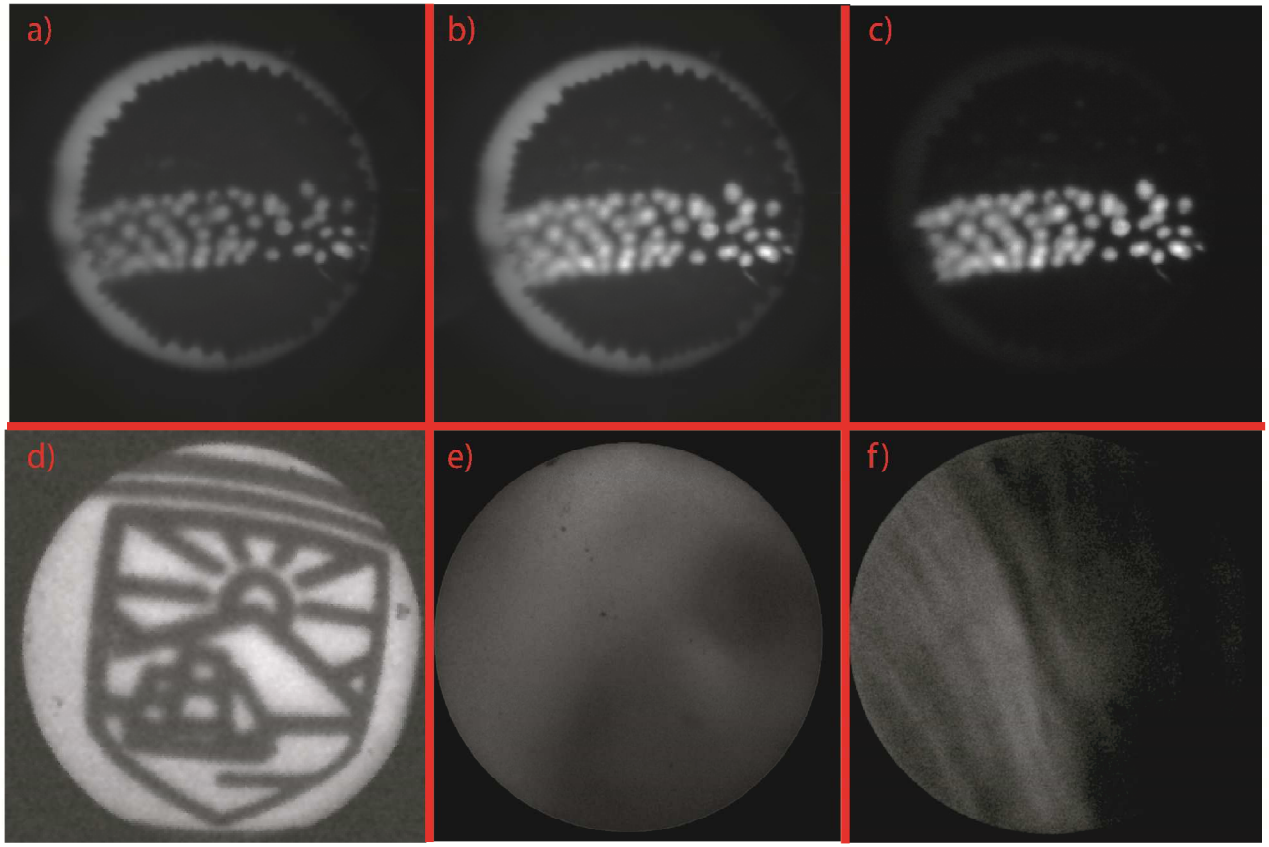

Figure 5.3 a-c) Dronpa tagged histones in the *Drosophila* salivary gland imaged through a Schott Fiber Bundle: bleached a); after reactivation with UV light b); and the background subtracted image c). The Cornell logo (width ≈2 cm) d) demonstrates the imaging capability of the Fujikura fibre with the aspheric doublet. The same system was also used in an anesthetised pig to acquire a white light image e) of the porcine bronchial tract. A fluorescent image f)of endogenous fluorescence in the same airway was taken at 490nm excitation through a bare Sumitomo bundle.

tip. When it was inserted into the same catheter and the tip directed against the channel wall, bright auto-fluorescence was recorded (figure 5.3e). It is likely that this will prove the most functional setup, as the granulomas possess a cheese-like consistency and a bare fibre inserted into a granuloma punctured by a needle-tipped catheter may result in the most useful images. In other words, even a high numerical aperture lens system may prove useless unless it has a negligible working distance.

It is inevitable that the design of the system will evolve over the course of the study. The current setup has been constructed to be as adaptable as possible, for example, it can easily incorporate a narrower fibre bundle which will gain increased flexibility at the cost of poorer resolution (a sacrifice which may be reasonable). Additionally, more excitation channels can be added to the light source without too much trouble should different chromophores be selected in the future. Although the bronchoscope has been designed anticipating its main requirements, only experience will demonstrate the necessary optimizations required for full utility, experience which will be gained once the systems infected with fluorescent bacteria become available for study.

Identifying the Fluorescent Mycobacteria by the Lifetime of Their Autofluorescence

While these fluorescent reporting tuberculosis strains will potentially prove extremely helpful in the design of new anti-tuberculosis agents, one is unlikely to encounter theme outside of a BSL3 laboratory. Typically, the underfunded clinicians in the developing world are forced to identify pulmonary tuberculosis using standard transmission microscopy and Ziehl-

Neelsen (ZN) staining of sputum smears. A literature review reveals that fluorescent examination by auramine-staining increases sensitivity by 10% over this method (Steingardt et al., 2007) while maintaining the same specificity. This is extremely import, as it is estimated that a diagnostic test with a sensitivity improved to greater than 85% to sputum smear-positive and smear-negative samples and a specificity of 97% could prevent 400,000 deaths annually, relative to the current values for the sensitivity and specificity which are approximately 53% and 97% in the Mtb clinics (and these serve only ~50% of the infected population) (Keeler et al., 2006). Thus there is a great need for new diagnostic tests to identify the ill.

It is well known that organic matter contains endogenous fluorophores, which vary in both their spectrum and strength from species to species and organ to organ. The main fluorescent component in mycobacteria, is the aptly named coenzyme F_{420}, which was identified originally (Cheeseman et al., 1972) as the source of the strong absorption peak found in *Methanobacterium* at 420nm. This hydride carrier is found mainly in methanogenic Archaea, but is also present in mycobacteria, which, when excited at 420nm, glow a bright cyan with maximal emission at 475nm. The use of this fluorescence as a marker for indentifying M. tuberculosis has been applied to sputum smears with some success (Patiño et al., 2008), especially when the samples were heat inactivated by incubation for 20min at 80°C, which was demonstrated to raise the fluorescence by a factor of 10. It is possible that this serves to convert the reduced $F_{420}H_2$ (which is non-fluorescent) into its oxidised form. This method however, suffers from the fact that lung tissue itself brightly auto-fluorescent. Rather than spectroscopically trying to unmix the mycobacteria emission from that of

surrounding tissue, we wondered if fluorescent lifetime analysis might be useful in disentangling the two signals. Coenzyme F_{420} is a deazaflavin derivative and like other flavins has a lifetime on the order of 4 ns. This is substantially longer than other intrinsic fluorophores like NADH and Elastin which typically have lifetimes under 2ns depending on their oxidation state and local environment (Elson et al., 2006).

In order to assess the feasibility of fluorescence lifetime imaging (FLIM) as a means of isolating the bacteria *in vivo*, we used a system built around a SPC-830 (Becker & Hickl) TCSPC card (figure 5.4) which was synced to a confocal scanbox (MRC 600 Biorad) to allow for image acquisition. The lifetime measurements were acquired both by two photon as well as single photon excitation. In order to acquire the latter, the beam from a Ti::Sapphire laser (Maitai, Spectra Physics) was doubled by placing a BBO crystal at the center of a unity telescope (figure 5.4 dashed box). Before entering the scanbox, the IR light was removed by a band pass filter, and the remaining 420nm beam was passed through ~10cm of glass dispersing it and therefore limiting the probability of any two-photon absorption in the deep UV. In addition to the usual Pockels Cell (Con Optics) to regulate the intensity of the beam, a pulse picker (Con Optics) was used to increase the spacing between the pulses depending on the lifetime of the system and the total number of photons collected. A microchannel plate PMT (Hamamatsu R3809U-50) behind a 480/40 bandpass filter (manufacturer unknown) was used for optimal detection. The resulting exponential curves were fit using the sum of exponentials:

$$y(t) = \sum_i^{\infty} \alpha_i \, e^{-\frac{t}{\tau_i}} \qquad 2)$$

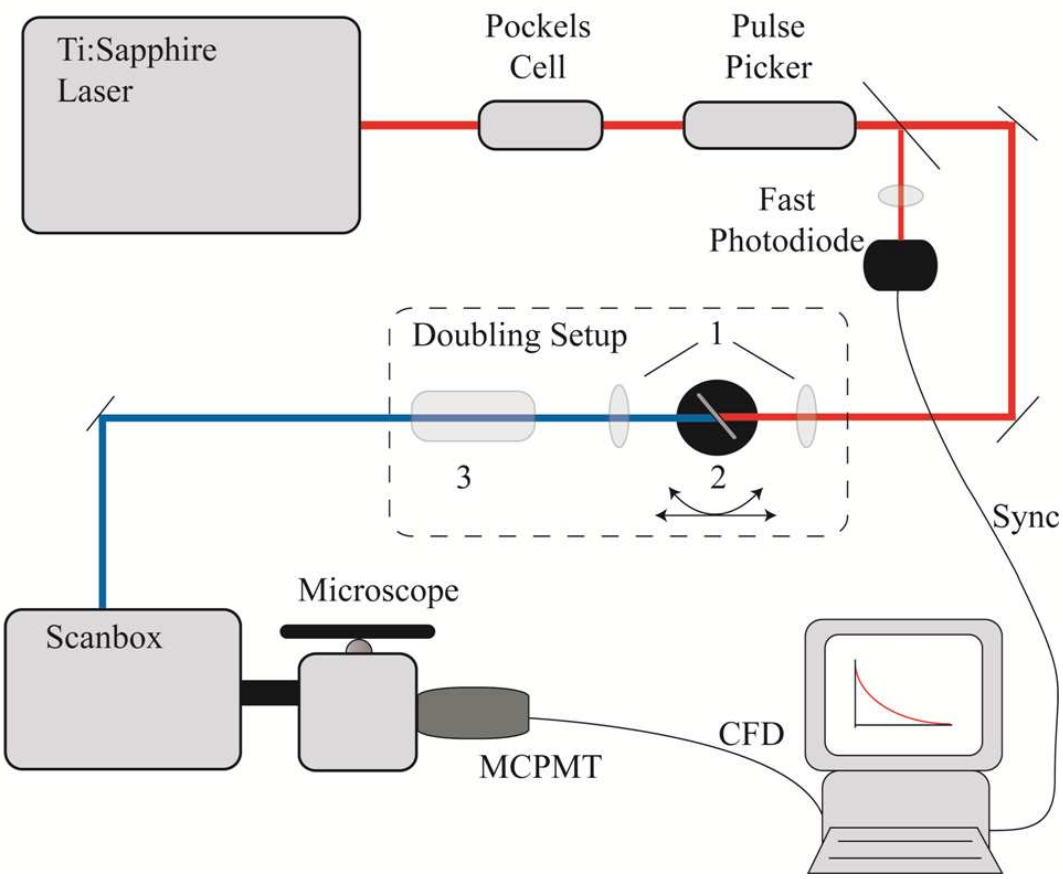

Figure 5.4 The experimental apparatus used for fluorescent lifetime imaging both of two photon excited and standard fluorescence, the latter necessitating a doubling setup that included: 1) focusing optics, 2) a BBO crystal mounted on a three axis stage, and 3) a dispersive glass to stretch the doubled pulses.

convolved with the instrument response function, where α_i and τ_i are the amplitude and decay constant of each fluorescent component i. While each component has its own lifetime, the average lifetime of a curve (Lakowicz, 2006) could be calculated as:

$$\langle \tau \rangle = \frac{\sum_i \alpha_i \tau_i^2}{\sum_i \alpha_i \tau_i} \quad 3)$$

which often proved useful for comparison purposes. Finally, as work on tuberculosis is confined to a BSL3 facility, we used *Mycobacteria smegmatis* (smeg) as a representative bacteria. This related and noninfectious relative of Mtb has been used to produce F_{420} (Isabelle et al., 2002).

In order to assist lifetime measurements made on two photon excited fluorescence, the action cross-sections for purified F_{420} were quantified (see chapter 4 for details on this measurement) in PBS at the physiological pH 7.4 (the molecule becoming dim below that due to reduction). These were observed (figure 5.5a) to be relatively bright for an intrinsic fluorophore – with a peak fluorescence at 840nm that was roughly 4 times that of riboflavin (Zipfel et al., 2003) and even higher than that approaching 700nm, though these lower wavelengths are to be avoided in general as both they excite excessive background fluorescence and create photodamage.

As a preliminary test, lifetime measurements were made by recording single traces with high resolution on the SPC card's analog to digital converter (1024 time bins were used). So that although the system was scanning, all of the detected photons were compiled on an individual curve. When recorded at 840nm excitation, both F_{420} in solution and smeg in suspension yielded lifetime curves that could be fit with only a single

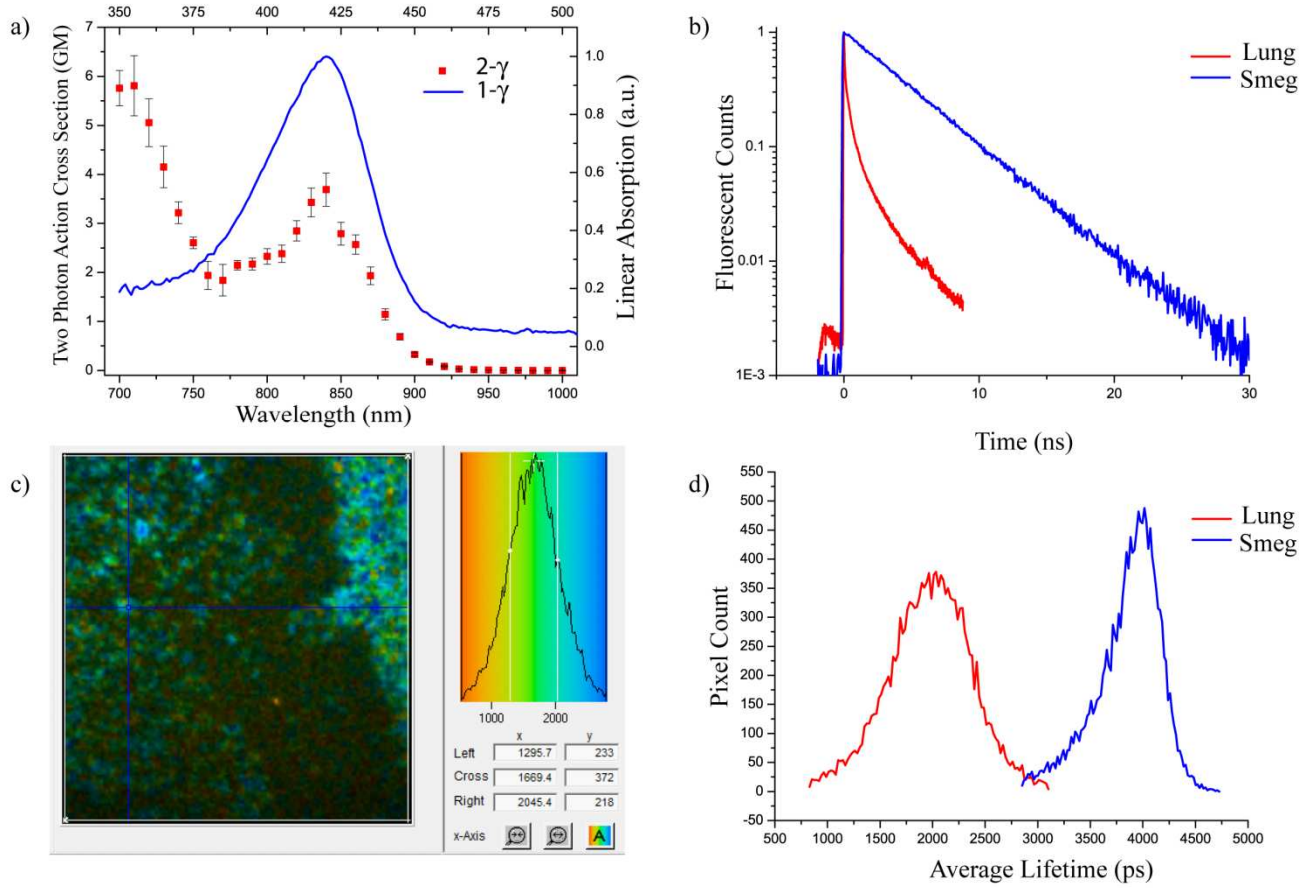

Figure 5.5 a) Linear and Two-photon Absorption of F_{420}. b) Two-photon lifetime of Lung tissue (~1.2ns) and smeg (~4ns). c) an example of the Becker and Hickl SPCImage software taken of lung tissue (left) and smeg (right) with pixel histogram. d) average lifetime pixel histogram derived from separate FLIM samples containing pure smeg or only lung taken at 420nm.

exponential (figure 5.5b – only smeg shown) having a decay constant of 4.2ns (χ^2=1.01). That both these curves should yield the same result confirmed that the F_{420} was the main source of fluorescence in the bacteria (at least within this excitation and emission band) and that it was present in the oxidised form within the cells. Next, the lifetime trace of lung tissue was measured and resulting in a decay that was both much shorter and more complicated (figure 5.5b). It required a multi-component fit and three exponentials still resulted in a higher χ^2, on the order of 1.2-1.8 per scan. However the average lifetime from scan to scan was relatively consistent at 1.2 ± 0.2ns (N=3). These results seemed encouraging enough to proceed to FLIM measurements.

Lifetime images were acquired on the SPC-830 card and analyzed using the Becker & Hickl SPCImage software. This software calculated a three exponential fit to each pixel trace and generated a pseudo-color image (figure 5.5c) from the average lifetimes - the color map of which was displayed in the software as a distribution of the picosecond pixel lifetimes (figure 5.5c top left). FLIM images of separate samples containing either smeg smears or lung tissue yielded average pixel lifetime histograms (figure 5.5d) with distribution mean similar to the single curve measurements, but with a much larger variance. The nature of acquiring an image rather than a single decay curve results in collecting fewer photons per trace (if the image is to be acquired in a reasonable amount of time) and necessitated a reduction in the number of time bins to 64 limiting the accuracy of the determination of the rate constant. Unfortunately, whether due to this lowered resolution or another, unknown factor, when the lung tissue and smeg were finally imaged together, they could not be spatially separated.

Doubling the beam to 420nm, yielded similar results as in the two-photon excitation experiments – when imaged separately, both tissues were easily resolvable (figure 5.5d), but imaged together the overall image contained broad average pixel lifetimes ranging from 2 to 4 ns, but with no spatial correlation to known smeg or lung location.

At this time, it remains unclear why the two samples when imaged together appear inseparable and a more systematic approach is necessary to elucidate this problem. It is possible that the system suffers from differences between the overall magnitude of lung and smeg fluorescence, the former being relatively airy, while the latter occurred in highly concentrated smears. Because FLIM is a photon intensive technique, even when done by time correlated single photon counting, an examination of the relative fluorescence intensity of different smeg concentrations may prove useful – it would interesting to know the minimum detectable concentrate of bacteria in solution, especially since F_{420} is known to be photo-liable (Cheeseman et al., 1972). Also, having a better way of preparing the "mixed" sample so the two species could be isolated into separate regions (rather than just mashed together) that could be imaged simultaneously, repeating hopefully the results of figure 5.5d. This would rule out whether the problem might lie in the Becker & Hickl software itself, which is fairly old, and not particularly flexible. In fact, FLIM custom software based on a global analysis has been demonstrated to provide superior discrimination to the Becker & Hickl routines (Chia et al., 2008). Should a solution to this problem be found, the usefulness of this technique would be unquestionable, especially if coupled to a low-cost system that could employed at clinics in the field.

Acknowledgements

This work was generously funded by a grant from the Bill and Melinda Gates Foundation as part of a multidisciplinary, multi-institutional effort led by JoAnne Flynn of the University of Pittsburgh Medical School. Robert Abramovich provided the smeg and is developing the reporting Mtb strains in the Russell Lab at Cornell. Katherine Kieckhafer of the Lis Group provided the Dronpa samples.

REFERENCES

Balaji J, Garai K, Chakrabarti S, and Maiti S, " Axial Resolution Limit of a Fiber-Optic Fluorescence Probe" App. Opt. **42** 3780-3784 (2003)

Barry CE and Cheung MS, "New tactics in the fight against tuberculosis" Scientific American February 23, 2009

Cheeseman P, Toms-Wood A, Wolfe RS, "Isolation and Properties of a Fluorescent Compound, $Factor_{420,}$from *Methanobacterium* Strain M.o.H. " Journal of Bacteriology, **112** 527-531 (1972)

Chia TH, Williamson A, Spencer DD, Levene MJ, "Multiphoton fluorescence lifetime imaging of intrinsic fluorescence in human and rat brain tissue reveals spatially distinct NADH binding", Opt. Ex. **17** 4238- 4249 (2008)

Deyl Z, Macek K, Adam M, and Vancikova O, "Studies on the chemical nature of Elastin fluorescence." *Biochim.Biophys.Acta* **625**, 248-254. (1980)

Elson DS, Galletly N, Talbot C, Requejo-Isidro J, McGinty J, Dunsby C, Lanigan PMP, Munro I, Benninger RKP, de Beule P, Auksorius E, Hegyi L, Sandison A, Wallace A, Soutter P, Neil MAA, Lever J, Stamp GW, and French PW, "Multidimensional Fluorescence Imaging Applied to Biological Tissue", Reviews in Fluorescence 477-524 (2006)

Ghosh J, Larsson P,Singh B, Pettersson BMP, Islam NM, Sarkar SN, Dasgupta S, Kirsebom LA, "Sporulation in Mycobacteria" PNAS **106** 10781-10786 (2009)

Hüttenberger D, Gabrecht T, Wagnières G, Weber B, Linder A, Foth HJ, and Freitag L, "Autofluorescence detection of tumors in the human

lung—Spectroscopical measurements *in situ*, in an *in vivo* model and *in vitro*" Photodiagnosis and Photodynamic Therapy **5** 139-147 (2008)

Isabelle D, Simpson DR, Daniels L, "Large-Scale Production of Coenzyme F420-5,6 by Using *Mycobacteria smegmatis,*" App. Env. Microbiology **68** 5750-5754 (2002)

Jung JC and Schnitzer M, "Multiphoton Endoscopy", Opt. Letters **28** 92-94 (2003)

Keeler E, Perkins MD, Small P, Hanson C, Reed S, Cunningham J, Aledort JE, Hillbourne L, Rafael ME, Girosi F, Dye C, "Reducing the global burden of tuberculosis: the contribution of improved diagnostics" Nature Sup. 1 49-57(2006)

Lakowicz JR, "Principals of Fluorescence Spectroscopy," Springer, (2006) Chapter 4

Lin PL, Rodgers R, Smith L, Bigbee M, Myers A, Bigbee C, Chiosea I, Capuano SV, Fuhrman CV, Klein E, and Flynn JL, "Quantitative Comparison of Active and Latent Tuberculosis in the Cynomolgus Macaque Model" Infect. And Immunity **77** 4631-4642 (2009)

Marriott G, Mao S, Sakata T, Ran J, Jackson DK, Petchprayoon C, Gomez TJ, Warp E, Tulyathan O, Aaron HL, Isacoff EY, and Yan Y, "Optical lock-in detection imaging microscopy for contrast-enhanced imaging in living cells" PNAS **105** 11789-17794 (2008)

Njoroge JM, Mitchell LB, Centola M, Kastner D, Raffeld M, and Miller JL, "Characterization of Viable Autofluorescence Macrophages Among Cultured Peripheral Blood Mononuclear Cells" Cytometry **44** 38-44 (2001)

Patiño S, Alamo L, Cimino M, Casart Y, Bartoli F, García MJ, and Salazar L "Autofluorescence of Mycobacteria as a Tool for Detection of *Mycobacterium tuberculosis*" Journal of Clinical Microbiology, **46** 3296-3302 (2008)

Russell DG, "Who puts the tubercule in tuberculosis" Nat. Rev. Microbiology **5** 39-47 (2007)

Steingart KR, Ramsay A, Pai M"Optimizing Sputum Smear Microscopy for the Diagnosis of Pulmonary Tuberculosis" Expert Rev. Anti. Infect. Ther. **5** 327-331 (2007)

Udovich JA, Kirkpatrick ND, Kano A, Tanbakuchi A,Utzinger U, and Gmitro AF, "Spectral background and transmission characteristics of fiber optic imaging bundles" App. Opt. **47** 4561-4568 (2008)

Via LE, Lin PE, Ray AM, Carrillo J, Allen SS, Eum SY,Taylor K, Klein E, Manjunatha U, Gonzales J, Lee EG, Park SK, Raleigh JA, Cho SN, McMurray DN, Flynn JL, and Barry CE, "Tuberculous Granulomas Are Hypoxic in Guinea Pigs, Rabbits, and Nonhuman Primates" Infect. And Immunity **76** 2333-2340 (2008)

World Health Organisation "Treatment of Tuberculosis – Guidelines for National Programs" Geneva Third Edition (2003)

Zipfel WR, Williams RM, Christie R, Nikitin A, Hyman BT, & Webb WW, "Live tissue intrinsic emission microscopy using multiphoton excited native fluorescence and second harmonic generation," PNAS, **100,** 7075-7080 (2003)

Chapter 6 – Looking Forward

The work that has been presented in this thesis represents a step in the natural progression of the research that will hopefully continue to evolve into unseen explorations of the natural world. There is never enough time to do everything that one would hope, and the very act of doing, seems to create more questions than answers. So it is satisfying to reflect for a moment on the future directions that this work might take, especially the applications that readily await some of the instrument here designed.

Although the work in the third chapter is essentially an extension of the CRD detector, the CRD has the advantage of being readily implemented and there are a number of experiments that would directly benefit from both the large increase in the fluorescence collection and the observed detection of scattering anisotropy. First of all, further study of its application to the quantification of diseased states by second harmonic generation collection, whether it be damaged or abnormal cartilage (Nadiarnykh et al., 2007) or in the extracellular matrix with and surrounding a tumor (Hompland et al., 2008) could be useful as it would eliminate the need for a forward detector, and therefore a thinned, prepared sample. If this was successfully demonstrated, the construction of a similar detection scheme might be implemented endoscopically using a CCD to gain spatial information from a scanned fiber bundle.

Another waiting experiment – hinted at from the work in the chapter – would be its application to the study of the neural networks of large scale calcium oscillations over a wide area. This was attempted in the preparation of the paper, but the combination of perfusion, the high temperature of the bath, and the encapsulation of the unit by the Teflon collar, created

condensation on the optics that all but eliminated image formation. Subsequent discussion with other researchers has suggested that infiltration with nitrogen gas would easily remedy this problem, as would potentially reducing the structure of the collar to its minimal possible volume. If the device was to be used in this context, the addition of a second channel would probably be necessary. Unfortunately, due to the high NA of the light guides this is not as easy as one would hope, and the solution would likely entail a large asphere to collimate and then focus throughput signal. This should probably be designed using code V or a similar program. With these relatively minor changes however, many interesting experiments could be attempted that would not be possible using merely the 4x objective.

The work in the third chapter is more of a proof of principle, an attempt to change the design paradigm for two-photon objectives, then a final blueprint for a new optic. That said, we have demonstrated an optic that has an unparalleled numerical aperture for a system with such a large field of view, and a fantastic collection efficiency far exceeding that of the Olympus macro lens. However, before the objective is constructed there are still considerations to be explored even before the manufacturing parameters are assessed. First of all, although aspheric surfaces were avoided in the design of the objective, the benefit of them should not necessarily be neglected unless they would drastically increase the cost of the unit. For example, making the inner surface of the final lens (the one closest to the sample) aspheric and running a quick optimization increased the numerical aperture of the water immersion unit to 0.40 with no loss of field of view. It might also be useful to make additional surfaces aspheric in order to shrink the diameter of the back aperture, as under-filling has been a problem when

using the 4x macro objective due to its width. Secondly, there are a number of design details that have yet to be investigated, but should be. The angle dependence of the dichroic surface was not considered when the scattering simulations were run and should be before the final design is made. What may be found is that periscoping the entry of the excitation beam is a more optimal solution (Figure 6.1a - this it should be added would not allow its use on a conventional microscope), or in fact that collection is highest when the detector axis is not perpendicular to the optical axis of the objective, but rather inclined to it (Figure 6.1b). There is also an angular dependence on the quantum efficiency of the detector photocathode that may reduce the sensitivity and side-on PMTs should be considered. As in the case of the CRD detector, collection would also benefit from more than one channel. A multi-detector scheme could be bulky so close to the sample, and so the use of a light guide to remove the detector pathway away from the focal plane (Figure 6.1b) may be necessary. Finally, although the imaging of a sample of great thickness was examined, one rarely images deeper than 500 microns. Unless one is imaging tissue *ex* or *in vivo*, slices of a maximum thickness of 1mm are often used. In this scenario the addition of a mirror (Combs et al., 2007) below the sample may be useful to further increase the collected solid angle (Figure 6.1). From these suggestions two things become obvious: there are many practical aspects to be investigated before the fabrication of the lens and these considerations should be tailored around a specific imaging scenario.

The fourth chapter clearly demonstrated the promise in the imaging of anti-cancer drugs, quantifying the fluorescence intensity of seven different agents, as well as demonstrating an order of magnitude enhancement in two-

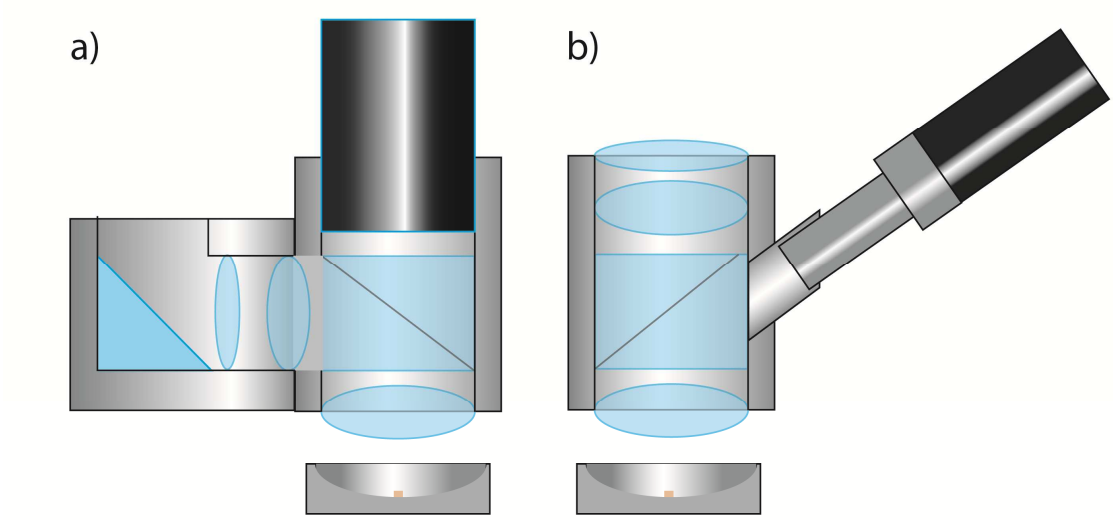

Figure 6.1- Potential modifications/additions to the objective design of chapter 3 including: a periscoped entry of the excitation beam a); inclination of the detector axis b); collection by a liquid light guide to be delivered to a distant detector b); and the mounting of a sample on a mirrored surface in order to enhance collection further (both).

photon imaging brightness with the drug irinotecan. This hopefully was enough to excite interest in the application of imaging cancer drug fluorescence by multiphoton endoscopy, however there is a lot of work that remains to be done even before attempting any imaging in human tissue. First of all, the uptake difference observed between the tumor and healthy tissue should definitely be explored more, although it will likely require a lot of work. Different time points taken at an hour, eight hours, even a day after injection are required to demonstrate what may turn out to be an enhancement of this uptake. For the longer time frames, the by-product of irinotecan hydrolysis may become apparent and therefore spectroscopic imaging of the tumors should likely accompany this study. Additionally, as the camptothecin analogue topotecan has been demonstrated to have a high cross-section (Gryczynski et al., 1999) repetition of the study with its commercial equivalent Hycamtin could be fruitful. Incidentally, the authors of that paper have patented the two-photon excitation of the camptothecin family in blood plasma as a way of monitoring drug clearance. Repeating this with another of the measured drugs, for example doxorubicin, would be relatively simple and potentially quite useful. Another scenario that might be really interesting (sort of "the ultimate experiment") would be to attempt to image the drug, injected intravenously, and to observe particularly its diffusion away from the blood vessel. This would be very difficult and particular care would have to be taken to choose the correct tumor model as the vascular in the ovarian epithelia model seemed if not non-existent, then very disorganised and erratic.

The work discussed in chapter 5 relating to the detection of tuberculosis in vivo was part of a large scale consortium that will continue

for at least another. The bronchoscope was demonstrated to be capable of imaging auto-fluorescence *in vivo* in the lung (at least of pig if not primate). As mentioned previously, on-site testing will likely dictate any necessary changes that need to be made and the current design has been purposefully kept flexible as a result. If, for example, a higher numerical aperture objective was elected as a better alternative to a bare fiber face, the system might benefit from the application of a structured illumination scheme which could provide some modest sectioning capbility. This scheme, as it has been implemented previously (Bozinovic et al., 2008), requires an expensive spatial light modulator and therefore the cost of this application should be weighed against its overall benefit.

One avenue that may prove extremely fruitful to implement would be the development of a multiphoton thoracoscope. Rather than a flexible nonlinear endoscope which is quite complicated to design, one could imagine the construction of a rigid system using a system of relay lens. This system might be dispersive, but it would not generate self phase modulation and therefore could be readily compensated. The system then, aside from being able to readily excite the implanted fluorophores, and the capability to section the tissue, would also have access to SHG from the abundant collogen both in the lung and surrounding the granulomas. It's also possible that the Olympus stick lenses could be immediately used (depending on the animal model in question), without the need to design a relay system. If a proper thorascope was constructed, one would imagine that it could translate into humans without too much difficulty.

The detection of the wild type tuberculosis bacillum by lifetime imaging looks promising from the preliminary work that has been

performed. Originally, this lifetime detection scheme was envisioned as a potential diagnostic tool through a fiber bundle based endoscope. However, the auto-fluorescence arising from the cladding between the fibers for 420nm excitation would preclude its use in this regard. Assuming the kinks in the project are figured out, and the F_{420} and background signals readily separated, the thoracoscope could provide a useful, though invasive, method of *in vivo* detection. On the other hand a single silica fiber could be delivered bronchoscopicly as a point test source, without the imaging ability of a scanning system. Unlike most scientific endeavours, the main considerations here should be governed by a cost benefit analysis, as there is little point in building a device that is too expensive to use in a clinic in the developing world.

REFERENCES

Bozinovic N,Ventalon C,Ford T,Mertz J," Fluorescence endomicroscopy with structured illumination", Opt. Express **16** 8016-8026 (2008)

Combs C, Smirnov A, Riley J, Gandjbakhche A, Knutson J, Balaban R,"Optimization of multiphoton excitation microscopy by total emission detection using a parabolic reflector," J. of Microscopy **228** 330-337. (2007)

Gryczynski I,Gryczynski Z, Lakowicz JR, Yang D, Burke TG "Fluorescence Spectral Properties of the Anticancer Drug Topotecan by Steady-State and Frequency Domain Fluorometry with One-Photon andMulti-Photon Excitation" Photochemistry and Photobiology, **69** 421-428 (1999)

Hompland T, Erikson A Lindgren M, Lindmo T, de Lange Davies C, "Second-harmonic generation in collagen as a potential cancer diagnostic parameter" J Biomed Opt **13** (2008)

Nadiarnykh O, Plotnikov A, Mohler WA, Kalajzic I, Redford-Badwal I, Campagnola PJ,"Second harmonic generation imaging microscopy studies of *osteogenesis imperfect*" Journal of Biomedical Optics **12** 051805-1:9 (2007)

APPENDIX A

The Collection Efficiency of a Metal Can

When considering the design of the objective that became the one found in chapter 3, it was interesting to examine an existing 40x/0.7 NA air objective that came as a Code V stock lens (Figure A.1a). The non-sequential ray tracer Lighttools was used to tally the total number of photons isotropically emitted from a point source at the focus of this objective which found their way to a receiver placed at its back aperture (Table A.1, Figure A.1b). The objective collected 14% of the total flux, the equivalent (using equation 2 from chapter 3) to an NA of collection of 0.7 as expected. An absorptive metal can, made to enshroud the objective, was aligned between the point source and the receiver and found to pass only 3% of the photon flux through its clear aperture relative to the objective lens. Making the interior of this can reflective proved to drastically increase the number of photons transmitted, by effectively translating the base of its cone of acceptance from its back aperture to its front. In this configuration it

Table A.1 – Measurement of the system flux

System	Total Flux (%)	Relative Collection (%)
Objective Only	14.09	100
Absorptive Can	0.39	3
Reflecting Can	37.62	268
Objective + Reflecting Can - Abs. Edges	21.69	155

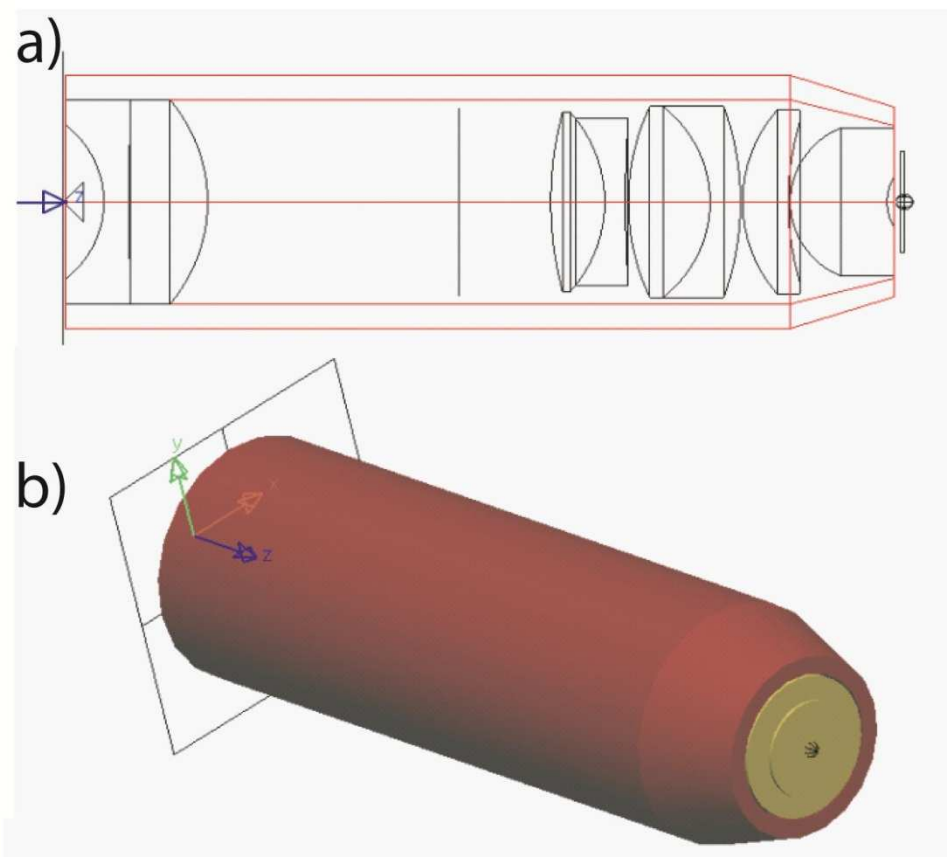

Figure A.1 – a) the cross-section of a Code V stock objective (40x/0.7 NA) encased within an aluminum can. b) the lens in CAD view in Lighttools. A point source can be seen at the focus of the lens, as well as the square receiver at the back aperture used to detect the photons.

bettered the objective by almost a factor of three. In fact, when the objective was placed inside of this reflecting can, and the absorptive optical coatings were removed from all lateral lens surfaces, the transmission was only 60% of that of the bare can. These losses can be accounted for from light that had been "turned around" by total internal reflection (TIR) off the glass surfaces, so that it exited the objective system through the front aperture. This was compounded by the fact that, despite possessing a relatively low NA for its magnification, the objective was fairly complex - containing 5 elements and 13 surfaces, most of which were required to minimize chromic aberration.

These simulations were fundamental to the basic design paradigm of our new type of two-photon objective. The success of the reflective casing at collecting "fluorescence", led to its inclusion in our system. Conversely, in order to minimize the loss from TIR, the number of lens elements was kept low. This was possible as a two-photon microscope does not have to worry about the confocality of its detector system, and thus chromatic aberration is not an issue. Additionally, by incorporating a dichroic beam splitter directly following the front lens, the photons were collected after only three surfaces, minimizing reflective losses.

APPENDIX B

The Assessment of Microstructured Fiber for Two-Photon Endoscopy

One of the difficulties of translating two-photon microscopy from the lab into the clinic is the delivery, deep within the body, of the ultra-short (100fs) pulses necessary to achieve nonlinear excitation. Fiber delivered endoscopes employing traditional single mode fibers (SMF) (Helmchen et al., 2001) are hampered by pulse broadening due to the high intensities caused by the beam confinement within the micron diameter fiber core. Building off work previously performed in the lab (Ouzounov et al., 2003), what follows is an assessment of the capability of the 25 μm microstructured (MSF) fiber (Crystal Fibre, Figure B.1a), to deliver spatially clean, ultra-short laser pulses for its intended use in multiphoton endoscopy. This fiber consists of a 25 micron inner glass core surrounded by a ring of air filled capillaries. Although it is technically a multimode fiber and has a correspondingly high numerical aperture (NA ≈ 0.6), the large index mismatch between the glass/air interface not only provides the index mismatch to guide the light via total internal reflection, but also serves to limit modal coupling. Unlike other large core fibers with good single mode characteristics (Helmchen et al., 2002) it is fully flexible. With its potential use in mind, it was important to consider both the spatial and temporal quality of its delivered beam, as well as its capability to collect the target fluorescence.

Beam Delivery

In order to maximize the multiphoton fluorescent signal relative to the focal volume, it is necessary for the laser pulse to approximate a Gaussian in three dimensions. A conventional single mode fiber delivers

perfect $TEM_{0,0}$ modes, however it broadens the pulse out in time due to mechanisms including: group velocity dispersion (GVD) from the variation in refractive index throughout the bandwidth of the pulse, and self phase modulation (SPM) in which the refractive index becomes intensity dependant due to the large powers confined within the narrow volume of the core. While the former characteristic can be linearly compensated for, the later is much harder to compensate cleanly (Lelek et al., 2008). As a result, for peak powers above 250 pJ, the pulse is stretched from an initial 100 fs out to a few ps. The larger core of the MSF essentially eliminates this effect. By applying a negative pre-chirp with a grating compressor (Figure B.1b) to compensate for the positive dispersion of the glass core, it is possible to deliver pulses of sub 200 fs duration. The delivered pulse widths from 3 meters of grating compensated fiber were assessed by interferrometric autocorrelations. These demonstrated that that the dispersion in the lowest mode could be effectively compensated for, even at higher powers, with a grating scheme (Figure B.1c). They also indicated presence of higher order modes which appeared in the side bands seen in traces. These lobes were a result of the correlation of the main $TEM_{0,0}$ mode with a slightly delayed higher order mode (the different modes have different wave vectors and thus propagate at different speeds). In general though, the bulk of the pulse energy could be recovered, with only minimal broadening for pulse energies of up to 3 nJ (Figure B.1d) and that was likely caused by third order dispersion acquired by passing through the Pockels cell. In fact, the diffraction gratings could compensate for all the glass in the optical path: the Pockels cells or acoustic optical modulator; the faraday

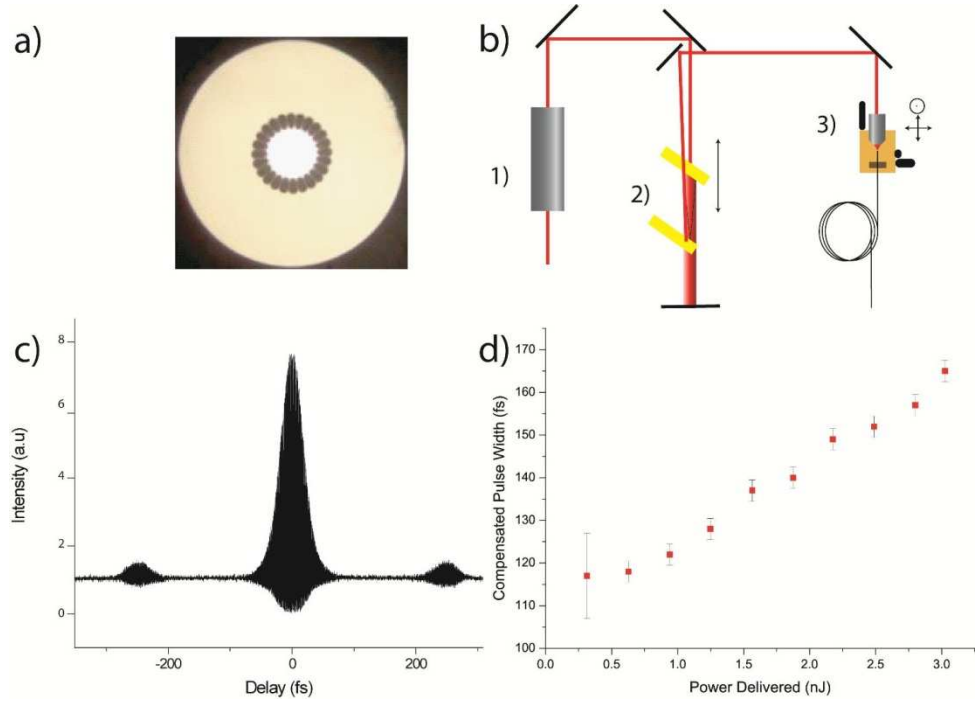

Figure B.1 - a) the cross-section of the 25 μm core MSF from Crystal Fibre. b) a grating compensator system consisting of 1) a faraday isolator to reject back-reflected components 2) the folded diffraction grating pair used to create negative dispersion 3) the three axis fiber launcher and objective. c) the interferrometric autocorrelation of a 3 nJ pulse delivered through 3m of fiber. The central mode shows little chirp, however the side lobes indicate the presence of delayed higher order modes within the beam. d) compensated pulses under 200fs delivered through 3m of fiber.

isolator; the objective lenses, and scanning optics as well - delivering a pulse approximately 3 times shorter than in an uncompensated system microscope. This results in a similar increase in fluorescence and as a result pre-compensators are now appearing in commercial systems (ie the Spectra Physics Deep Sea).

While the temporal character of the beam may be easily characterized by the use of an autocorrelator, the spatial dimensions were harder to assess, as the profile was variable depending on the condition of the fiber and coupling alignment. Cleavage of the fiber was especially difficult as it was particularly brittle and so great care (and often several attempts) were taken to produce a clean fracture. One method of assessing beam quality was to literally take a picture of the beam in the far field using a CCD camera which served to provide a qualitative measurement of beam composition (Figure B.2a). This initial image was somewhat noisy due to dust accumulation on an inner neutral density filter of the camera and was smoothed using and algorithm in the image analysis software image J to give Figure B.2b. The cross-section was taken along the indicated line and fit to a gaussian with fairly good agreement.

This assessment needs to be viewed with caution as the higher order modes present in the autocorrelation may have simply been drowned out by the lowest mode. A more quantitative method of characterizing the modal profile is by measuring the divergence of the beam when loosely focused (Denisov and Karasik, 2009). The Gaussian mode ($TEM_{0,0}$) will focus (of all the modes) to the tightest possible spot. The amount of deviation from this smallest waist can be related to the M^2 quality factor by the following relationship:

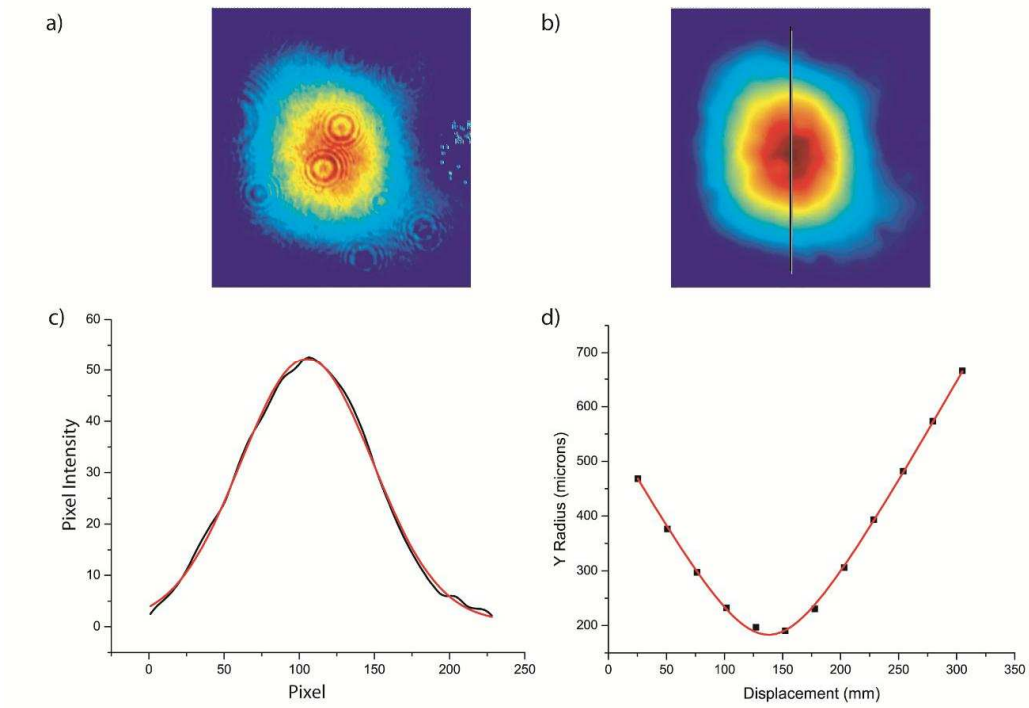

Figure B.2 – Far-Field profiles of the beam imaged directly by the ccd a) and then filtered b). A fit c) (red) of the cross-section (indicated by the black line in b) to a guassian shows good agreement. The measured beam waist d) for a loosely focused beam out of the SMF fiber and the corresponding fit to equation 1 in order to determine the M^2 value.

$$\omega_R(z) = \omega_{0,R}\sqrt{1 + \left(\frac{M^2\lambda z}{\pi\omega_{0,R}^2}\right)^2} \quad 1)$$

where ω_R (z) the beam waist at distance z from $\omega_{0,R}$ -the observed minimum waist – for a beam of given wavelength λ. The M^2 measurement was made by loosely focusing (f=50cm) the collimated output of a fiber and then measuring its beam width past the focal spot using a scanning knife edge beam profiler (Thorlabs Omega WM100) displaced in steps by a micrometer. The resulting curve was fit to equation 1) yielding a value for M^2 as in Figure B.2d. Measurements (Table B.1) were taken for the beam: directly out of the Mai Tai Ti:Sapphire laser; through the SMF; and through the MSF. The

Table B.1 – M^2 measurements On Various Beams

Source	M_x^2 Value	M_y^2 Value
Mai Tai	1.26	1.21
SMF	1.10	1.11
MSF (no gratings)	2.00	1.75
MSF (gratings)	2.82	2.95
MSF (bad profile)	5.43	5.41

resulting values were noticeably higher for the MSF, although not terribly - especially when no gratings were used (the gratings used in this experiment were several years old and their transmitted beam profile was noticeably poor).

As a final means of assessing the modal nature of the beam, measurements of the point spread functions of sub-resolution beads were performed by collimating the beam after the fiber and using it as the source for a Biorad multiphoton microscope. Preparations of 200nm fluorescent beads (Polysciences Inc.) were diluted in water and evaporated onto glass slides, then imaged with a 20x/0.75NA Olympus objective using

illumination directly out of the tsunami, as well as through the fiber/grating system. The results in Table B.2, show a broadening of the point spread functions for the fiber delivered light relative to the typical beam (as one would expect from the difference in M^2 values), but the deterioration seems reasonable. One should remember that the point spread functions are of the square of the intensity, whereas the M^2 value is linear and therefore the higher order modes may in effect be "cleaned up" by the nonlinear absorption process.

Table B.2 - Measured Point Spread Functions of 200nm Beads

Axis	Directly From Tsunami 1/e radius (nm)	Fiber Delivered 1/e radius (nm)
ω_x	428±8	493±20
ω_y	4445±7	495±20
ω_z	1620±20	2070±80

Signal Collection

It is important to consider the signal collection capability of the fiber system, especially if the same fiber is to be used for both delivery and collection. Although the total two-photon fluorescence is independent of the numerical aperture of the focusing objective, a higher NA objective will collect a greater amount of the solid angle of the isotropic radiation. In the same way, the collection capability of a fiber optic will be enhanced by having a higher NA, for although the light may be coupled into the fiber with a suitable lens, deviations will occur because the source of fluorescence is not a point and may lie in a highly scattering medium. Also, a larger core (and this is typically related to NA) will allow for ease of alignment when directing the relatively small focal spot of the coupling lens into the fiber. This is turns out to be quite important as it is difficult to correct for the

extreme wavelength difference between the excitation and emission photons in the miniaturized objectives used for two-photon endoscopy. This in turn hinders the epi-coupling of the fluorescence resulting in poor imaging performance (Miang et al., 2006).

The collection characteristics of the fiber were investigated by scanning the focal spot of the 488nm line from an argon laser across the core of the fiber, in order to get a sense of the effective "active area" of the fiber. This was performed by first maximizing the amount of light coupled into the fiber and then laterally misaligning the tip. The fiber was then brought back into place by manually adjusting the micrometer on the fiber mount in 1 micron increments. These displacements were plotted (Figure B.3a) as a function of the % of light coupled into the fiber – that is the power exiting the fiber divided by the power after the coupling objective. For the MSF, a variety of aspheric objectives of increasing numerical aperture were used to couple the light, consistent with the fact that this is a high NA fiber. The SMF being of low NA, only the lowest numerical aperture lens could be used to transmit light. It is evident from the figure, that the coupling efficiency is much greater for the larger cored MSF – approaching 90% of the excitation beam. It is also interesting to note that although the apparent width of that fiber was 25 μm, the effective width is smaller, on the order of 15 μm (FWHM).

Another experiment was performed in an attempt to evaluate the performance of the fibers in a more applicable orientation (Figure B.3b). In this case the laser light was coupled into the fiber with objective L1 and then the output light collimated with objective L2. This collimated beam was then focused down by a 40x 0.9Na objective and used to excite fluorescence

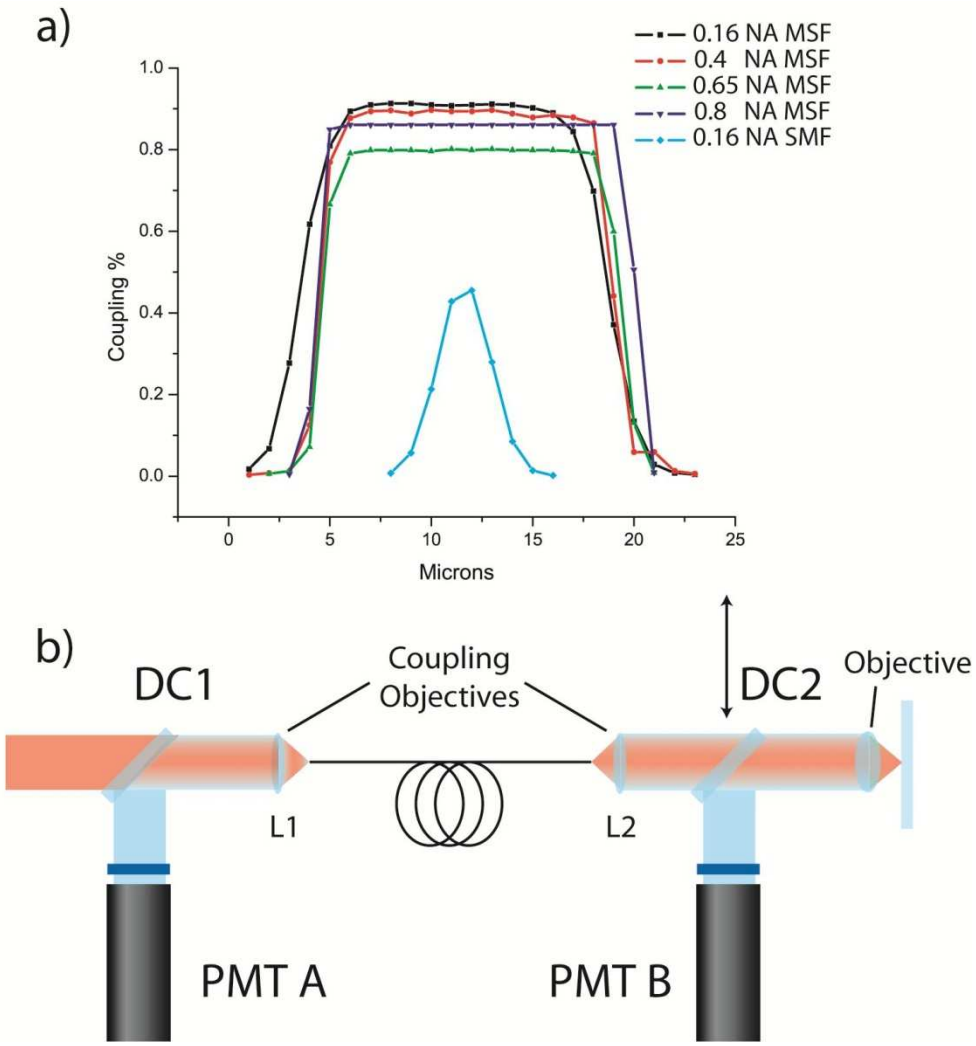

Figure B.3 - a) Coupling percentage as a function of lateral displacement of the focus on the core of the fiber for the SMF and MSF fibers. b) The setup used to determine re-coupling of fluorescence into the SMF or MSF fiber. L1 and L2 are coupling objectives, DC1 and DC2 are dichroics.

in a blue plastic slab (Chroma). The fluoresced light was directed onto a BGG22 (Chroma) shielded PMT B via the movable dichroic mirror DC2, where the incident photons were counted. The mirror was then removed and the light coupled through L2 and back via a similar arrangement into PMT A. The alignment of the fiber and L2 were then tweaked to maximize the ratio of counts in PMT A to PMT B. The measurement of scattered as opposed to fluoresced light was then corrected for by detuning the laser to eliminate modelocking and again counting photons at a similar initial power. Thus, one was able to deduce the approximate ability of the two fibers to collect the fluoresced light by comparing them for similar arrangements of L1 and L2. The results are summarized in Table B.3 for a variety of coupling objectives, and indicate that the collection efficiency of the larger cored fiber betters the SMF by nearly 20 times.

Table B.3 - Summary of the Observed Transmission of Fluorescence Through the Two Fibers

Objective (Mag/NA)		MSF	SMF	Total
L1	L2	Coupling %	Coupling %	Enhancement
4x/0.1	3x/0.07	7	.4	18
4x/0.1	10x/0.16	20	14	14
10x/0.16	10x/0.16	10	12	8

Summary

To conclude, the delivery of ultra-short pulses was demonstrated for beams of several nanojoules of peak power through over 3m microstructured fiber. The spatial characteristics of these beams had deteriorated relative to a typical Ti:Sapphire light source or single mode fiber, although it was found to be still good enough for the purpose of sub-micron imaging. In addition, the benefit of the larger core

diameter/numerical aperture of the MSF for fluorescence collection (relative to that of a traditional SMF) was demonstrated (at least on the table top).

REFERENCES

Denisov DG, Karasik VE, "Experimental Estimation of the Quality of a Laser Beam" Measurement Techniques **52** 260-265 (2009)

Helmchen F, Fee M, Tank D, Denk, W, "A Miniature Head-Mounted Two-Photon Microscope: High-Resolution Brain Imaging in Freely Moving Animals" Neuron **31** 903-912 (2001)

HelmchenF, Tank D, Denk W, "Enhanced two-photon excitation through optical fiber by single-mode propagation in a large core" Applied Optics **41** 2930-2934 (2002)

Lelek M, Suran E, Louradour F, Barthelemy A, Viellerobe B, Lacombe F, "Coherent femtosecond pulse shaping for the optimization of a non-linear micro-endoscope" Optics Express **15** 10154-10163 (2008)

Myaing MT, MacDonald DJ, Li X, "Fiber-optic scanning two-photon fluorescence endoscope" Optics Letters **31** 1076-1078 (2006)

Ouzounov DG, Moll KD, Foster MA, Zipfel WR, Webb WW, Gaeta A, "Delivery of nanojoule femtosecond pulses through large-core microstructured fibers" Optics Letters **27** 1513-1515 (2002)

APPENDIX C

Protocol for the Measurement of Two-Photon Action Cross-Sections

Introduction

This appendix outlines the procedure for the measurement of two-photon action cross-sections with "The Edotron". We have constructed this automated system to mitigate the tedium of a standard measurement. The device measures a plot of fluorescence generated as a function of excitation power. Given that the fluorescence may be defined as:

$$F = \sigma_2^* C\phi\left(g\langle I\rangle^2 \int_{-\infty}^{\infty} psf^2\, d\Omega\right) \quad (1)$$

the slope of this plot, S = (σ_2^* C ϕ g), can be readily determined. Here g is the second-order coherence of the excitation light, σ_2^* is a molecule's two-photon action cross-section, C its concentration, and ϕ the wavelength calibrated collection efficiency of the system. This last term is given by:

$$\phi = \int Q(\lambda)F(\lambda)T(\lambda)\, d\lambda \quad (2)$$

where Q is the detector quantum efficiency, T the spectral response of the collection dichroic/filter system, and F the fluorescence emission lineshape. One can obtain the unknown action cross-section by ratioing a calibrated slope for this molecule to that from a reference solution such as fluorescein in 0.1N NaOH (the cross-section of which is known precisely).

$$\sigma_{2,unk}^* = \left(\frac{S_{unk}}{S_{ref}}\right)\left(\frac{\phi_{unk}}{\phi_{ref}}\right)\left(\frac{C_{unk}}{C_{ref}}\right)\sigma_{2,ref}^* \quad (3)$$

A more detailed discussion of this measurement can be seen in Xu and Webb, 1996, which has been referenced in chapter 1.

Sample Preparation

In order to quantify the action cross-section, it is necessary to know the concentration of the molecule as accurately as possible. In cases where this value is suspect, it can be estimated by linear absorption in the spectra-photometer. If the absorptivity of the molecule is not known, FCS may be performed to estimate its concentration in solution. In general the concentration should be kept as low as possible to avoid self-screening effects. Concentrations around 1 μM are usually fine, but may need to be increased (or decreased) for extremely dim (or bright) compounds. Before the measurement is to be made a fluorimeter should be used to measure the linear emission. One should remember that though it will be consistent with the two-photon fluorescence emission, it is possible that it will vary with solvent and therefore a solvent specific emission curve should be used. Finally, about a millilitre of sample should be placed in the semi-micro quartz fluorimeter cells (Starna Cells) for measurement. As mentioned in the introduction a sample of 1 μM fluorescein in 0.1N NaOH is also required as a reference. In order to cancel out any solvent scattering or reflections, a blank sample of only solvent is also required. In addition to these two references, seven compounds may be measured at a time.

Hardware

The measurement of all seven samples is a fully automated process. Once initiated, it allows the user to walk away while the measurements are being taken. The key to this mechanisation is the MaiTai laser (Spectra Physics) which can be computer controlled to move to a directed wavelength, where it auto-modelocks. The beam intensity is regulated by a

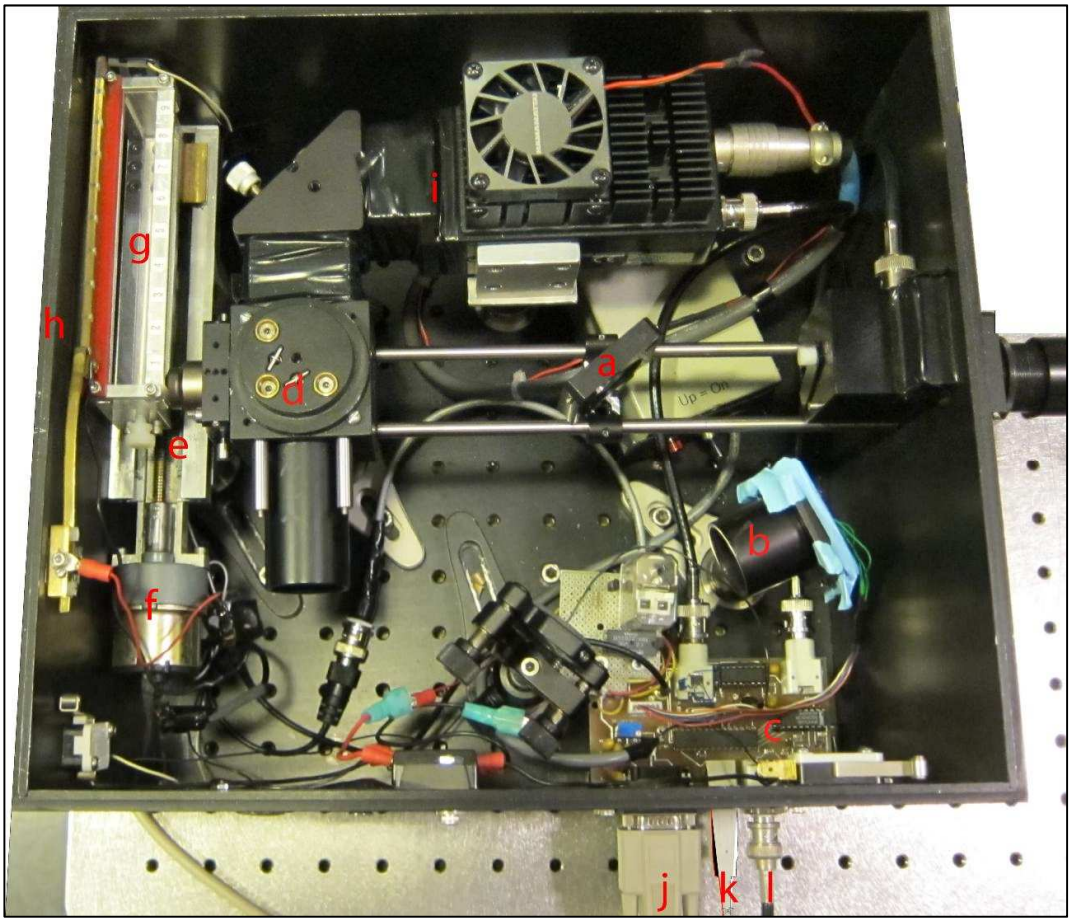

Figure C.1 – An overview of the Edotron. The beam enters from the right, a fraction of which is deflected by an IR coated coverslip a) and directed on to a photodiode circuit b) the output of which is read by the microcontroller c). The majority of the beam passes through the 680SP dichroic d) to be focussed by the aspheric objective e) into a quartz cuvette (not shown). The motor f) translates the cuvette rack g) until the closed circuit made by the brass arm h) is opened. Fluorescence is collected by the GaAsP Photon counting PMT (Hamamatsu H7421) i) through 700SP and 720SP filters. Power is supplied to the system through the serial cable j). The microcontroller communicates as an HID device through USB k). Finally the beam intensity is modulated by a co-axial connection to a Pockels Cell Driver l).

Pockels Cell (Con Optics) and an ND filter wheel (Thorlabs) – it's important that it is attenuated in that order.

The Edotron (pictured in Figure C.1) is governed by a PIC18F (Microchip) microcontroller running C script written in the CCS compiler. On entering the Edotron the beam should be aligned through the optical axis of the 20x aspheric objective (New Focus - Figure C.1e). A portion of this beam is reflected by an IR coated coverslip (Figure C.1a) and, after passing through a diffusive glass to eliminate any irregularities due to dust etc., is directed onto a photodiode circuit. This light to frequency converter (Taos Inc.) produces a square wave the frequency of which corresponds to the intensity of the incident light. It is used to drive the counter of another PIC microcontroller which is polled by the central unit. It is crucial that the beam is centered on the photodiode using the adjustable mirror in order to achieve a proper I^2 fit. I wrote a C# program "Pockels Cell Tester" which may be used to determine and maximise its 16bit output (done with a low voltage applied to the Pockels Cell). The laser intensity is regulated by applying a voltage between 0 and 2V to the Pockels Cell driver through the co-axial connection (Figure C.1l). The ND filters should also be set at this time as the Pockels Cell alone will not provide sufficient attenuation because the A/D used to control its voltage is only 8 bit. Without the ND Filters, the beam will saturate the photodiode and not provide enough dynamic range for the curves. With the laser tuned 800nm (or maximal output) Pockels Cell should be set to increasing values until 64k is reached. If this value is not reasonable (~200) then the ND filter should be increased.

Once that is accomplished the cuvettes should be loaded into the rack Figure C.1g. The blank must occupy position 1, followed by the fitc in

position 2, and then the remainder of the samples. Care should be taken to make sure the beam is focused into the center of the cuvette, and that all cuvettes are firmly seated in the rack. Empty cuvettes should be used as space fillers for partial runs. A knob on the side of the rack may be used for minor adjustments and to ensure a snug fit. During the run, the motor (Figure C.1f) is used to translate the cuvette rack from position to position until the closed circuit made by the brass arm (Figure C.1h) is opened, halting progress. Fluorescence is collected by the GaAsP Photon counting PMT (Hamamatsu H7421) (Figure C.1i) through 700SP and 720SP filters. These filters and the dichroic have been calibrated in the software and must not be changed! The TTL output of the PMT is counted by the central microcontroller, whose tally has been confirmed to correspond directly to photon counts. Power is supplied to the system through the serial cable (Figure C.1j) from the custom power box. Finally, the microcontroller communicates as an HID device through USB (Figure C.1k) with the operating software. After initial calibration (upon power on) in which the cuvette rack scans the range of its motion (the lid must be on for this to be achieved) it waits to receive ascii commands via USB.

Software

Before running the software a data folder should be created. This should include a separate text file with a normalised emission curve for each sample to be measured (including the fluorescein and the blank). These should be formatted as two tab delimited columns with the headings wavelength and counts. An additional text file is needed containing, again in tabs delimited columns, each sample and its concentration in micromoles. It

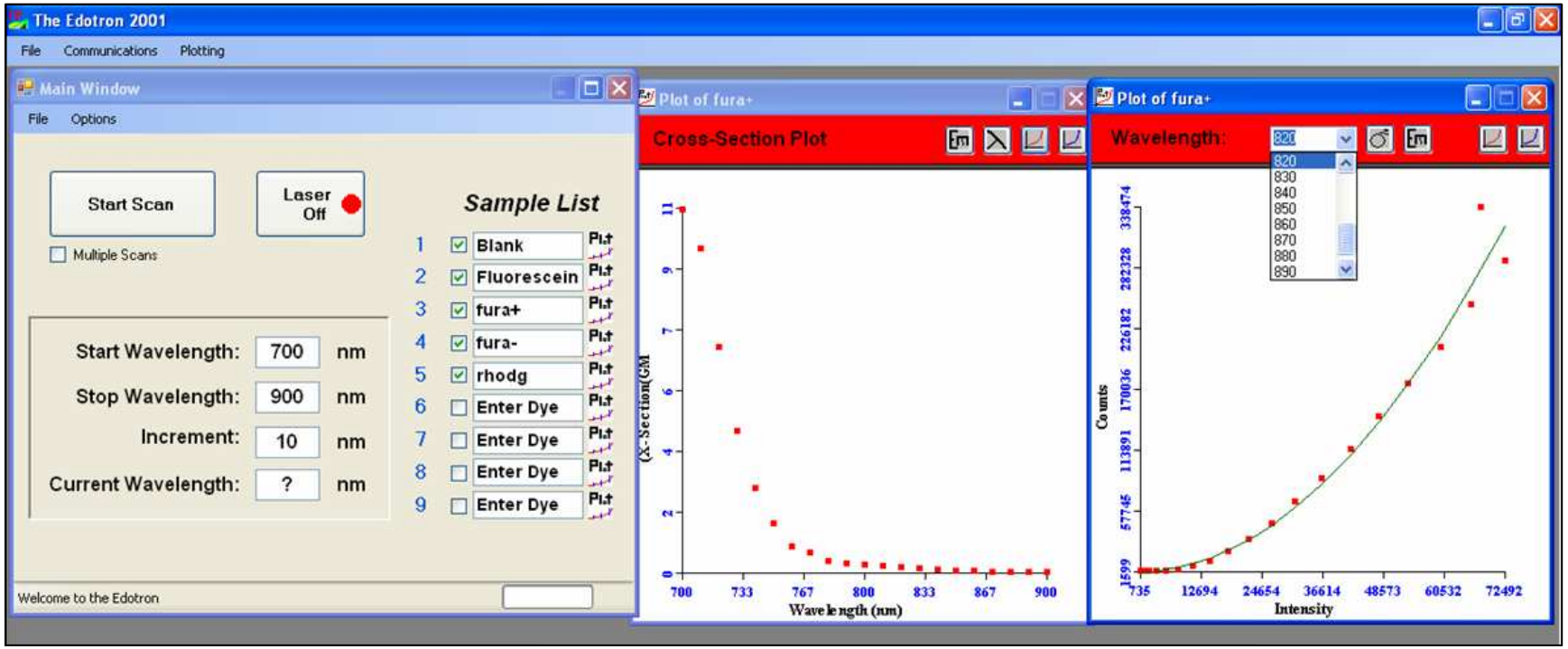

Figure C.2 – A screen shot of the cross-section acquisition software. The samples are input into the main window, as is the selected wavelength range. The plot button beside each sample calls up a window that displays emission, cross-section, and wavelength I^2 curves. The plot data may either be shown as a line plot or individual data points by toggling the red curve icon. A fit of the data is also displayed by the top right toggle button in the plot window.

is important that each of the samples listed in this file have the same spelling and punctuation as the file name of their emission curve (minus the .txt).

The main operating software (Figure C.2) was written in Microsoft Visual C# and is typically run in debug mode in Visual Studio on the Sony Viao laptop. Upon loading, it attempts to communicate with the laser, which should be turned on before hand and connected by a serial cable to the laptop. If the connection has failed you may need to adjust the COM port in the communications dialogue box. To run a scan, the first thing to do is check each of the cuvettes to be used from the sample list, and to enter the desired wavelength range. If a number of trials are to be run (for repeatability) "Multiple Scans" should also be selected.

With everything ready, the Start Scan button initiates the scan. The user is first requested to select a location to save the data. For each trial, the data is saved in separate folders for each of the samples. There are three files: one with the cross-sections; one containing the previously measured emission and the concentration and resulting calibration constant; and one with the wavelength dependant I^2 raw data and the fit information. Additionally, the root trial folder will contain a file with all of the measured cross-sections, and another with the co-efficient of a log-log fit of the data used to measure the cross-section. It is important to note that the program eliminates points at the ends of the power range to achieve the best possible I^2 fit (this is to eliminate saturation if it occurs).

The next request is to load all of the sample emission files (hold control to select them). Then the software asks the user to input the location for each cuvette. Finally, the text file containing the concentration data needs to be loaded. If everything has gone smoothly the program will

now switch the laser to the starting wavelength and begin to poll data from the blank cuvette – the magic has begun! One should note that for each cuvette at each wavelength a preliminary measurement is taken to determine how bright the dye is. The intensity range is then modified so that the maximum counts will lie in the 200-400k range.

If at anytime the user wants to examine the data being collected, clicking the plot button next to the cuvette of interest in the sample list (Figure C.2) opens up a plot. Clicking the appropriate button displays the measured cross-sections so far, the emission wavelength, or the I^2 and (optionally) a rough fit of the data. A given trial may also be loaded at after it has been recorded. If multiple scans have been selected, the program will shut the laser off at the end of the last scan – but the PMT will still be on!